MODELING DISSOLUTION IN ALUMINUM ALLOYS

A Dissertation
Presented to
The Academic Faculty

by

Tracie Lee Durbin

In Partial Fulfillment
of the Requirements for the Degree
Doctor of Philosophy
in Mechanical Engineering

Georgia Institute of Technology

March 2005

MODELING DISSOLUTION IN ALUMINUM ALLOYS

Approved by:

Dr. Thomas Sanders, Jr.,Co-Chair
School of Material Science and Engineering
Georgia Institute of Technology

Dr. G. Paul Neitzel, Co-Chair
George W. Woodruff School of Mechanical Engineering
Georgia Institute of Technology

Dr. Hamid Garmestani
School of Material Science and Engineering
Georgia Institute of Technology

Dr. S. Mostafa Ghiaassiaan
George W. Woodruff School of Mechanical Engineering
Georgia Institute of Technology

Dr. Richard Neu
George W. Woodruff School of Mechanical Engineering
Georgia Institute of Technology

Date Approved: March 17, 2005

To my husband,

Samuel G. Durbin, II

my parents,

Ellen J. Zoeller

David W. Zoeller, 1946 - 2001

and my brothers.

Jeremiah D. Zoeller

Ian D. Zoeller, 1980 - 1995

Nicholas W. Zoeller

ACKNOWLEDGMENTS

First, I would like to thank my family for their love and support. My parents, David and Ellen, always encouraged me to pursue my dreams and expected great things for me. My brothers, Jeremiah, Ian, and Nicholas, have been a constant source of amusement throughout all these years of school. My husband Sam has provided me with a wealth of support and encouragement throughout our time in graduate school. We have been fortunate to take our classes and qualifiers together, and he has been my rock throughout this entire experience. I truly could not have made it through the ups and downs of graduate school without him.

I express my deep gratitude to my advisors, Dr. Thomas Sanders and Dr. Paul Neitzel, for their patience and guidance throughout my graduate school career. The discussions on everything from movies and politics to the Kirkendall effect with Dr. Sanders will be sorely missed. Great thanks go to my reading committee, Dr. Hamid Garmestani, Dr. Mostafa Ghiaasiaan, and Dr. Richard Neu. I would also like to thank my first advisor in graduate school, Dr. Damir Juric.

There are so many fellow students that have been of great help along the way. Dr. Seungwon Shin has proven to be an invaluable resource in regards to my numerical work, in addition to being a wonderful friend. Dr. Susan Stewart has been a true friend and a great study and workout partner (not to mention computer benefactor!).

Dr. Jaudelice Oliveira was the best roommate I ever had and I continue to value our relationship. Dr. Ben Church and Matt Trexler have been awesome over the past three years and I will miss both of them. My many officemates, extended group members, and fellow graduate students (whom I have not already mentioned) have brought interesting conversation and levity to my days: Maria-Isabel Carnasciali, Charles Dillinger, Richard Howe, Dr. Kevin Hurysz, Tim Koehler, Dr. Jason Nadler, Dr. Joerg Stromberger, Raymond Oh, Tammy McCoy, and Monique McIntosh.

Finally, I would like to acknowledge the funding for the National Sciences Physical Consortium Fellowship, generously given by the Engineering Sciences Center, 9100, at Sandia National Laboratories in Albuquerque, NM. The best thing to come out of my time at Sandia has been the strong relationships that I formed with Dominique Wilson, Richard Griffith, and Tom Voth. Dominique has been the big sister than I never had and I can never repay her for her generosity. Richard has been a constant source of enthusiasm and motivation in my life. Tom has been a great influence, throughout our relationship he has faced many challenges and overcome them with a will that is inspirational.

TABLE OF CONTENTS

LIST OF TABLES

LIST OF FIGURES

LIST OF SYMBOLS

A	Area
$\tilde{c}$	Transformed composition used for immersed-boudnary calculations
C	Composition
C_E	Eutectic composition
C_{max}	Maximum solid solubility composition
C_M	Matrix composition in binary alloy simulations
C_P	Precipitate composition in binary alloy simulations
C_S	Interface composition in binary alloy simulations
C_i	Composition of chemical element i
$C_{P,i}$	Precipitate composition of solutal element i
$C_{S,i}$	Interface composition of solutal element i
ds/dt	Interface velocity
D	Mass diffusivity
$\mathcal{D}$	Binary diffusivity coefficient
$\tilde{D}$	Transformed diffusivity field for front-tracking calculations
F_{ij}	Peskin function – representation of the Dirac delta function
G	Gradient of the indicator function
H	Heaviside function, also called the indicator function

J_x	Mass flux in the x–direction
J_y	Mass flux in the y-direction
$K(T)$	Solubility product for a multi-component alloy
K_0	Solubility product pre-exponential factor
K_{int}	Reaction rate at the moving interface
k_i	Front-tracking transformation ratio
L	Matrix boundary location in planar one-dimensional simulations
m_1, $m_{2,}$	Stoichiometric factors for precipitates.
m_3	
m_k	Interface mass source term.
n	Number of chemical species in an alloy
n	Normal to an interface point.
p	The smallest allowable distance between two interface points.
Q	Activation energy of formation
Q_i	Solutal source term for component i
r	Radial direction in cylindrical and spherical calculations
r_L	Outer matrix boundary location in cylindrical and spherical simulations
R	Universal gas constant
R	Interface vector in two-dimensional simulations
$s(t)$	Interface location at time t
s_0	Initial interfacial location, one-dimensional cylindrical and spherical calculations, radius of cylindrical precipitate in two-dimensional simulations
$\tilde{s}_i$	Transformed solute mass source term

s	Solute mass source term
T	Absolute temperature (Kelvin)
t	time (seconds)
Δt	Time step
$\mathbf{t}$	Tangent to an interface point.
v_x	x-component of interface velocity
v_y	y-component of interface velocity
x_0	Initial interface location, one-dimensional planar simulations
x_c	x-coordinate of center of precipitate in two-dimensional simulations
x_f	x-location of interface point
x_{ij}	Eulerian grid points.
x_L	x-coordinate, matrix boundary in two-dimensional simulations
x_p	Discrete interface points.
Δx	Spatial step in x-direction
$\mathbf{x_f}$	Interface position vector
y_c	y-coordinate of center of precipitate in two-dimensional simulations
y_f	y-location of interface point
y_L	y-coordinate, matrix boundary in two-dimensional simulations
Δy	Spatial step in y-direction

Greek Symbols

α	Represents the matrix phase in Chapter 4
β	Represents the precipitate phase in Chapter 4

δ	Dirac delta function
$\boldsymbol{\kappa}$	Curvature of an interface point.
η	Normal direction to the moving interface.
ρ_1, ρ_2	Density in phases 1 and 2

Subscripts

0	Initial values
1,2	Phase 1 and phase 2
α ,β	Phase α and phase β
f	Interface location
P	Precipitate phase
M	Matrix phase
S	Interface values

ABSTRACT

Aluminum and its alloys are used in many aspects of modern life, from soda cans and household foil to rigid containers, automotive and aircraft structures. Aluminum alloy systems are characterized by good workability that enables these alloys to be economically rolled, extruded, or forged into useful shapes. Mechanical properties such as strength are altered significantly with cold working, annealing, precipitation-hardening, and/or heat-treatments. Heat-treatable aluminum alloys contain one or more soluble constituents such as copper, lithium, magnesium, silicon and zinc that individually, or with other elements, can form phases that strengthen the alloy.

Microstructure development is highly dependent on all of the processing steps the alloy experiences. Ultimately, the macroscopic properties of the alloy depend strongly on the microstructure. Therefore, a quantitative understanding of the microstructural changes that occur during thermal and mechanical processing is fundamental to predicting alloy properties. In particular, the microstructure becomes more homogeneous and secondary phases are dissolved during thermal treatments. Robust physical models for the kinetics of particle dissolution are necessary to predict the most efficient thermal treatment.

A general dissolution model for multi-component alloys has been developed using the front-tracking method to study the dissolution of precipitates in an aluminum

alloy matrix. This technique is applicable to any alloy system, provided thermodynamic and diffusion data are available. Treatment of the precipitate interface is explored using two techniques: the immersed-boundary method and a new technique, termed here the "sharp-interface" method. The sharp-interface technique is based on a variation of the ghost fluid method and eliminates the need for corrective source terms in the characteristic equations. The immersed-boundary and sharp-interface techniques are compared to the exact solution of one-dimensional planar dissolution. The results show the sharp-interface front-tracking method more accurately matches the exact solution when compared with the immersed-boundary method. In addition, the sharp-interface method is shown to predict the dissolution behavior of precipitates in aluminum alloys when compared to published experimental results. The influence of inter-particle spacing is examined and shown to have a significant effect on dissolution kinetics. Finally, the impact of multiple particles of various sizes interacting in an aluminum matrix is investigated. It is shown that smaller particles dissolve faster, as expected, but influence the dissolution of larger particles through soft-impingement, even after the smaller particles have disappeared.

CHAPTER ONE

INTRODUCTION

Aluminum and its alloys are used in many aspects of modern life, from soda cans and household foil to the automobiles and aircraft in which wee travel. Aluminum alloys have numerous technical advantages that have made them one of the most useful alloy systems. Aluminum is a relatively light metal compared with metals such as iron, nickel, brass, and copper with a density of 2.7 g/cm^3. Although many aluminum alloys have typically low to intermediate strength, alloys containing precipitation-hardening elements such as copper (2XXX) or zinc and magnesium (7XXX) can have mechanical properties equivalent to some steels. The combination of high strength and low density make these alloys particularly attractive when structural weight is a critical property. In addition to high strength, aluminum alloys have a strong resistance to corrosion, which is a result of a tenacious oxide surface that forms quickly in air. This hard, microscopic oxide coating protects aluminum from many chemicals and weathering conditions. Aluminum and its alloys are also characterized by good workability that enables them to be economically rolled, extruded, or forged into useful shapes. Cold working, annealing, and in some alloys, precipitation-hardening and heat-treatments are used to control strength.

Aluminum alloys are separated into two major classes – cast and wrought. Cast-aluminum alloys are produced in hundreds of compositions by all commercial casting processes, including green-sand, dry-sand, composite-mold, plaster-mold, investment

casting, permanent-mold, counter-gravity tow-pressure casting, and pressure-die casting. Because cast alloys are poured into their final shape, they may be strengthened by heat-treatments but are not work-hardened. Wrought alloys differ from cast alloys in that they can be shaped by deformation. Aluminum alloys may be strengthened by thermal treatments (heat-treatable alloys) and by work-hardening (work-hardenable). Wrought-aluminum alloys are further separated into heat-treatable and non-heat-treatable. The 1XXX, 3XXX and 5XXX series alloys are non-heat-treatable, and thus are work-hardened by cold-working processes, usually by cold rolling. The 2XXX, 6XXX, and 7XXX series alloys are heat-treatable.

Heat-treatable aluminum alloys contain one or more soluble constituents such as copper, lithium, magnesium, silicon and zinc that individually, or with other elements, can form phases that strengthen the alloy. Also, aluminum alloys may contain impurities such as iron and silicon. Because of limited solubility, the morphology of phases formed by the combination of these impurities with major solute additions cannot be affected by heat treatment. In all aluminum alloys, the percentages of alloying elements and impurities must be controlled carefully. If they are not, properties such as strength, toughness, formability, and corrosion resistance, for example, may be affected adversely. However, while certain mechanical properties are improved, it may often be at the expense of other properties. For example, tensile and yield strengths can be increased, but this often results in lower elongation and fracture toughness. Thus, heat treatments are designed to optimize properties.

Heat-treating improves the strength of aluminum alloys through a process known as precipitation hardening. Precipitation hardening occurs during the heating and cooling

of an aluminum alloy in which precipitates are formed in the aluminum matrix. These second-phase particles affect dislocation motion which in turn affects strength. The composition of a particular alloy determines the heat treatment temperature. When an aluminum alloy is heated above the solvus temperature of the secondary phases in the matrix, the alloying elements dissolve into the aluminum matrix to form a solid solution. Following a quench (or rapid cooling), the alloying elements precipitate out of solution. This step, known as aging, occurs at room temperature (natural aging); however, an alloy can be artificially aged at an elevated temperature in order to increase the kinetics of the process.

Annealing in precipitation-hardening alloys is a process that imparts the most ductile condition. During annealing, the alloy is heated to above its solution temperature and then slowly cooled to room temperature. During the cooling processes, the alloying elements precipitate out of solution and form coarsely distributed phases, which are not effective barriers to slip. The result is a low-strength alloy.

Another method for increasing the strength of aluminum alloys is by work hardening. Work hardening increases the dislocation density and results in a higher strength alloy. Some examples of work hardening include forging, stamping and tube bending.

The important microstructural features, as far as toughness is concerned, are second phase particles and grain structure. The second-phase particles of concern are: (1) coarse, insoluble particles formed during casting, or coarse particles of normally soluble phases formed during casting or subsequent processing; (2) smaller intermediate particles formed during homogenization; and (3) aging precipitates. The as-cast microstructure is

highly segregated as a result of coring during solidification in which solutal element concentration and secondary phases are distributed unevenly throughout the microstructure.

The first step in alloy processing is, therefore, homogenization. This high temperature step is necessary to eliminate (or reduce) the coring by dissolving soluble phases and precipitating equilibrium phases. Although precipitate dissolution is not the only metallurgical process that is occurring during homogenization, it is often the most critical. The homogenization temperature can be determined from a thermodynamic analysis of the phases that are present. The homogenization time at a given temperature is dependent upon the types of precipitates present, their shape, size, distribution, and chemical composition. Subsequent processing steps for wrought alloys include: cold working, during which an alloy is simultaneously deformed and strengthened; hot working, during which an alloy is deformed at high temperatures without strengthening; and annealing, during which the effects of strengthening caused by cold working are modified. By controlling these processes, the material is processed into a usable shape while material properties are improved and controlled.

Microstructure development depends heavily on all of the processing steps the alloy experiences. Ultimately, the properties of the alloy depend strongly on the microstructure so it is particularly useful to gain a quantitative understanding of the microstructural changes that occur during thermal and mechanical processing. During thermal treatments, the microstructure becomes more homogeneous and secondary phases are dissolved. Hence, any modeling efforts directed towards understanding these

processes are important. Robust physical models for the kinetics of particle dissolution are necessary to predict accurately the most efficient thermal treatment.

In this thesis, particle dissolution in aluminum alloys is studied. To model the dissolution of second-phase particles in these alloy systems correctly, it is helpful to understand the microstructural changes that these alloys experience throughout their processing steps. The model that has been developed during this research is applicable for dissolution of particles in multi-component alloys in multi-dimensions. Because there is a dearth of information regarding dissolution of particles in higher-order alloys, the numerical simulations will be limited to binary (specifically Al-Cu and Al-Si) and ternary (Al-Mg-Si) systems.

1.1 Microstructure Formation

Ingot casting is a non-equilibrium phenomenon. Non-equilibrium effects during solidification fall into two categories: (1) coring of the solute across primary and secondary dendrite arms, and (2) precipitating a second phase by eutectic decomposition of the liquid solution resulting in the formation of large (> 0.3 μm) secondary intermetallics particles in the interdendritic channels whose size is controlled by solidification rate and alloy composition. Typically for commercial alloys these particles are approximately 2 to 50 μm in their longest dimension [1].

Both non-equilibrium effects contribute to the development of microstructure with further processing. The coring of the solute elements upon solidification establishes concentration gradients of each element within the microstructure. The presence of

coarse second phases within the cast microstructure precludes direct working of the ingot.

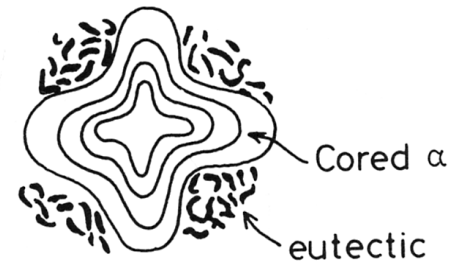

Figure 1.1 Cross section of a dendrite showing coring [2]

Coring occurs in all alloy systems that freeze over a range of temperatures. For example, in the case of a solidifying binary hypo-eutectic system, such as Al-Cu or Al-Si, dendritic cells form which have increasing amounts of solute from the cell center to its edges. Figure 1.1 depicts this phenomenon. The last liquid to solidify between the cells is a continuous, non-equilibrium eutectic phase. Since the continuous phase of any metal product controls the physical properties of the metal, and eutectic structures are typically brittle, the resulting cast structure is brittle and this impedes fabrication.

Many aluminum binary systems, such as Al-Cu and Al-Si, form eutectics. A basic eutectic phase diagram for hypothetical A and B is shown in Figure 1.2. The eutectic composition and the maximum solid solubility of B in A are indicated by C_E and C_{max} respectively. If the initial composition in a eutectic alloy is less than C_{max}, the precipitates that form will all be soluble. Conversely, if the initial composition is higher than C_{max}, both soluble and insoluble secondary phases will form. The focus of the current study will be soluble phases, therefore only "dilute" alloys will be considered.

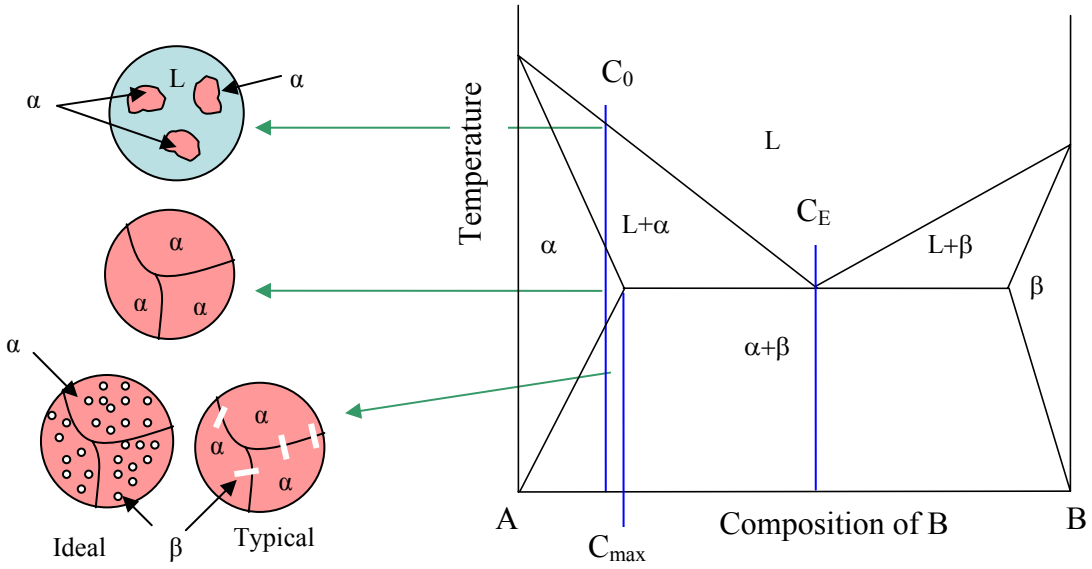

Figure 1.2 A sample binary eutectic phase diagram for hypothetical A and B. The first solid to form from a melt at initial composition, C_0 is the α-phase. The highest concentration of B in the α-phase will be C_{max}, the maximum solid solubility of B in A. The β-phase will form near the grain boundaries as the alloy cools to room temperature.

The thermal treatments that homogenize the structure prior to working smooth out the concentration gradients of the solutal elements and impurities. Additionally, the homogenization step will lead to dissolution of soluble second phases containing major solute elements and to precipitation of the dispersoid phases. The dispersoid-forming elements are retained in supersaturated solid solution after casting. The preheat temperature is above the solvus temperature for the coarse soluble phases but below the solvus temperature for the dispersoid phases.

After an alloy has been preheated, it may be plastically deformed by rolling, extrusion, drawing, and forging. A room temperature rolling is referred to as cold rolling and rolling at an elevated temperature is hot rolling. Rolling an ingot reduces the cross

sectional area, making it easier to fabricate into a final product. Insoluble constituent phases are broken up during rolling, reducing particle size and increasing particle number fraction. Deformation also serves to work harden via the introduction of dislocations into the microstructure to accommodate the strain involved with rolling. Hot rolling produces a more uniform dislocation distribution throughout the microstructure than cold rolling [3]. The microstructure attempts to attain equilibrium during and after deformation by two competing mechanisms: recovery and recrystallization. Recovery is the simultaneous creation and annihilation of dislocations, while recrystallization is the nucleation of new strain-free grains. The recrystallization behavior of an alloy must be limited because recrystallization can be detrimental to the strengthening characteristics of a worked alloy. Recrystallization can be affected by working conditions, second-phase particles, alloying elements and initial grain size [4]. These factors are affected by solidification rates and solute additions.

To summarize, an aluminum alloy will go through the following processing steps prior to industrial use: casting (or solidification), homogenization (or preheating), and rolling (in the case of work-hardenable alloys). An ideal microstructure would contain homogeneous concentrations of solutal elements and a uniform distribution of precipitates and dispersoid phases. Unfortunately, the final end product is typically non-ideal. A better understanding of the effects of solute gradients and secondary phase distributions will lead to producing a more ideal microstructure.

1.1.1 Aluminum – Copper System

Copper is the major solutal element in the 2000 series of wrought, heat-treatable aluminum alloys. These alloys are used for their strength in the aerospace and automobile industries. The aluminum-rich portion of the Al-Cu phase diagram is shown in Figure 1.3. Various temperature ranges for heat treatments are also shown on the phase diagram. After an Al-Cu alloy has been cast it will be solution heat treated just below the eutectic temperature. Depending on the product and stage in processing, the alloy may be annealed, with temperature ranges as shown in Figure 1.3.

As previously stated, the focus of this research is dilute alloys. Dilute alloys are those with an overall composition less than the maximum solid solubility. For example, consider an Al-Cu alloy containing 4.5 wt%Cu. At the solution heat treatment temperature, 540°C, all of the copper in the alloy is soluble in the alpha-matrix phase. A rapid quench to room temperature ensures that there is there is insufficient time at elevated temperatures to nucleate the second-phase; consequently the alpha solution is supersaturated. Furthermore, there is a supersaturation of vacancies. These excess vacancies arise because the quench maintains the vacancy concentration developed at 540°C. The vacancies accelerate precipitation to the extent that it occurs at temperatures at which it would ordinarily have low diffusion rates.

Diffusion in solid solutions is an important mechanism. An atom can move only if there is a vacant lattice site next to it. The diffusion mechanism involves an exchange between a vacancy and a diffusing atom. Precipitation at room temperature is too slow to be commercially acceptable, even with excess vacancies. While artificial aging reduces the time required for the phase transformation it also results in a decrease in the amount

of second-phase that can precipitate. Consequently, the selection of an appropriate aging temperature requires a balance between the time to age and the maximum achievable properties.

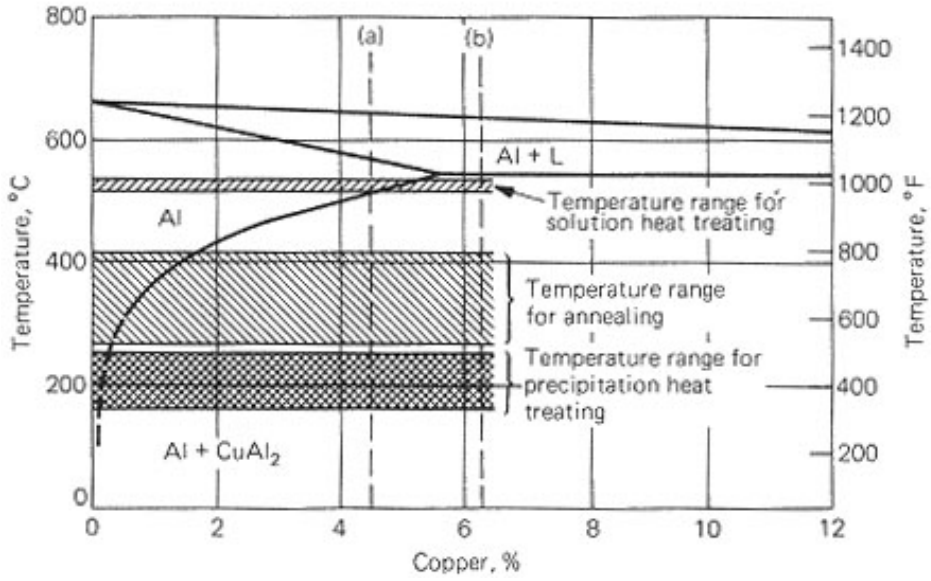

Figure 1.3 Aluminum-rich portion of the Al-Cu phase diagram with temperature ranges indicating heat treating operations [1].

Precipitation has been studied extensively in binary Al-Cu alloys. Guinier [5] and Preston[6] detected copper-rich zones in these alloys independently in 1938. These "GP zones" are typically formed as the first precipitate during low-temperature aging of aluminum alloys [7]. GP zones are believed to consist of copper and magnesium atoms collected on the $\{110\}_{Al}$ planes [7]. As has been stated previously, when supersaturated solid solutions decompose, one or more metastable phases may appear prior to or in addition to the equilibrium precipitate [8]. The formation of GP zones is often followed

by the precipitation of non-equilibrium phases in aluminum alloys. The precipitation sequence for the binary Al-Cu system is:

Supersaturated solid solution (SSS)→ GP zones→θ" →θ'→θ (Al_2Cu)

GP zones are copper-rich clusters about 8 nanometers in diameter and 0.3 to 0.6 nanometers thick. The GP zones have the same structure as the matrix, but have a much higher copper content. Because Cu atoms are smaller than Al atoms, strain fields around the precipitate are created. Upon heating, GP zones begin to dissolve, and a second precipitate, θ″, appears. The θ″ precipitate maintains a plate-like morphology about 30 nanometers in diameter and 2 nanometers thick and is coherent with the matrix. Upon further heating, θ'precipitates begin to form at the expense of the θ″. θ′ precipitates are on the order of 100 nanometers in diameter and semi-coherent with the matrix. Finally, the precursor phases disappear and θ precipitates form. θ is the equilibrium phase and is incoherent with the matrix.

GP zones are more like the matrix than any of the other phases, including the equilibrium theta phase. The magnitude of the precipitate-matrix interfacial energy increases from GP zones to θ″ to θ′ to θ. Third, the stability of the phases increases likewise so regardless of which phase forms first, eventually the equilibrium θ phase will be present [9].

1.1.2 Aluminum-Magnesium-Silicon System

The aluminum-magnesium-silicon system is the basis for a major class of heat-treatable alloys used for both wrought and cast products. Because 6XXX alloys are easy

to fabricate and have high tensile strength after heat-treating, ranging from 90 MPa (13 ksi) to 400 MPa (58 ksi) [10], Al-Mg-Si alloys are used in automobiles and in architectural products. The Al-Mg-Si system of wrought alloys undergoes similar processing to the Al-Cu alloys, and the microstructure development is analogous to that described above. Most commercial compositions in the Al-Mg-Si alloys, at normal aging temperatures, occur in a ternary phase field consisting of the equilibrium phases: primary aluminum; the β-phase (Mg_2Si); and silicon.

The precipitation reactions in this alloy system have been studied and the following sequence has been noted [1]:

Supersaturated solid solution→ semi-incoherent β″ rods→ semi-coherent β′ needles→ semi-coherent β plates → non-coherent β (Mg_2Si).

Several ternary phase diagrams are given for the Al-Mg-Si system below. Figure 1.4 shows the liquidus projection. Figures 1.5 and 1.6 show the solidus and solvus projections, respectively. An isothermal slice is taken across the ternary phase diagram at 340°C and shown in Figure 1.7. It is obvious that the ternary phase diagrams are much more complicated than binary phase diagrams.

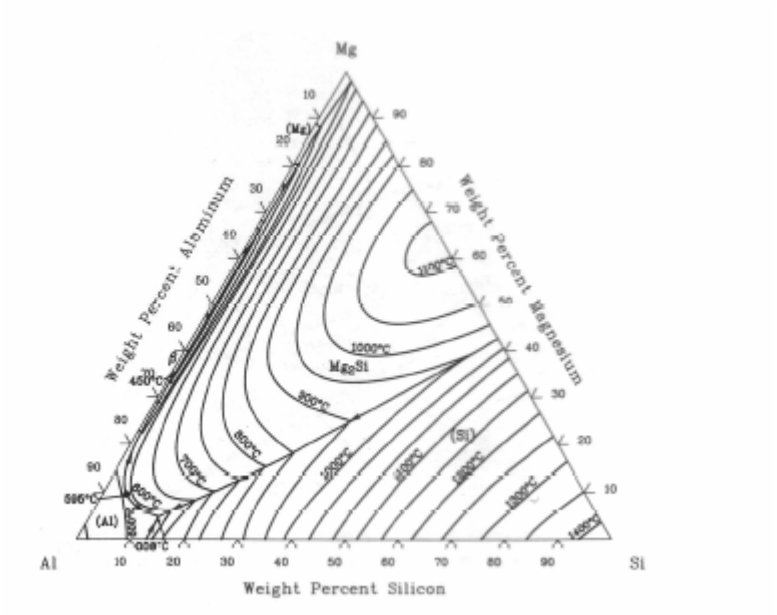

Figure 1.4 The liquidus portion of the Al-Mg-Si ternary phase diagram[11].

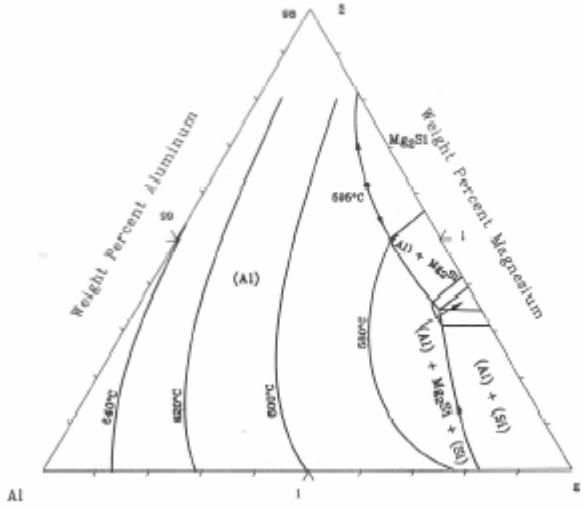

Figure 1.5 The solidus projection of the Al-Mg-Si phase diagram[11].

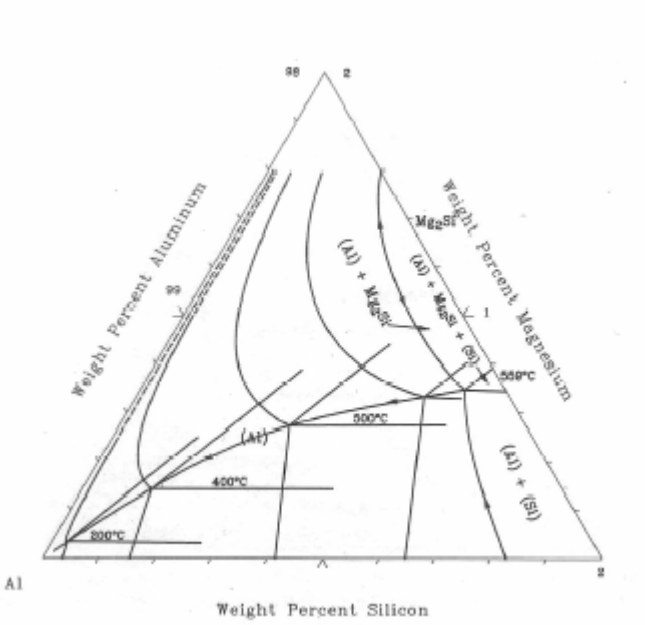

Figure 1.6 Solvus projection of the Al-Mg-Si phase diagram[11].

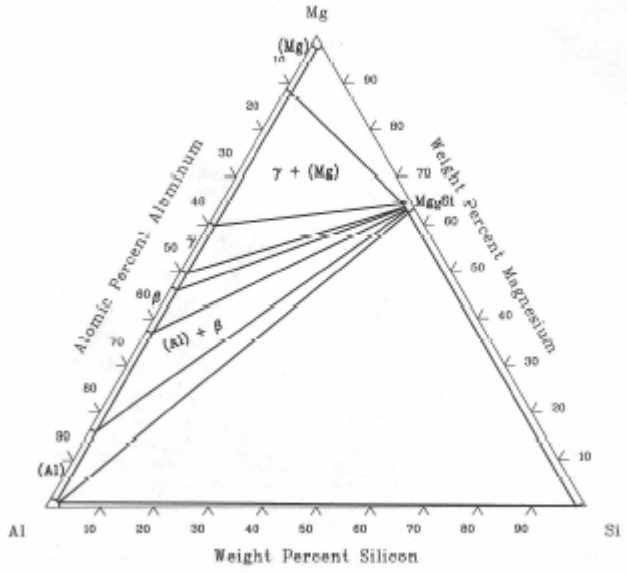

Figure 1.7 Al-Mg-Si phase diagram at 340°C[11].

An interesting feature of the Al-Mg-Si system is that it is a pseudo-binary Al-Mg_2Si at magnesium to silicon ratios of 1.73-to-1 (wt%). Figure 1.7 shows the Al-Mg_2Si pseudo-binary phase diagram.

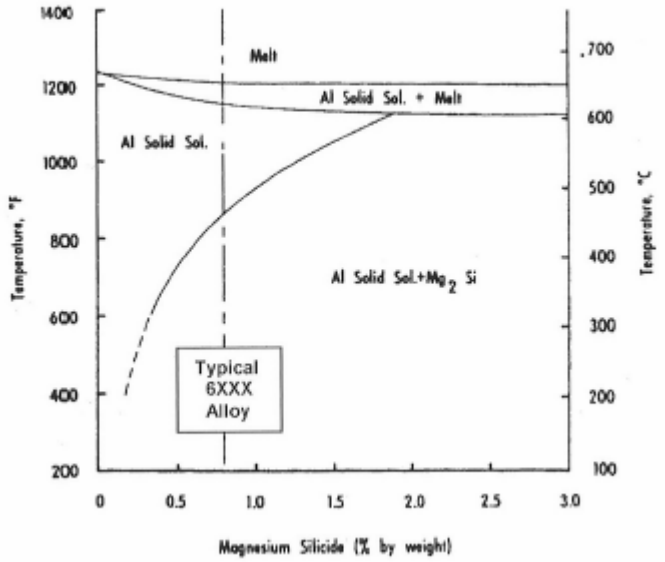

Figure 1.8 Al-Mg_2Si pseudo-binary phase diagram [11].

1.1.3 Aluminum-Silicon System

Another important set of aluminum alloys is the aluminum-silicon system, which are commercially viable due to their high fluidity and low shrinkage in casting, brazing and welding applications [1]. Binary aluminum-silicon alloys are characterized by high corrosion resistance, good weldability, and low specific gravity. The Al-Si system is a simple eutectic system, however Al-Si alloys differ from "standard" eutectics. In the aluminum-silicon system, solid solubility of aluminum in solid silicon at any temperature

is nil, see the phase diagram in Figure 1.9. The enlarged aluminum-rich portion of Figure 1.9 is shown in Figure 1.10. This means that there is no β phase and so when considering dissolution, this secondary phase is pure silicon. So, for Al-Si alloys, the eutectic composition is a structure of α+Si rather than α+β. The primary Si has a cuboidal form. The eutectic is non-lamellar in form and appears to consist of separate flakes [12]. These coarse flakes of Si in the eutectic promote brittleness within these alloys. Most Al-Si alloys used have a near-eutectic composition since this gives a lower melting point and makes them cheaper to cast [3].

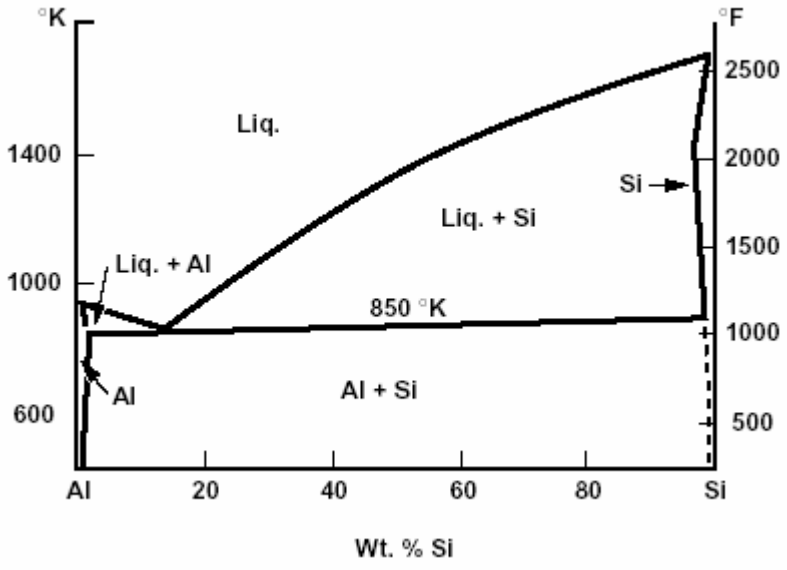

Figure 1.9 Aluminum-Silicon Phase Diagram from Mondolfo[12].

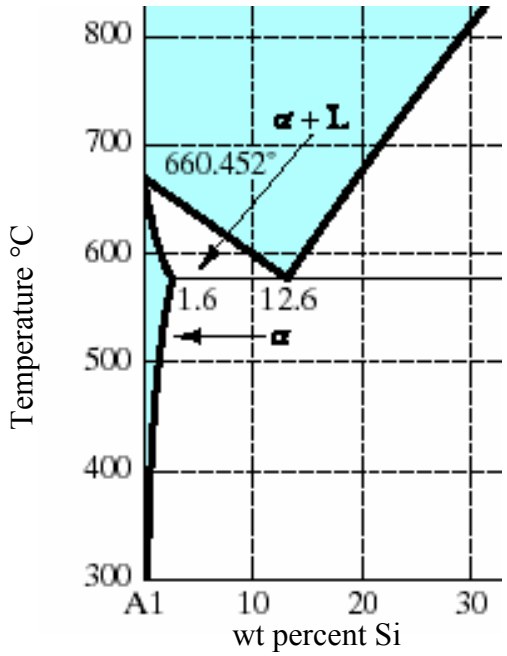

Figure 1.10 Aluminum-rich portion of the Aluminum-Silicon phase diagram.

Most commercial aluminum-silicon alloys are at the eutectic composition, or higher. These cast alloys are used for their resistance to wear. When the composition of silicon in the alloy exceeds the eutectic composition, the microstructure is characterized by an aluminum matrix with insoluble silicon particles. Due to coarsening, these particles become spherical in shape, however this phenomenon is not addressed in the current study. However, because of the simplicity of the system, there have been numerous investigations on the precipitation and dissolution of silicon in Al-Si alloys containing silicon less than the solid solubility[13].

1.2 Overview of Previous Modeling Efforts

As described above, alloys are heat treated to smooth out inhomogeneities and to optimize their mechanical properties. During heat treatment the types of phases that are present, and the morphology of these phases, can change. Throughout processing, beginning with the solidification step and ending with the final solution heat treatment step, there are a variety of particles that form. The formation of secondary phases in aluminum alloys is very important to the final macroscopic properties of the alloy. Precipitate precursor phases form during casting and provide the necessary conditions for precipitates to form through subsequent material processing. The precursor phases dissolve at the expense of the desired precipitates. Thus the dissolution and precipitation of the different phases along the processing route are essential to the development of an optimum microstructure. The ability to predict the dissolution process of secondary phases is an important step toward developing a quantitative model to simulate microstructural development.

Particle dissolution has been modeled by numerous researchers using a variety of analytical and numerical techniques [13-39]. Over a period of many years, several analytical models have been developed [36-38] which describe the kinetics of particle dissolution in metals and alloys under elevated temperatures. These solutions all represent approximations of the diffusion field around the dissolving precipitate and are all for infinite domains. Numerical studies [13-36, 39] have attempted to describe the dissolution kinetics in a precise manner; however these models deal primarily with binary alloys and isothermal annealing. In more recent studies, dissolution models were

extended to multi-component systems in one-dimension[29-34] and to binary systems in two-dimensions[24, 39].

There are two modes that control the rate limiting step for particle dissolution, diffusion away from the interface, interface reactions, or a mixture of both. In the case of diffusion control, any interface reactions that are necessary for the precipitate to dissolve occur much faster than the diffusion of solute into the matrix. Alternatively, if an interface reaction (such as a phase change) is required before the solute can diffuse into the matrix, the dissolution process is considered to be interface controlled. Figure 1.11 shows the corresponding solute gradients in the matrix for both diffusion controlled and interface controlled dissolution. Under diffusion control, the interface boundary condition remains constant, and is determined by the maximum solid solubility of the phase diagram, as shown in Figure 1.11. Furthermore, as time progresses under interface control and the particle dissolves, the composition ahead of the precipitate decreases to the average composition over the entire domain, given by C_0. Diffusion control and interface control are the two extreme cases of particle dissolution. If the dissolution is mixed-mode controlled, the concentration profiles will be similar to those found under diffusion-control conditions. The interface composition will vary from the equilibrium value, however, and during the process when the interface reaction is the rate-limiting step, the concentration gradients will have time to smooth out in the matrix.

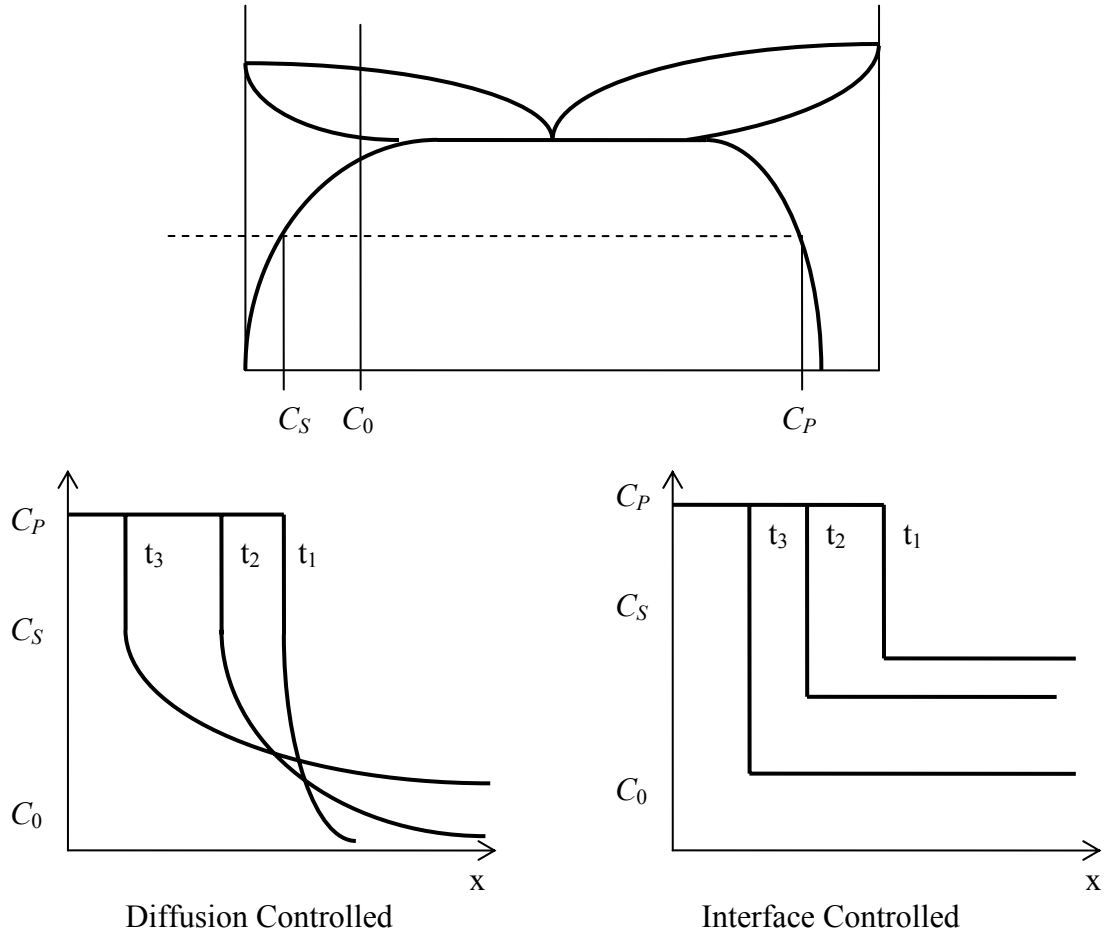

Figure 1.11 Schematic of a binary phase diagram and concentration profiles at the precipitate/matrix interface at times t_1, t_2, and t_3, showing the difference between dissolution that is interface controlled and diffusion controlled ($t_1<t_2<t_3$).

For the most part, second-phase particles dissolving in a metal matrix may be considered to be diffusion controlled. A chemical reaction at the interface would be necessary to provide the conditions for interface controlled dissolution. Most researchers have focused on diffusion-limited dissolution while a handful [35, 37, 38] developed methods in which mixed-mode control could be incorporated.

The early models of particle dissolution were based on analytical solutions in an unbounded medium under the assumption of local equilibrium at the moving interface[36, 37]. Aaron and Kotler [37], for example, investigated second-phase dissolution of precipitates, including effects of diffusion, interface reaction and curvature in their model. They noted that, for spherical precipitates dissolving in an infinite matrix, as time increases, the volume for mass transfer increases, thereby speeding up the dissolution process. This is different from the planar case because the volume for mass transfer ahead of the moving interface is always constant. As the solute from a spherical particle diffuses into the matrix, more and more surface area is available for mass transfer. The authors also observed that for dilute alloys the curvature effects were negligible. Interface reactions were also included in Aaron and Kotler's analysis. They developed an expression to determine the deviation of the interface concentration from the equilibrium (or diffusion-limited) value for various interface-reaction mechanisms, including uniform atomic detachment, screw-dislocation, and ledge mechanisms. Whelan [36] performed a similar analysis for purely spherical precipitates. Both Aaron and Kotler [37] and Whelan[36] developed analytical expressions for the radius of a spherical dissolving precipitate in a binary alloy in an unbounded domain.

Nolfi *et al*. [38] used separation of variables to solve for the kinetics of dissolution and growth of a spheroidized, solute-rich stoichiometric precipitate in the surrounding matrix. In this study, the interfacial reaction between the particle and its surrounding phase were included. Two limiting cases were examined: (1) long-range solute diffusion through the matrix with interfacial equilibrium (diffusion control) and (2) the transfer of atoms across the matrix-precipitate interface with the rate of dissolution or

growth being controlled by an interfacial reaction. Mixed-mode control was also considered. Nolfi *et al*. [38] were the first to introduce a quantitative estimate of the mixed-mode character for the dissolution of spherical precipitates. A major limitation in this analysis was the assumption of constant precipitate size.

Tanzilli and Heckel [26] solved the diffusion equation numerically using a finite-difference technique. They combined a Crank-Nicolson discretization of the diffusion equation with a Murray and Landis [40] grid transformation to account for the moving boundary in binary systems. Their model, in principle, can be used to describe the dissolution kinetics in materials with a given volume fraction of precipitates of different shapes. However their model has some major limitations. The main assumption in the model is that all precipitates are of equal size and that they are divided into identical, spherical cells having the particle at their center. A consequence of this geometry is that all of the precipitates dissolve completely at the same annealing time. Tundal and Ryum [41] have extended this analysis to include a distribution of particle sizes. They showed that the macroscopic dissolution rates depend strongly on the particle size and possible interactions between subsequent particles. Again, spherical particles that are at the center of their respective spherical volumes are considered. This assumption was justified by the conclusion that if dissolution is controlled by volume diffusion, the precipitates will become spherical as they shrink. Tundal and Ryum [13] compared their model to experiments of Si-atoms in an Al-Si alloy. At high temperatures (and therefore high diffusivity of Si in Al) the numerical results compared well with experiments.

Vermolen and co-workers [16, 17, 27-32, 34, 35, 39] have done considerable work in dissolution modeling. A semi-analytical model was derived for the dissolution

of spherical particles in finite media assuming that long-distance diffusion is the only rate-limiting step [28]. The model allowed the prediction of the dissolution kinetics as a function of the initial concentration differences between particle and matrix and the interface concentration during dissolution. Several assumptions were made to formulate the solution including that the alloy is dilute and the solutal element has limited solubility in the matrix phase. Vermolen [35] then extended this 1-D model to incorporate any combination of first order reactions at the particle-matrix interface and long-distance diffusion in the matrix. The dissolution could be diffusion-controlled, interface-reaction-controlled, or a mixture of the two.

Segal *et al*. [24] extended Vermolen's one-dimensional binary analysis to two dimensions. A finite-element method was used with a moving mesh. Some instabilities in the precipitate interface were observed for sharp edges and the authors outlined a new method for calculating the interface motion based on mesh regeneration at each time step. The precipitate phase was not included in the calculations. Two-dimensional concentration fields were shown, and soft-impingement of differing size particles was observed.

Multi-component systems dissolution was also investigated for iron alloys by Vitek [42] and in an Al-Mg-Si alloy by Reiso *et al*. in [43]. More recently, Vermolen and colleagues [29-32] have extended their one-dimensional spherical model to include multi-component alloys. In general, they have used a finite-volume model for a one-dimensional spherical geometry, assuming that all particles in the alloy are the same size and equidistant from each other. The dissolution rate was correlated to heat flow in Langkruis [21] to compare the results of the model with differential scanning

calorimetry (DSC) measurements. The model was then used to predict peak hardness for a standard artificial heat treatment as a function of initial structure and heating schedule. The model compared reasonably well with the experiments; however it could be improved by using a more realistic geometry and distribution of particles.

For the most part when considering dissolution of particles in a multi-component system, cross-diffusional terms in the diffusivity matrix are neglected. The cross-diffusional terms in the diffusivity matrix are the off-axis entries that are a measure for the interaction of diffusion in the matrix between consecutive alloying elements. When an alloying element dissolves in the matrix it may facilitate or hinder diffusion of the other elements. Vermolen *et al*. [30] [31] considered the case when these cross-diffusional terms could not be neglected. They used front-tracking with a moving grid. The interface point always coincides with a grid node using this scheme. An implicit finite-difference method was used to solve the diffusion in the matrix while the convective term due to grid movement was treated explicitly. A geometrically distributed grid was used such that the discretization was fine near the moving interface and coarser farther away. In [34], Vermolen *et al*. developed analytical approximations for an unbounded domain and compared it with their numerical solution. As expected, at earlier times the two models showed good agreement but diverged at later times when soft-impingement started occurring. Using the analytical approximation as a basis, cross-diffusion was shown to have a large impact on the dissolution of the particle when the off-diagonal terms in the diffusivity matrix were on the same order as the diagonal terms.

Thus, there are some limitations that must be recognized when considering previous modeling of particle dissolution. First, most particles are not ideally shaped;

therefore a two or three dimensional model is necessary to compute the dissolution of non-ideal particles. Furthermore, the case where more than one particle is dissolving in a two-dimensional cell needs to be examined. Additionally, there have been no previous two-dimensional multi-component simulations. These specific issues will be addressed in this thesis.

1.3 Research Objectives

The aim of this thesis is to model the dissolution of secondary phases in aluminum alloys. To this end, a general multi-component dissolution model based on the front-tracking method of Shin[44] and Juric [45] was developed. Because much of the literature covers binary and ternary alloys specifically, these types of alloys were focused on in the current study. Therefore, the two-dimensional model was applied to binary alloys, as well as ternary alloys. Additionally, one-dimensional, mass-conserving dissolution models for planar, cylindrical, and spherical precipitates were developed and applied to binary and ternary systems.

Using these models, the impact of initial conditions on the dissolution of precipitates in aluminum alloys will be studied. Particle size, shape, and distribution are important to the overall homogenization of the alloy, and thus are important to the current work. The interactions of more than one particle dissolving in the same matrix cell will be considered.

The remainder of this dissertation is organized as follows: In Chapter 2 the theory behind the development of the governing equations will be described, as well as

the numerical techniques utilized in this investigation. The model is validated in Chapter 3 for binary alloys based on comparisons with exact solutions and experimental data. In Chapter Four the model is applied to ternary alloys. The main conclusions of the dissertation are summarized in Chapter 5, along with recommendations for future modeling efforts. Finally, the finite-difference equations for the two-dimensional simulations are given in Appendix A

CHAPTER TWO

DISSOLUTION MODEL

2.1 Introduction

The mathematical theory and the numerical method for the dissolution problem will be developed in this chapter. First, the general case of multi-component dissolution in two-dimensions will be described and the governing equations will be formulated in section 3.2. Then the numerical method will be described in section 3.3. Finally, the solution procedure will be discussed in section 3.4.

2.2 Governing Equations

In a multi-component alloy, precipitates containing *n* different chemical elements, which are different from the bulk-alloy-matrix phase, may form. In this case, *n* diffusion equations must be solved, which are coupled through conditions on the moving boundaries. As the precipitate dissolves, the radius shrinks and the interface moves. Solute is rejected into the bulk phase and diffuses outwards into the matrix according to the material properties of the alloying element being considered.

Consider an arbitrary matrix with two phases, where phase 1 is the majority phase, and phase 2 is the minority phase, referred to as the dissolving phase, separated by a moving interface, denoted by $s(t)$, shown in Figure 2.1. The velocity of the moving interface, which is found by solving an interfacial flux balance, is the same for each element in a given phase. Additionally, the interfacial concentrations of all of the chemical elements in a particle are hyperbolically related to each other[2, 32]. For chemical elements $C_i, i \in \{1,...,n+1\}$, with stoichiometry $(C_1)_{m1}(C_2)_{m2}(C_3)_{m3}(...)(C_n)_{m4}$, the solubility product, $K(T)$, is given by:

$$(C_{1,S})^{m1}(C_{2,S})^{m2}(C_{3,S})^{m3}(...)(C_{n,S})^{mn} = K(T) \tag{2.1}$$

where the subscript S refers to the interface composition.

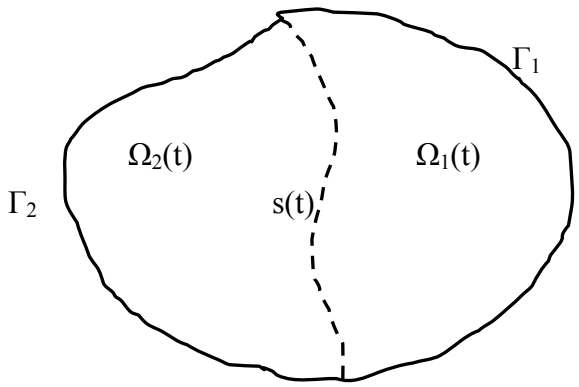

Figure 2.1 Arbitrary solution domain in two dimensions. The areas of the two separate phases, phase 1 and 2 are given by $\Omega_1(t)$ and $\Omega_2(t)$, fixed outer boundaries Γ_1 and Γ_2, and moving boundary s(t).

The solubility product follows an Arrhenius relationship with temperature[2],

$$K(T) = K_0 \exp\left(-\frac{Q}{RT}\right) \tag{2.2}$$

where K_0 is the pre-exponential factor, Q is the activation energy of formation, R is the gas constant, and T is the absolute temperature.

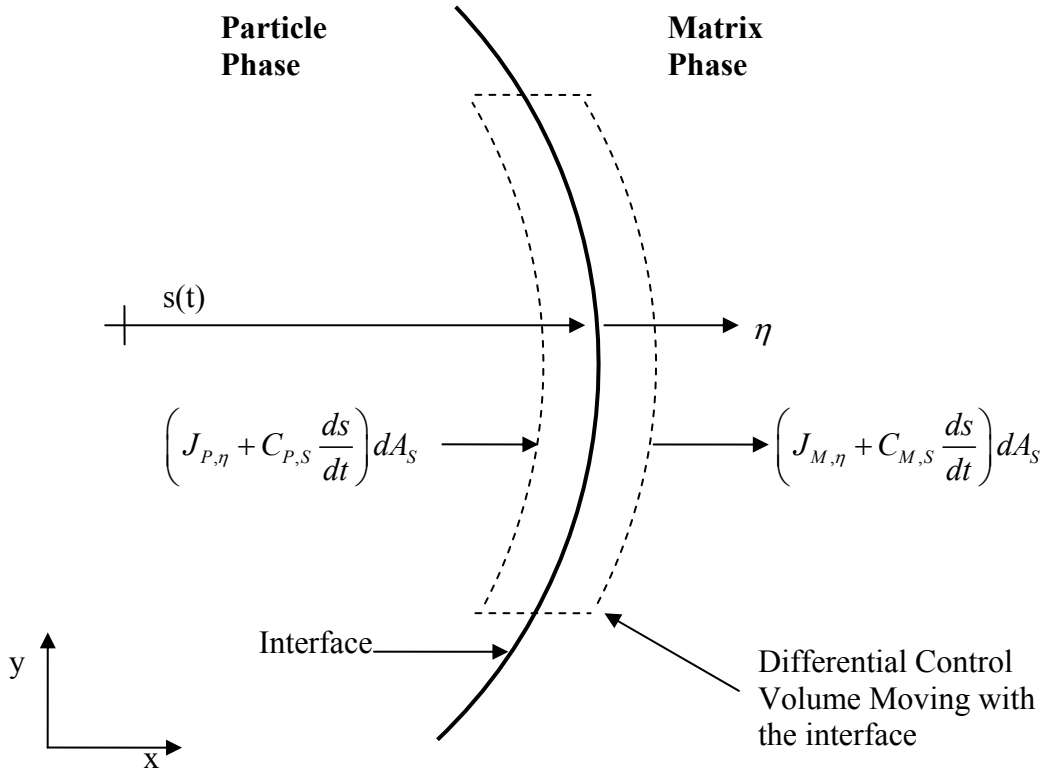

Figure 2.2 Mass transport across a phase boundary. $J_{P,\eta}$ and $J_{M,\eta}$ are the mass fluxes normal to the interface in the particle and matrix phases, $C_{P,S}$ and $C_{M,S}$ are the interface compositions in the particle and matrix phases, and dA_S is the differential surface area of the interface in the control volume.

The system must satisfy the principles of conservation of mass at the interface. The transport of mass across the interface is schematically indicated in Figure 2.2. In Figure 2.2, subscript *P* refers to the particle phase, subscript *M* refers to the matrix phase, and subscript *S* refers to values on the interface in each phase. An arbitrary solutal element is being considered, so the subscript *i* has been dropped. Mass must obviously be conserved for all components in the system. Mass is transported to and from the interface, with differential surface area dA_S, by Fickian diffusion (indicated by mass fluxes $J_{P,\eta}$ and $J_{M,\eta}$). Note that the mass flux is in the direction normal to the interface, η. The interface is moving with a velocity of ds/dt, so the rate of particle mass flow moving towards the control volume moving with the interface is $\left(J_{P,\eta} + C_{P,S}\frac{ds}{dt}\right)dA_S$. In a similar manner, it can be argued that the rate of matrix mass flow moving out of the control volume is $\left(J_{M,\eta} + C_{M,S}\frac{ds}{dt}\right)dA_S$.

The control volume in Figure 2.2 is assumed to be so thin that there is negligible accumulation of mass within it. Conservation of mass for a this control volume requires that

$$J_{P,\eta} + C_{P,S}\frac{ds}{dt} = J_{M,\eta} + C_{M,S}\frac{ds}{dt}, \tag{2.3}$$

which can be rearranged to obtain

$$J_{M,\eta} - J_{P,\eta} = \left(C_{P,\eta} - C_{S,\eta}\right)\frac{ds}{dt}. \tag{2.4}$$

The mass fluxes in the direction normal to the interface are given by

$$J_{M,\eta} = -D_M \frac{\partial C}{\partial \eta} \text{ and } J_{P,\eta} = -D_P \frac{\partial C}{\partial \eta} \tag{2.5}$$

where D_M and D_P are the diffusivities of the arbitrary solutal element in the matrix and particle phases, respectively. There is no subscript on composition, C, here because we are only considering one element. The analysis is valid for all solutal components in the system. Combining Equations (2.4) and (2.5) yields the following relationship for mass conservation at the interface:

$$D_P \frac{\partial C}{\partial \eta} - D_M \frac{\partial C}{\partial \eta} = (C_{P,S} - C_{M,S}) \frac{ds}{dt}. \tag{2.6}$$

A schematic of the composition profile across the interface for component i is shown below in Figure 2.3.

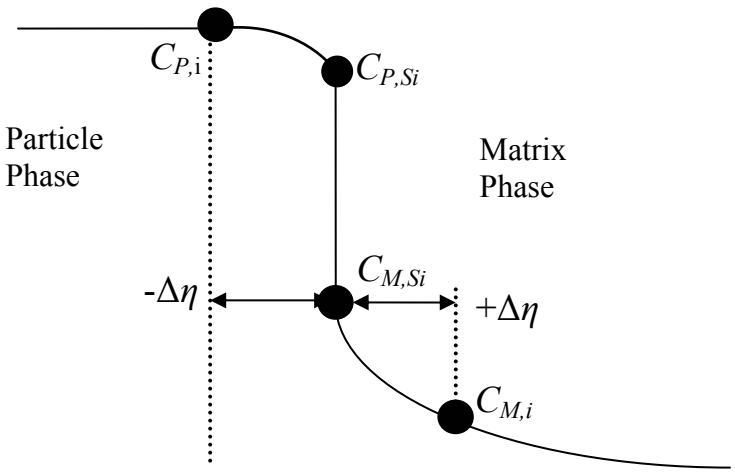

Figure 2.3. Schematic of particle/matrix interface composition profile during dissolution for component *i*. $C_{P,i}$ is the composition one node inside the particle (- $\Delta\eta$), $C_{P,iS}$ is the interface composition of the particle, $C_{M,iS}$ is the interface composition in the matrix, $C_{M,i}$ is the composition one node outside of the particle (+$\Delta\eta$) and $C_{M,iS}$ is the far field composition of the matrix.

The preceding derivation has assumed that all of the solutal elements are diffusing independently of each other. However, this may not be a valid assumption for some systems. When the solutal elements are affecting the diffusion of element i, a species-dependent diffusivities (D_{ij}) must be used. For example, consider chemical element 1. $D_{P,1n}$ accounts for the effect of element-*n* on the diffusion of element-1 in the particle phase. Therefore, the interfacial mass conservation for chemical element 1 becomes:

$$\sum_{j=1}^{n}\left(D_{P,1j}\frac{\partial C_1}{\partial \eta} - D_{M,1j}\frac{\partial C_1}{\partial \eta}\right) = (C_{P,1S} - C_{M,1S})\frac{ds}{dt}. \qquad (2.7)$$

Equation (2.7) is valid for every single chemical element in the system. The velocity of the moving interface, *ds*/*dt*, is identical for all elements in the system. Consider a three-component alloy where *n*=3. Solving for the interface velocity and rearranging,

$$\frac{\sum_{j=1}^{3}\left(D_{P,1j}\frac{\partial C_1}{\partial \eta}-D_{M,1j}\frac{\partial C_1}{\partial \eta}\right)}{(C_{P,1S}-C_{M,1S})}=\frac{\sum_{j=1}^{3}\left(D_{P,2j}\frac{\partial C_2}{\partial \eta}-D_{M,1j}\frac{\partial C_2}{\partial \eta}\right)}{(C_{P,2S}-C_{M,2S})}=\frac{\sum_{j=1}^{3}\left(D_{P,3j}\frac{\partial C_3}{\partial \eta}-D_{M,3j}\frac{\partial C_3}{\partial \eta}\right)}{(C_{P,3S}-C_{M,3S})}.$$

This gives the second relationship necessary for determining the position of the moving interface at any given time. The first condition is given by the stoichiometry of the particle, shown in Equation (2.1). The unknowns in above set of equations are the compositions of the chemical species, C_i, the interface compositions at each time step, $C_{S,i}$, and the interface velocity, *ds*/*dt*.

The above interfacial-flux equation does not take into account any interface reactions that may be occurring. If there are interface reactions occurring, a third interface condition is needed. Supposing a first-order reaction is occurring at the interface,

$$K_{\text{int}}(C_{sol,i}-C_{M,Si})=\sum_{j=1}^{n}\left(D_{P,1j}\frac{\partial C_1}{\partial \eta}-D_{M,1j}\frac{\partial C_1}{\partial \eta}\right)-(C_{P,1S}-C_{M,1S})\frac{ds}{dt},\ \text{for}\ i\in\{1,...,n\} \quad (2.8)$$

where K_{int} is a measure of the rate of the interface reaction, $C_{sol,i}$ is the equilibrium solid solubility of component *i* and $C_{S,i}$ is the actual interface composition of component *i*. As

K_{int} becomes large, the dissolution becomes diffusion-controlled and as K_{int} becomes small, the dissolution is interface-reaction-controlled.

In addition to conserving mass at the interface, each alloying element must also conserve mass globally over the entire domain. In the case of a multi-component alloy, each individual diffusion equation may have terms associated with the other alloying elements. Consider the control volume shown in Figure 2.4.

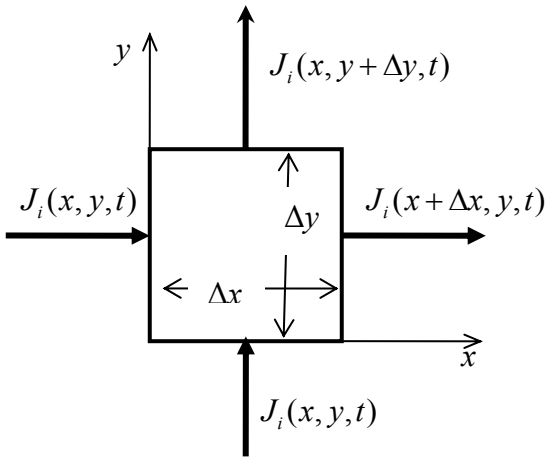

Figure 2.4 Control volume over which mass flux of each component is calculated.

In each phase, the mass fluxes across the control volume in the x and y directions are given by

$$J_i(x,y,t) = -\sum_{j=1}^{n} D_{ij} \frac{\partial C_j(x,y,t)}{\partial x}, \quad J_i(x+\Delta x,y,t) = -\sum_{j=1}^{n} D_{ij} \frac{\partial C_j(x+dx,y,t)}{\partial x} \tag{2.9}$$

and

$$J_i(x,y,t) = -\sum_{j=1}^{n} D_{ij} \frac{\partial C_j(x,y,t)}{\partial y}, \quad J_i(x,y+\Delta y,t) = -\sum_{j=1}^{n} D_{ij} \frac{\partial C_j(x,y+dy,t)}{\partial y}. \tag{2.10}$$

where the diffusivities, D_{ij}, are the multi-component diffusion coefficients of the chemical species in the system. D_{ij}, in general, are different from binary mass diffusivities, $\mathcal{D}_{ij}$, and, unlike $\mathcal{D}_{ij}$, are strongly concentration dependent. Summing these fluxes over a differential control volume and taking the derivative with respect to time yields Fick's second law in two-dimensions:

$$\frac{\partial C_i}{\partial t} = \sum_{j=1}^{n} \left\{ \frac{\partial}{\partial x}\left(D_{ij} \frac{\partial C_j}{\partial x} \right) + \frac{\partial}{\partial y}\left(D_{ij} \frac{\partial C_j}{\partial y} \right) \right\}, \text{ for } i \in (1,...,n) \tag{2.11}$$

The set of governing equations that must be solved to find the dissolution of a second-phase particle in a matrix are given above. This set of equations is part of a general class of problems, commonly known as Stefan problems. The interface condition given in Equation (2.7) is known as the Stefan condition. If interface reactions are important, Equation (2.8) must also be applied.

Front-tracking was used primarily in this work and the numerical technique will be described here for a general multi-component alloy in two-dimensional Cartesian coordinates. First, however, it is useful to consider how the interface compositions at the particle/matrix interface are determined.

The composition in the particle and the matrix and the interfacial boundary can be found in a number of ways. If the phase diagram information is available, it may be used to determine the equilibrium concentrations for the alloy system being studied. Phase-diagram-calculation software, such as Pandat and Thermocalc, can be used to find the concentrations for many alloys. For multi-component alloys, if the solubility product constants are known for various precipitates, they can be used to find the interface compositions. Alternatively, free-energy functions may be used to determine the equilibrium boundary conditions. In this research, systems in which the phase diagram information is available have primarily been used.

2.3 Numerical Method

Particle dissolution is often considered to be a Stefan problem – essentially diffusion with a moving interface. In addition to particle dissolution, melting, solidification, and other phase-change phenomena may be described as Stefan problems. Many approaches have been taken to solve these types of problems such as front-fixing, implicit methods such as level-set and phase-field methods, as well as various front-tracking approaches.

In front-fixing methods, the position of the interface is fixed by a suitable choice of new space variables. In this type of method, the interface position is always at a grid node. The transformed differential equations may be more complicated than the original set of equations and it is difficult to apply in two and three dimensions [19, 46].

The level-set method uses an implicit representation for the interface, captured as the zero level set of a continuous function. The advantage is that topological changes of the interface are handled in a simple manner, however mass loss has been observed using this method [19, 47, 48].

The phase-field method is an implicit method that uses a phase-field function parameter to characterize the domain. The main idea is to couple the governing equation of the physical problem with an equation derived from a Helmholtz free-energy functional of the phase-field function[49, 50]. The interface is represented by a smoothed transition region, and so it may be difficult to resolve fine details. One of the drawbacks of the phase-field model is the appearance of new parameters which are difficult to control and depend on the free-energy functional chosen[50].

Front-tracking methods follow the interface in time. The moving grid method is one of these, in which the grid is adjusted at each time step to keep the same number of nodes in each phase. Vermolen and co-workers [24, 27-35] used this method for the particle-dissolution problem. In two and three dimensions it is necessary to regenerate the mesh at every time step, which can become time consuming[19]. The front-tracking method developed by Juric and Trygvasson [51] for solidification utilized two grids: a stationary grid combined with a moving interface grid. This approach allows the moving

front to be followed accurately without the time consuming effort needed for mesh regeneration. Shin [44] improved on this method for modeling boiling phenomena.

The front-tracking method developed by Juric [45, 51] and Shin [44, 52, 53] will be utilized in this work. Again, the interface is tracked explicitly, and, in two-dimensional solutions, the Lagrangian (moving) surface gives the interface location. The material properties and the concentration field are specified at stationary, or Eulerian, grid points. Two different methods for determining the interface velocity and concentration at grid nodes will be employed, the immersed-boundary method, and a newly developed method, called the sharp-interface method in this thesis. Both methods will be described below. The accuracy of these methods will be discussed in Chapter Three.

2.3.1 Front-Tracking Method

The basis of the front-tracking method is quite simple. Two grids are used as shown in Figure 2.5: a stationary (Eulerian) finite difference mesh used to define the concentration; and a moving interface mesh used to track the interface. The interface mesh is represented by non-stationary Lagrangian computational points connected to form a one-dimensional line.

The basic structural unit is a line segment consisting of two adjacent points. The interface is represented by the vector parametric equation

$$\mathbf{R}(u) = g(u)\mathbf{i} + h(u)\mathbf{j}. \tag{2.12}$$

The normal, tangent and curvature at any point on the interface are found using the formulae

$$\mathbf{n} = \frac{-h'\mathbf{i} + g'\mathbf{j}}{\sqrt{g'^2 + h'^2}} \tag{2.13}$$

$$\mathbf{t} = \frac{g'\mathbf{i} + h'\mathbf{j}}{\sqrt{g'^2 + h'^2}} \tag{2.14}$$

$$\boldsymbol{\kappa} = \frac{g'h''\mathbf{i} - g''h'\mathbf{j}}{\left(g'^2 + h'^2\right)^{3/2}} \tag{2.15}$$

where the prime denotes differentiation with respect to the parameter u and **i** and **j** are unit vectors in the x- and y- directions, respectively. The normal is defined such that it is positive into the precipitate phase.

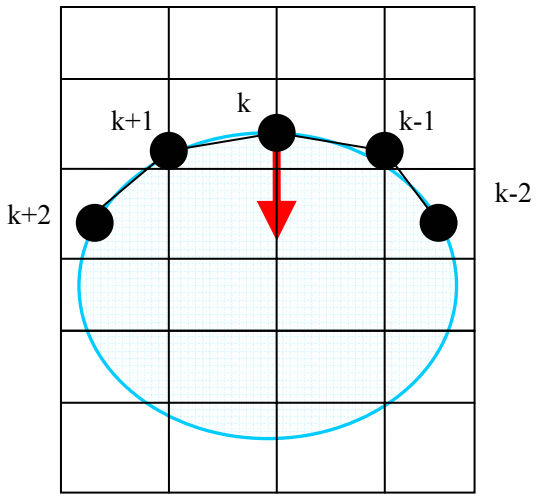

Figure 2.5 Two grids are used, a stationary Eulerian grid and a moving, Lagrangian grid to track the points. The normal direction is defined so that it is positive pointing into the precipitate and is calculated at each point using the four nearest neighbor points.

Since the location of the interface points is known, a fourth-order Legendre polynomial is fit to each interface point to develop the component functions g and h using its four nearest neighbors. A fourth order polynomial is constructed through five successive interface points $(x_f(u_i), y_f(u_i), i = 0,...,4$. Choosing the parameterization $u_i = i, i = 0,...,4$, the normal, tangent and curvature at the point $(x_f(u_2), y_f(u_2))$ are found using Equations (2.13) through (2.15) with the following expressions:

$$g_4'(u_2) = \frac{x_f(u_0) - 8x_f(u_1) + 8x_f(u_3) - x_f(u_4)}{12} \tag{2.16}$$

$$h_4'(u_2) = \frac{y_f(u_0) - 8y_f(u_1) + 8y_f(u_3) - y_f(u_4)}{12} \tag{2.17}$$

$$g_4''(u_2) = \frac{-x_f(u_0) + 16x_f(u_1) - 30x_f(u_2) + 16x_f(u_3) - x_f(u_4)}{12} \tag{2.18}$$

$$h_4''(u_2) = \frac{-y_f(u_0) + 16y_f(u_1) - 30y_f(u_2) + 16y_f(u_3) - y_f(u_4)}{12} \tag{2.19}$$

The interface is tracked using Lagrangian advection, such that a new point location can be found by:

$$\begin{aligned} x^{t+1} &= x^t + v_x dt \\ y^{t+1} &= y^t + v_y dt \end{aligned} \tag{2.20}$$

where v_x and v_y are the x and y components of the velocity, ds/dt, and dt is the time step used in the calculation. As the interface moves, it deforms and some parts become crowded with interface elements while the resolution of other parts becomes inadequate. In order to maintain accuracy, additional elements must either be added when the separation of the points becomes too large or the points must be redistributed to maintain adequate resolution. Small elements may be removed, which reduces the total number of elements and prevents the formation of fluctuations smaller than the grid size. To accommodate topology changes, interfaces are allowed to reconnect when either parts of the same interface or parts of two separate interfaces come close together. Since it is not well known at what distance the interface will coalesce when brought together and distances at such a small scale are not resolved, the interface is artificially reconnected when two points come closer than a small distance, p. Here the advantage of front-tracking is that the distance at which interfaces merge can be controlled and the effect of

varying p can be studied, unlike in interface capturing methods such as the phase-field [49] or level-set [48] methods where there is no active control over topology changes. However, it should be mentioned that p is not a physically known quantity, but an artificial parameter chosen by the user.

2.3.2 Immersed-Boundary Method

The immersed-boundary method was first developed by Peskin [54, 55] [55]and combined with front-tracking by Trygvasson and Aref [56]. The moving interface becomes immersed by combining the governing equations for the precipitate and matrix phases, resulting in one equation that accounts for both phases and the moving interface. Large jumps in concentration (as seen in Figure 2.3) and thermodynamic properties at the particle/matrix interface may cause instabilities in the solution of the governing equations for particle dissolution. Fortunately, a formulation employing a single diffusion equation can be written for both phases as long as the sharp changes in material properties and the rejection/absorption of solute at the interface is correctly accounted for. The concentration field for each alloying element must be transformed to create a continuous function. The concentration and diffusivity are transformed by the ratio $k_i = C_{P,Si} / C_{M,Si}$. Note that the subscript P refers to the precipitate phase and M refers to the matrix phase. The transformed initial condition is simply:

$$\tilde{c}_i = \begin{cases} C_{P,i}(x,y,0)/k_i, & \text{in the precipitate} \\ C_i(x,y,0), & \text{in the matrix} \end{cases}, \text{for } i \in (1,...,n) \tag{2.21}$$

and the diffusivity coefficients are transformed as follows:

$$\tilde{D}_{ij} = \begin{cases} k_i D_{P,ij}, & \text{in the precipitate} \\ D_{M,ij}, & \text{in the matrix} \end{cases}, \qquad \text{for } i, j \in \{1,...,n\} \tag{2.22}$$

The diffusion equation is rewritten in conservative form and expressed in terms of the transformed variables for $i \in \{1,...,n\}$:

$$\frac{\partial \tilde{c}_i}{\partial t} = \sum_{j=1}^{n} \nabla \cdot \tilde{D}_{ij} \nabla \tilde{c}_i + \int_f s_i \cdot \delta(\mathbf{x} - \mathbf{x_f}) dA, \tag{2.23}$$

where $\tilde{c}_i$ is the transformed concentration field, and $\tilde{D}_{ij}$ are the transformed volumetric diffusivity coefficients, s_i is the mass source of element i at the interface point $\mathbf{x_f}$, and $\delta(\mathbf{x} - \mathbf{x_f})$ is a two dimensional delta function that is nonzero only at the interface where $\mathbf{x} = \mathbf{x_f}$. The mass source term is appears as a result of recasting the two separate diffusion equations into one, and for an individual interface point it is given by:

$$s_i(x_f, y_f) = (C_{P,Si} - C_{M,Si}) \frac{ds}{dt} \tag{2.24}$$

where ds/dt is the velocity of point (x_f, y_f) and is determined by using the Stefan condition, given in equation (2.7) for alloying element i. In transformed concentration notation, the mass source becomes:

$$\tilde{s}_i(x_f, y_f) = C_{M,Si}(k_i - 1)\frac{ds}{dt} \tag{2.25}$$

Recall that k_i is simply the ratio of precipitate composition and matrix compositions at the interface for component *i*.

At each time step, information must be passed between the moving Lagrangian interface and the stationary Eulerian grid. Peskin's Immersed-Boundary Method [54] is used to pass this information because the discrete interface points (x_p) do not necessarily coincide with the Eulerian grid points (x_{ij}). Using this technique, the infinitely thin interface is approximated by a smooth distribution function that is used to distribute sources at the interface (due to rejection/absorption of solute, mass transfer across the interface, or surface tension, **f**) over several grid points near the interface. Considering mass transfer across the interface, *s(t)*, the interfacial source, m_k, can be distributed to the grid and the grid field variable, c_{ij}, can be interpolated to the interface using the discretized summation

$$m_{ij} = \sum_k m_k F_{ij}(x_k)\Delta s_k \tag{2.26}$$

where Δs_k is the average of the straight-line distance from the point *k* to the two points on either side of *k*, and F_{ij} is the Peskin [54] distribution function, defined as:

$$F_{ij} = \frac{\delta(x_{ij} - x_k)}{\Delta x}\frac{\delta(y_{ij} - y_k)}{\Delta y} \tag{2.27}$$

for two dimensions with grid spacing Δx, Δy. The delta function is defined by the following:

$$\delta(x) = \begin{cases} \delta_1(x), & |x| \le 1 \\ 1/2 - \delta_1(x), & 1 < |x| < 2 \\ 0, & |x| \ge 2 \end{cases} \tag{2.28}$$

and

$$\delta_1(x) = \frac{3 - 2|x| + \sqrt{1 + 4|x| - 4x^2}}{8}. \tag{2.29}$$

Similarly, the Peskin function is used to interpolate field variables from the stationary grid to the interface. For example, the concentration of the interface may be found by:

$$C_k = \sum_{ij} h^2 C_{ij} F_{ij}(x_k) \tag{2.30}$$

In this way, the front is given a finite thickness on the order of mesh size to provide stability and smoothness. There is also no numerical diffusion because this thickness remains constant for all time [44, 45, 52].

Different phases are identified by a step function, H, which is equal to one in phase 1 and two elsewhere. The interface is marked by a non-zero value of the gradient of the step function. Discontinuous material properties, such as density, are then expressed by:

$$\rho(x,y,t) = \rho_1 H(x,y,t) + \rho_2 (1 - H(x,y,t)) \tag{2.31}$$

where ρ_1 is the density in phase 1 $(H = 1)$ and ρ_2 is the density in phase 2 $(H = 0)$ (H=0).

An indicator function $H(x,t)$, is used to represent the step function. The jump in the indicator function across the interface is distributed using the grid points closest to the interface using Equation (2.26). This generates a grid-gradient field,

$$G(x) = \nabla H = \int_A n\delta(x - x_f)dA, \tag{2.32}$$

which is zero except near the interface, and has a finite thickness. The divergence of the gradient field, $(\nabla \cdot G)$, is found by numerical differentiation, using second-order centered differences. In this manner, the Laplacian of the indicator function is then calculated, and is again zero, except near the interface. The indicator function is found by solving the Poisson equation:

$$\nabla^2 H = \nabla \cdot G \tag{2.33}$$

At the end of each time step, the tracked interface elements are used to obtain the indicator function, H, at each grid point. The indicator function is constant within each material region, but has a finite-thickness transition zone around the interface and therefore approximates a two-dimensional step function. The primary advantage of this approach is that close interfaces can interact in a natural way since the gradients simply add or cancel as the grid distribution is constructed from the information carried by the

tracked front. Therefore, when two interfaces are close together, the full influence of the solute liberated from both interfaces is included in the diffusion equation.

2.3.3 Sharp-Interface Method

The sharp-interface method described here is based on the ghost-fluid method. The ghost-fluid method [57] is a useful way to calculate the gradients at the interface more accurately. Similar to the ghost-fluid method, in the sharp-interface method, the gradient for the matrix phase is extended into the precipitate for the purposes of calculating the diffusion of concentration in the matrix. Likewise, the gradient for the precipitate phase is extended into the matrix phase to calculate diffusion of solutal elements within the precipitate. This is accomplished by constant extrapolation in the direction normal to the interface, as seen in Figure 2.6.

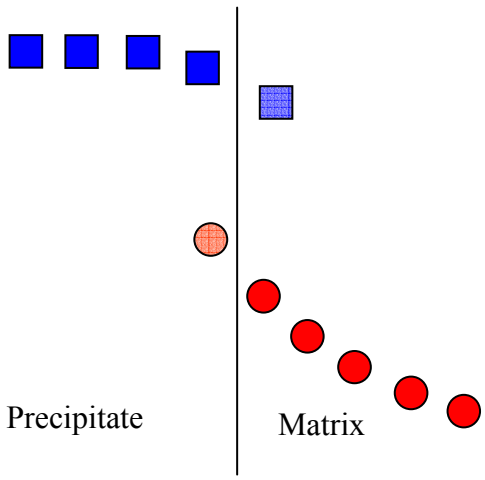

Figure 2.6 Gradients are extended into a ghost fluid for each phase for a more accurate calculation of interface values.

Consider the matrix phase, with diffusivity D. For simplicity, assume that the diffusivity is constant over the entire computation domain. The explicit finite-difference equation that characterizes the composition at node i,j for $\Delta x=\Delta y=h$, after a time step Δt, i

$$C_{i,j}^{t+1} = C_{i,j}^{t} + \frac{D\Delta t}{h^2}\left(C_{i-1,j} + C_{i,j-1} - 4C_{i,j} + C_{i+1,j} + C_{i,j+1}\right)^{t} \qquad (2.34)$$

Suppose that node i-1, j is located in the precipitate field. Instead of using the actual composition at that node, a "ghost" composition is calculated using the known composition and location of the interface. A schematic of this process is shown in Figure 2.7. The composition at one grid spacing from the interface ($x_f + \Delta x$) on the matrix side is interpolated using the nearest grid points. The grid node nearest the interface is not

used to extrapolate the composition in the ghost-matrix in order to avoid numerical instabilities if the distance between the grid node and the interface is too small. The interpolated composition and the interface composition are then used to extrapolate the composition at the grid node in the ghost-matrix.

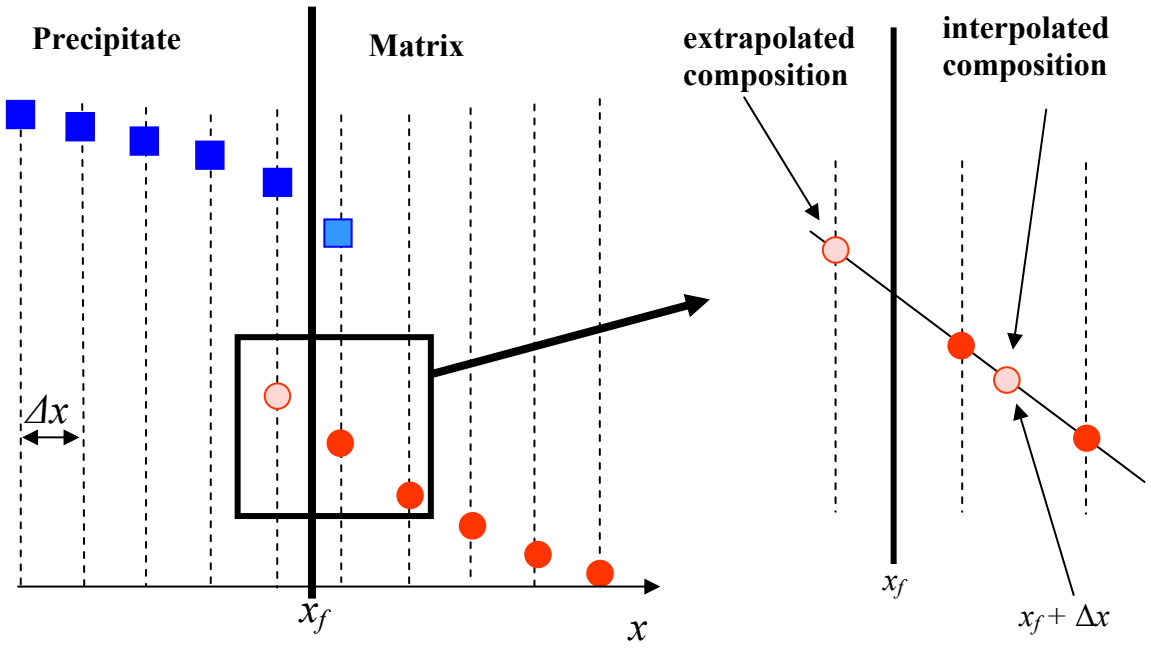

Figure 2.7 Schematic for extrapolating the composition of a ghost point for the matrix phase. First, the composition at $x_f + \Delta x$ is interpolated from the neighboring grid nodes The composition at the grid node behind the interface is then extrapolated using the known composition at the interface and the interpolated composition.

The composition at node i, j then becomes:

$$C_{i,j}^{t+1} = C_{i,j}^{t} + \frac{D\Delta t}{h^2}\left(C_{i-1,j} + C_{i,j-1} - 4C_{i,j} + C_{i+1,j} + C_{ghost}\right)^{t} \qquad (2.35)$$

where C_{ghost} is the "ghost" composition. The advantages of this method, as compared with the immersed-boundary front-tracking method, is that the gradients near the interface are expressed more accurately and the boundary is no longer immersed in the governing equations, thereby removing the necessity for the delta-function mass source term to account for the mass flow in the system.

2.4 Numerical Implementation

In order to begin the computation an initial interface shape is specified. From this shape the indicator function is constructed as described above in Section 2.3.3. The following must also be initialized: number of alloying components, initial composition fields of all components, diffusivity matrix, solution domain, and any boundary conditions (for instance, periodic boundaries or convective-source boundaries instead of no-flux boundaries). The interface compositions must then be found for each alloying element at each interface point based on the hyperbolic relation given in Equation (2.1) coupled with the Stefan conditions at the interface, given by Equation (2.7). A root-finding procedure must be used – in this work a Newton-Rhapson root-finding technique is used.

Using the initial interface compositions, the concentration and diffusivity fields are transformed using Equations (2.21) and (2.22). The procedure for the remaining time steps is given below.

1. The interface velocity at each interface point is calculated using Equation (2.7) for each of the individual components. All of the components should give identical results for velocity.
2. With the normal velocity, the mass source term for each interface point is then determined using Equation (2.25) and distributed to the stationary grid using the Peskin distribution function, as in Equation (2.26). Note that this step is unique to the immersed-boundary method. The sharp-interface method does not use mass source terms.
3. The concentration field is then calculated using the transformed diffusion equation, given in Equation (2.23). Finite-differencing schemes are used to discretize the differential terms. The discretization of the equations is shown in Appendix A. An explicit method has been employed, which is first order accurate in time and second order accurate in space.
4. The interface points are then advected using Equation (2.20) and the indicator function is calculated using an available fast Poisson equation solver (FISHPACK) for Equation (2.33).
5. The time step is advanced and new interface compositions are calculated for each individual component at each interface point, again using the Newton-Rhapson root-finding routine for the hyperbolic relation given in Equation (2.1) coupled with the Stefan conditions at the interface, given by Equation (2.7):

$$\sum_{j=1}^{n}\left(D_{P,1j}\frac{\partial C_1}{\partial \eta} - D_{M,1j}\frac{\partial C_1}{\partial \eta}\right) = (C_{P,1S} - C_{M,1S})\frac{ds}{dt}.$$

Return to Step 1 until the precipitate has completely dissolved or the final specified time has been reached.

CHAPTER THREE

APPLICATIONS FOR BINARY ALLOYS

3.1 Introduction

The physics behind the equations discussed earlier are described in detail in this chapter for a binary alloy composed of components A and B. In this system molecules of A and B form physical bonds, but do not react chemically. Therefore, this is a metallic or intermetallic solution or mixture. The majority component is called the solvent and the minority component the solute. For a given mass of m grams of binary alloy A-B, the mass of A and B are m_A and m_B, respectively, where $m_A+m_B=m$. The mass ratios are

$$C_A = \frac{m_A}{m}, \quad C_B = \frac{m_B}{m} \tag{3.1}$$

and are measures of the proportion of A and B, respectively, in the alloy and are known as the mass fraction or the concentration of each component in the alloy. Only one of the concentrations is needed to determine the composition of the alloy since $C_A+C_B=1$. The concentration of the solute, C_B, is typically used as the composition variable and will be used here.

Mass transfer arises from component segregation when there is a concentration gradient of solute in the solvent [Figure 3.1(a)]. In this example, the concentration of B, given by C_B, varies in one dimension (x) through the solution. The B atoms will diffuse

throughout the material until their concentration is the same everywhere. The movement of the B atoms is represented by a flux J, given by Fick's first law of diffusion:

$$J = -D_B \frac{\partial C_B}{\partial x} \tag{3.2}$$

where D_B is the diffusivity of chemical species B in A.

The number of B atoms that diffuse through plane 1, of Figure 3.1, with a flux of J_1 in a small time interval, Δt, will be $J_1 A \Delta t$. The number of atoms that leave plane 2, with a flux of J_2, during this time, is $J_2 A \delta t$. Since $J_2 < J_1$, the concentration of B within a volume of $A\delta x$ will have increased by:

$$\Delta C_B = \frac{(J_2 - J_1) A \Delta t}{A \Delta x} \tag{3.3}$$

For small Δx,

$$J_2 = J_1 + \frac{\partial J}{\partial x} \Delta x \tag{3.4}$$

so, in the limit as $\Delta t \rightarrow 0$,

$$\frac{\partial C_B}{\partial t} = -\frac{\partial J}{\partial x} \tag{3.5}$$

Substituting Fick's first law gives Fick's second law for a single-phase system:

$$\frac{\partial C_B}{\partial t} = \nabla \bullet \left(D_B \nabla C_B \right), \tag{3.6}$$

where the generalization to three dimensions has been made, which can be solved for the concentration profile using the appropriate initial and boundary conditions.

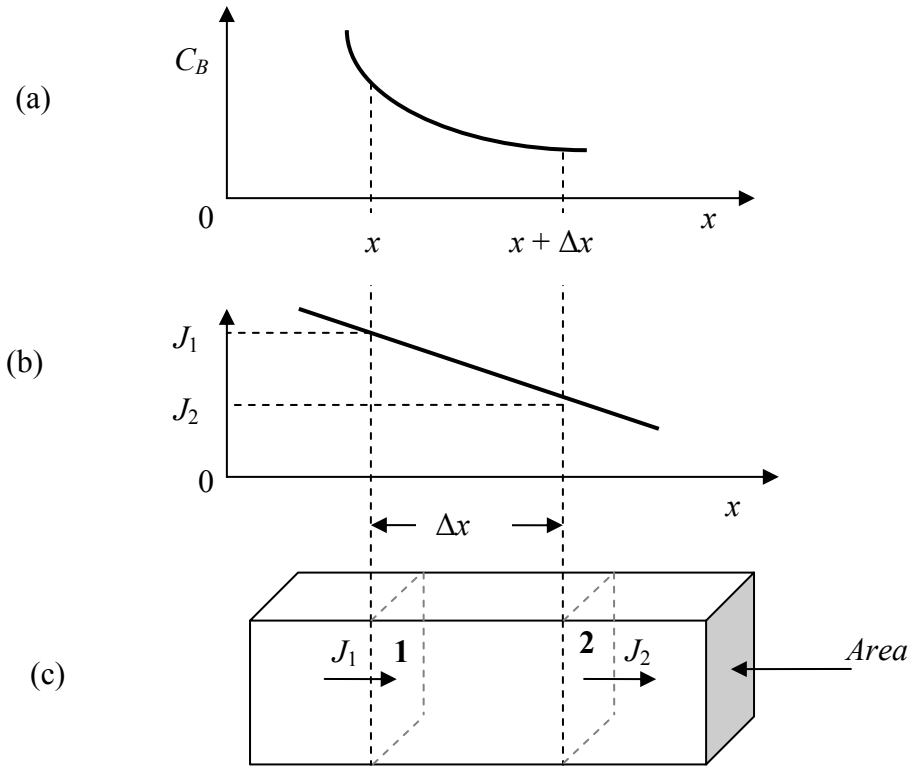

Figure 3.1 (a) Composition profile of component B. (b) Flux of component B. (c) Location of flux planes 1 and 2, and cross-sectional area for mass transfer, A.

In most practical cases, diffusion occurs in the presence of more than one phase. Consider a two-phase alloy composed of A and B that form an α-matrix interspersed with β precipitates. During the homogenization treatment β precipitates will dissolve. The B atoms will diffuse into the α-phase away from the α/β interface. The interface is not stationary but moves as diffusion progresses. An expression for the rate at which the boundary moves can be obtained as follows. Consider the planar α/β interface, shown in Figure 3.2. If a unit area of the interface moves a distance $\Delta\eta$, a volume ($\Delta\eta$•1) will be converted from β containing C_β B-atoms/m^3 to α containing C_α B-atoms/m^3. This means that a total of $\left(C_\beta - C_\alpha\right)\Delta\eta$ atoms of B must accumulate at the α/β interface, shown in the shaded area in Figure 3.2.

There is a flux of B-atoms towards the interface from the β-phase and a flux away from the interface in the α phase. In a time, dt, there will be an accumulation of B atoms at the interface given by:

$$\left\{\left(D_2 \left.\frac{\partial C_2}{\partial \eta}\right|_{\alpha/\beta}\right) - \left(D_1 \left.\frac{\partial C_1}{\partial \eta}\right|_{\alpha/\beta}\right)\right\} dt$$

where D_1 and D_2 are the diffusivity of B in the α-matrix (represented as phase 1) and β-precipitate (represented as phase 2) respectively, the concentration gradient of solute component B is taken normal to the α/β interface in both phases, and η indicates the direction normal to the interface.

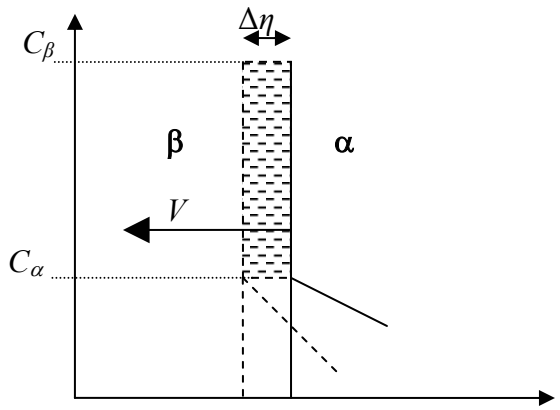

Figure 3.2 Concentration profile across the α/β interface and its associated movement.

The instantaneous velocity of the interface can then be found by equating the two expressions for accumulation at the interface:

$$v = \frac{ds}{dt} = \frac{1}{(C_\beta - C_\alpha)} \left\{ \left(D_2 \frac{\partial C_2}{\partial \eta}\bigg|_{\alpha/\beta} \right) - \left(D_1 \frac{\partial C_1}{\partial \eta}\bigg|_{\alpha/\beta} \right) \right\}. \qquad (3.7)$$

Note that the transfer of atoms across the α/β interface is assumed to be diffusion controlled. In some instances an interface reaction may control the motion of the interface and a different expression for interface velocity must be defined. For the current discussion, only cases where interface reactions may be neglected are considered.

To solve for the dissolution of the β precipitate, the diffusion equation for component B is coupled with the expression for the velocity of the interface. The solute equation is written for both phases separately as:

$$\frac{\partial C_1}{\partial t} = \nabla\left(D_1 \nabla C_1\right) \tag{3.8}$$

and

$$\frac{\partial C_2}{\partial t} = \nabla\left(D_2 \nabla C_2\right). \tag{3.9}$$

The alloy systems that will be discussed in this Chapter include Al-Cu and Al-Si. The composition in the precipitate phases is assumed to be constant, and the diffusion equation is solved within the precipitate with a diffusivity of zero.

3.2 One Dimensional Systems

One-dimensional solutions were developed for planar, cylindrical, and spherical precipitate geometries. These three geometries are illustrated in Figure 3.3. In the planar case, a planar precipitate with an initial half-thickness x_0 and composition C_P dissolves in a matrix of size L and composition C_M. The solution domain begins in the center of the precipitate$\left(x = 0\right)$. For the spherical and cylindrical geometries, a precipitate of initial radius r_0 and composition C_P is dissolving in a surrounding matrix of radius r_{L} and composition C_M. Again, the solution domain begins at the center of the precipitate for the cylindrical and spherical geometries. The interface composition is denoted by C_S.

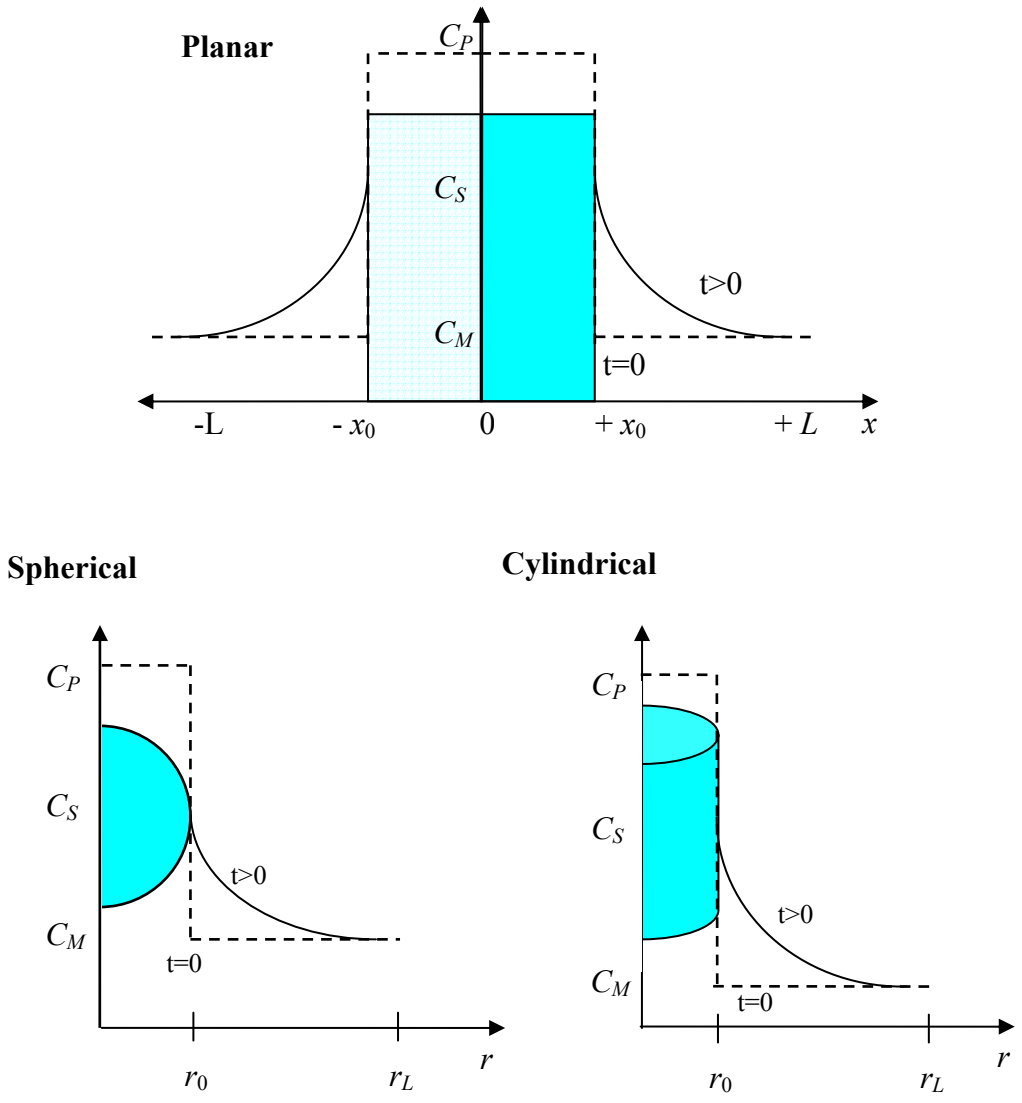

Figure 3.3 Schematic of solution geometry for one-dimensional planar, spherical and cylindrical solutions. C_P, C_M, and C_S are the precipitate, matrix and interface compositions, respectively.

The concentration profile of B in the system can be found by solving the following one-dimensional diffusion equation for solute in each phase:

$$\frac{\partial C}{\partial t} = \frac{D}{r^a}\frac{\partial}{\partial r}\left(r^a \frac{\partial C}{\partial r} \right) \tag{3.10}$$

where a is a geometrical parameter, which is 0, 1, and 2 for planar, cylindrical, and spherical geometries, respectively. The equations are coupled at the interface location, $s(t)$ through the Stefan condition, Equation (3.7). There are two separate fields for which the diffusion equation must be solved: within the precipitate and within the matrix.

The boundary conditions for all three one-dimensional solutions are given by:

$$\begin{aligned} &C(0 < x < s(t), t) = C(0 < r < s(t), t) = C_P \\ &\left.\frac{\partial C}{\partial x}\right|_{x=L} = \left.\frac{\partial C}{\partial r}\right|_{r=r_L} = 0 \end{aligned} \tag{3.11}$$

and the initial conditions are:

$$\begin{aligned} &C(0 < x < x_0, 0) = C(0 < r < r_0, 0) = C_P \\ &C(x_0 < x < L, 0) = C(r_0 < r < r_L, 0) = C_M \end{aligned} \tag{3.12}$$

where the composition in the matrix may be a function of distance. The interface condition, in addition to the flux condition, given in Equation (3.7), is given by:

$$C(s(t),t) = C_S \tag{3.13}$$

for all three geometries.

3.2.1 Comparison with Exact Solution

The immersed-boundary and sharp-interface front-tracking methods which were described in Chapter Two were compared to determine the best method to perform the simulations. In the immersed-boundary method, a single diffusion equation is written for the entire solution domain. Because of this, the particle/matrix boundary is "immersed" and source terms must be included in the governing equations. In the sharp-interface method, "ghost" fluids are used to calculate the diffusion in the matrix near the precipitate/matrix interface. There is no need to combine the governing equations for the entire flow field and thus the source terms are no longer needed.

The simulations to compare the two front-tracking methods were run using a precipitate composition of 33 at.%, an interface composition of 2.24 at.% and an initial composition in the matrix of 0 at%. The diffusivity value used was 0.1 μm^2/sec. These values were chosen because they are similar to conditions for the Al-Cu system. The precipitate half-thickness was chosen as 3 μm, and the length of the computational domain was set to 30 μm.

Analytical solutions only exist for very specific cases of particle dissolution. The solutions are for one-dimensional problems in infinite or semi-infinite domains, with simple initial conditions and constant diffusivity, D. These are similarity solutions, and

are functions of $\frac{x - x_f(t)}{\sqrt{t}}$, where x_f(t) is the interface location, and x and t are the spatial and temporal variables, respectively [58]. Following Carslaw and Jaeger [58], the interface location as a function of time for a planar particle dissolving in an infinite domain is given by:

$$x_f(t) = x_f(0) + 2\lambda\sqrt{Dt}\,, \tag{3.14}$$

and the composition is expressed as:

$$C(x,t) = C_M + \frac{C_S - C_M}{\text{erf}(\lambda)}\text{erf}\left(\frac{x - x_f(t)}{2\sqrt{Dt}}\right) \tag{3.15}$$

where, λ is found by solving the transcendental equation,

$$\lambda\sqrt{\pi}\exp(-\lambda^2) = -\frac{C_s - C_M}{(C_P - C_S)\,\text{erfc}(\lambda)}\,. \tag{3.16}$$

Figure 3.4 shows the interface location as a function of time for the exact solution and both front-tracking methods. The front-tracking methods were very close to each other; in fact, it is difficult to tell them apart in Figure 3.4. The absolute errors between the front-tracking methods and the exact solution are shown in Figure 3.5. Initially the immersed-boundary method has a smaller error than the sharp-interface method. However, the immersed-boundary method quickly develops a larger error than the sharp-

interface method. The error has been defined as the absolute difference between the exact solution interface location and the interface location calculated by front-tracking The maximum error in interface location was larger for the immersed-boundary method than for the sharp-interface method.

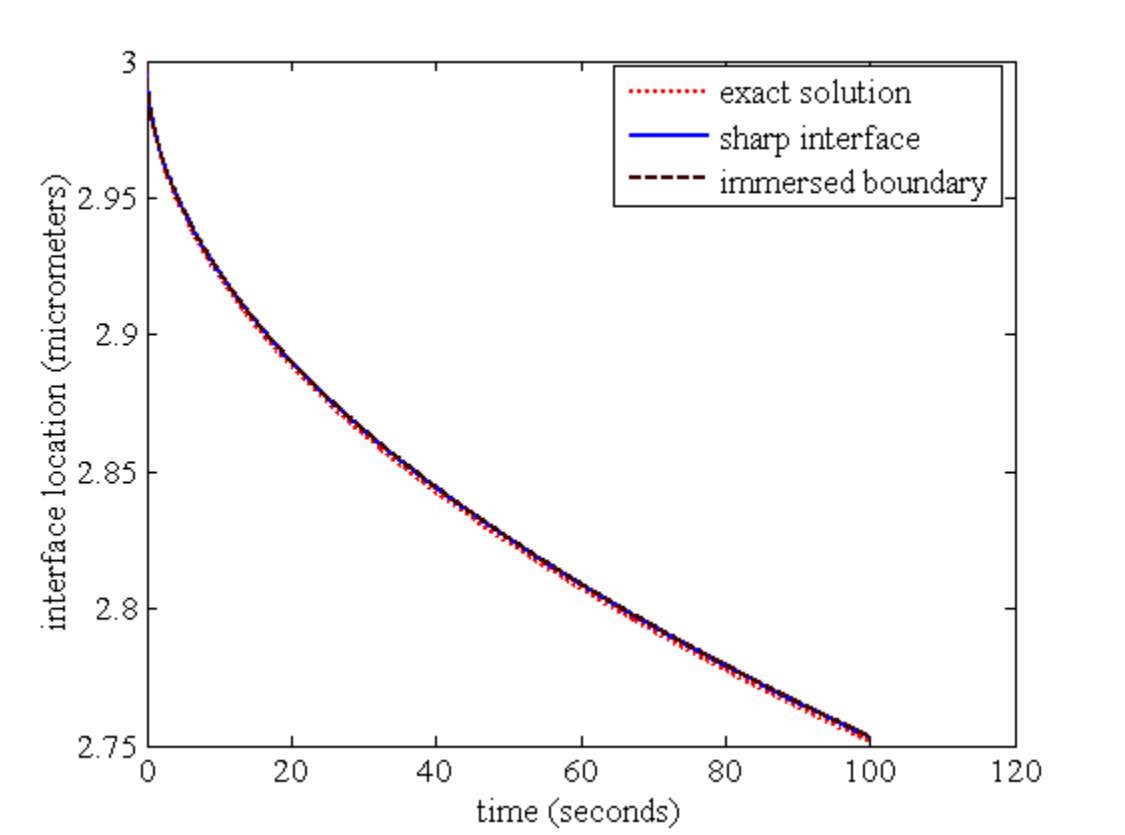

Figure 3.4 Interface location as a function of time for the exact solution (dotted line), sharp-interface method (solid line) and immersed-boundary method (dashed line). Both of the front tracking methods gave similar results, their interface locations were just slightly higher than the analytical solution. The simulations were run using: dx = 0.05, C_P = 33 at.%, C_S =2.24 at.% , C_M =0 at%, D = 0.1 μm2/sec, $x_f(0) = 3\,\mu m$, and L = 30 μm.

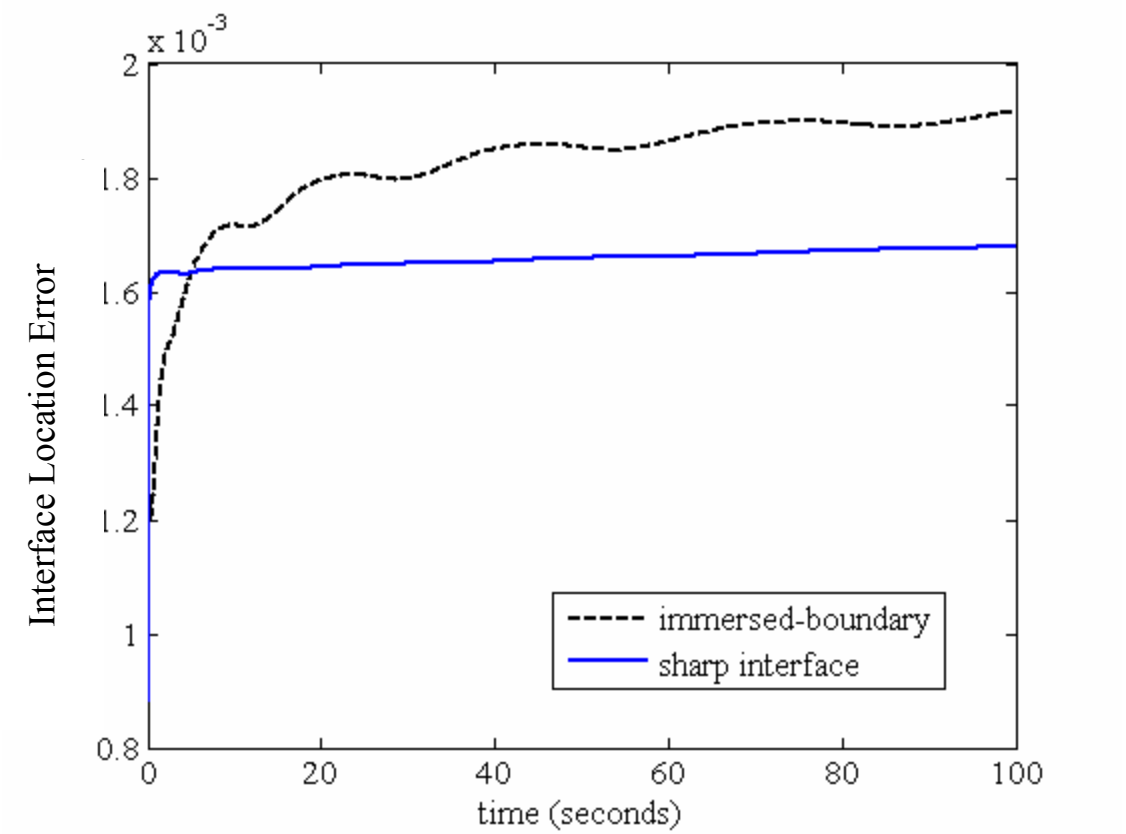

Figure 3.5 Absolute error in interface location for the immersed-boundary (dashed line) and sharp-interface (solid line) methods. The immersed-boundary method shows a greater error in interface location than the sharp-interface method. The simulations were run using: dx = 0.05, C_P = 33 at.%, C_S =2.24 at.% , C_M =0 at%, D = 0.1 μm2/sec, $x_f(0) = 3\,\mu\text{m}$, and L = 30 μm.

Another important aspect in the calculation is mass conservation. For the method to be accurate, it must conserve mass globally at every time. Figure 3.6 shows the mass in the system for both front-tracking methods. The immersed-boundary method, shown in the dashed line, decreases initially and then levels off, while the sharp-interface method remains constant throughout time. The sharp-interface method performs better in terms of mass-conservation than the immersed-boundary method.

An additional advantage of the sharp-interface method is shown in Figure 3.7, in which the composition profiles are shown at t = 10 seconds. The immersed-boundary method has a spike in concentration at the interface. This spike is due to the delta-function source term that is located at the interface. The spike becomes smaller as the grid size is reduced, however it does not completely disappear. The sharp-interface method does not have these spikes, so it is preferable to the immersed-boundary method.

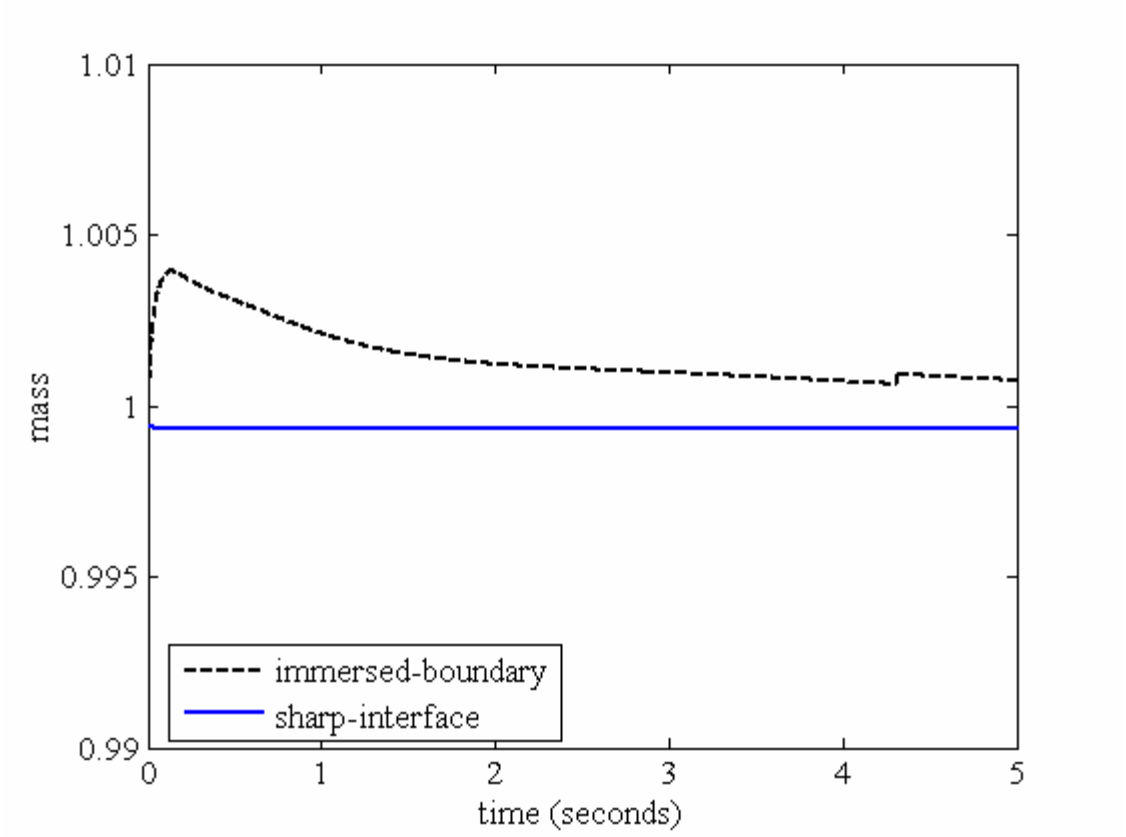

Figure 3.6 Total mass in system over time for the immersed-boundary method (dashed line) and sharp-interface method (solid line). The immersed-boundary method quickly gains mass and then starts to lose mass. The sharp-interface method maintains mass consistently over the entire temporal domain. The simulations were run using: dx = 0.05, C_P = 33 at.%, C_S = 2.24 at.% , C_M = 0 at%, D = 0.1 μm2/sec, $x_f(0) = 3\,\mu\text{m}$, and L=30 μm.

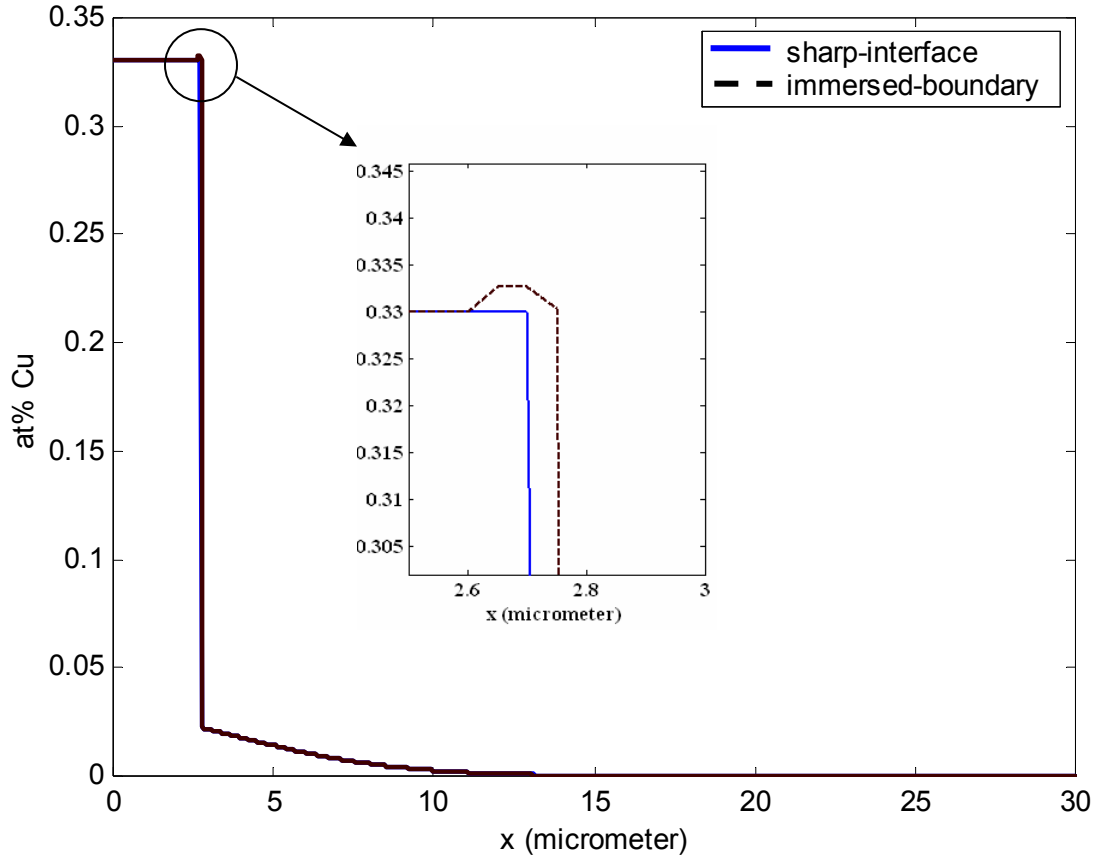

Figure 3.7 Comparison of composition profile at 100 seconds for sharp-interface and immersed-boundary methods. The composition at the particle/matrix interface is enlarged to show the spike in composition for the immersed-boundary method. The simulations were run using: C_P = 33 at.%, C_S = 2.24 at.% , C_M = 0 at%, D = 0.1 μm2/sec, $x_f(0) = 3\,\mu\text{m}$, and L = 30 μm.

Error norms have been plotted for the difference in composition between the exact solution and the two front-tracking methods. They are defined as:

$$L_1 = \frac{1}{m}\sum_{i=1}^{m}\left|e_i\right| \tag{3.17}$$

$$L_2 = \left[\frac{1}{m}\left(\sum_{i=1}^{m}\left|e_i\right|^2\right)\right]^{1/2} \tag{3.18}$$

$$L_\infty = \max\left|e\right| \tag{3.19}$$

where m is the number of data, and e_i is the error of point i. The L_1, L_2, and L_∞ concentration norms are plotted in Figures 3.8-3.10 respectively. In all three cases, the error norm is higher for the immersed-boundary method than for the sharp-interface method. In Figure 3.8, both methods appear to have the same trend for the L_1 norm, however the immersed-boundary method has higher values at all times. The immersed-boundary method has a decreasing L_2 norm, while the L_2 norm for the sharp-interface method is increasing; however the sharp-interface method does have a lower value throughout the computational time (see Figure 3.9). In Figure 3.10, the L_∞ composition norm for both front-tracking methods is shown. The immersed-boundary method has a much higher L_∞ error than the sharp-interface method. It is obvious that the sharp-interface method out-performs the immersed-boundary method over the entire solution domain.

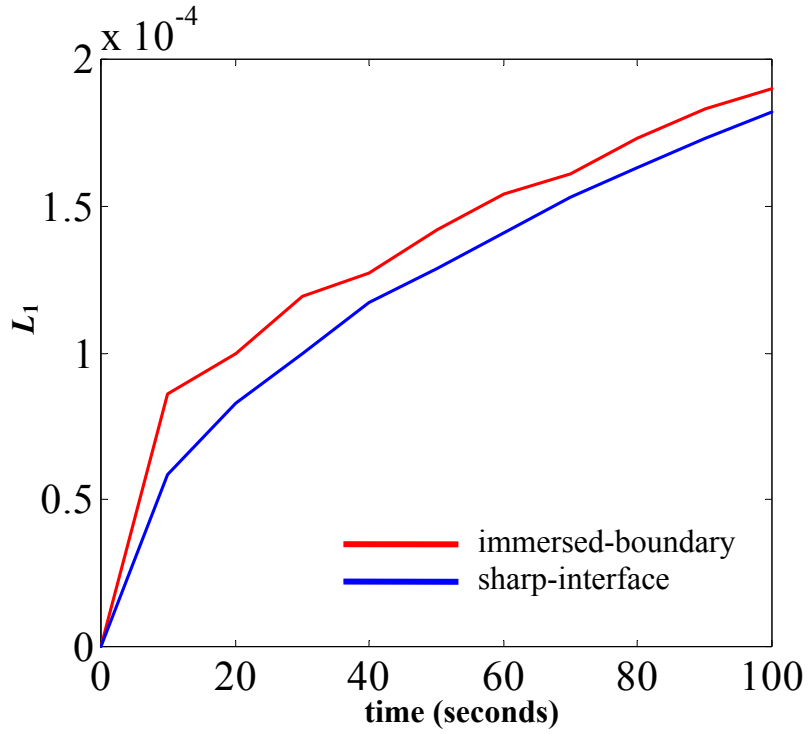

Figure 3.8 L_1 composition norm for immersed-boundary (red line) and sharp-interface (blue line) methods. The L_1 norm is higher at all solution times for the immersed-boundary method. The simulations were run using: C_P = 33 at.%, C_S = 2.24 at.% , C_M = 0 at%, D = 0.1 μm2/sec, $x_f(0) = 3\,\mu\text{m}$, and L = 30 μm.

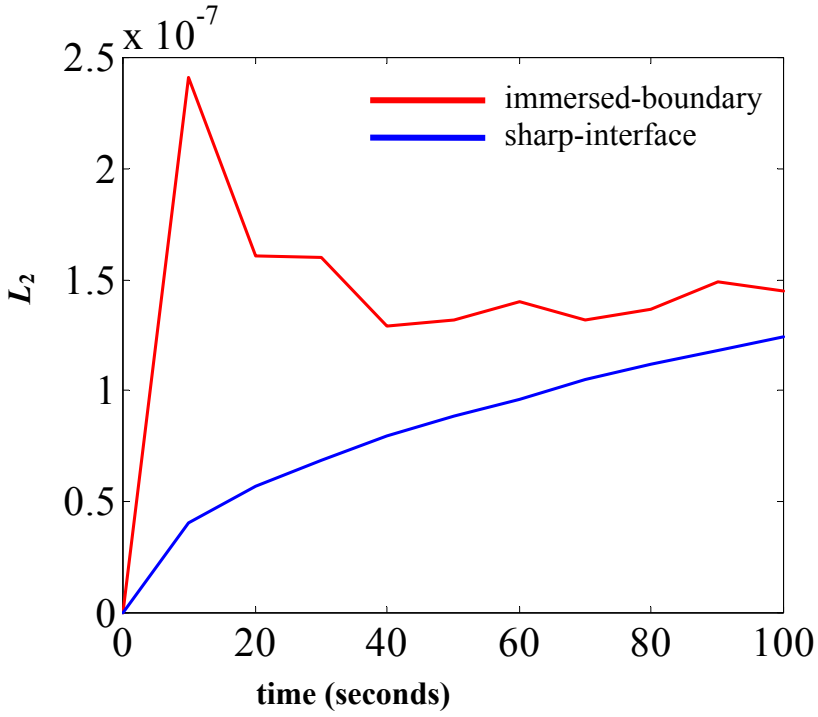

Figure 3.9 L_2 composition norm for immersed-boundary (red line) and sharp-interface (blue line) methods as a function of time. The L_2 norm is higher at all solution times for the immersed-boundary method, although they seem to be converging to the same value. The simulations were run using: C_P = 33 at.%, C_S = 2.24 at.% , C_M = 0 at%, D = 0.1 μm2/sec, $x_f(0) = 3\,\mu\text{m}$, and L = 30 μm.

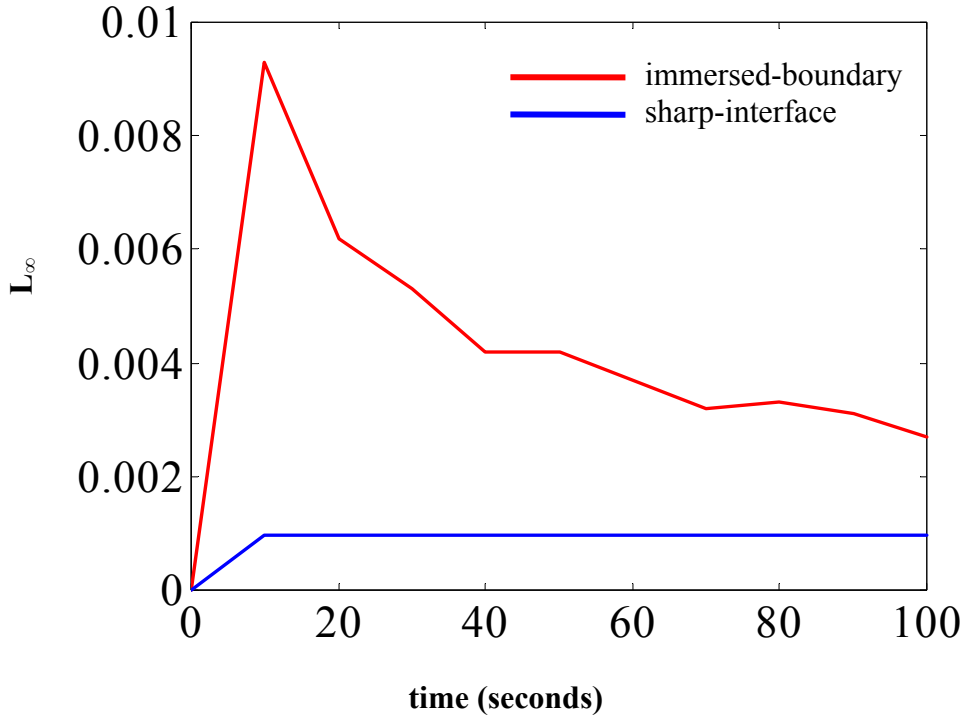

Figure 3.10 L_∞ composition norm for immersed-boundary (red line) and sharp-interface (blue line) methods. The L_∞ norm is much higher at early times for the immersed-boundary method, and is constant (after the initial time) throughout the solution time for the sharp-interface method. The simulations were run using : C_P = 33 at.%, C_S = 2.24 at.% , C_M = 0 at%, D = 0.1 μm2/sec, $x_f(0) = 3\,\mu\text{m}$, and L = 30 μm.

Grid convergence was also tested for the immersed-boundary and sharp-interface methods. Figure 3.11 shows the grid convergence for the L_∞ composition error norm. The sharp-interface method has nearly quadratic convergence and the immersed-boundary method has nearly linear convergence. Quadratic convergence is expected because the finite-difference method used to calculate composition values is second-order accurate. The mass error as a function of grid spacing is shown for the sharp-interface method in Figure 3.12. The error is reduced as the grid size is reduced, as expected.

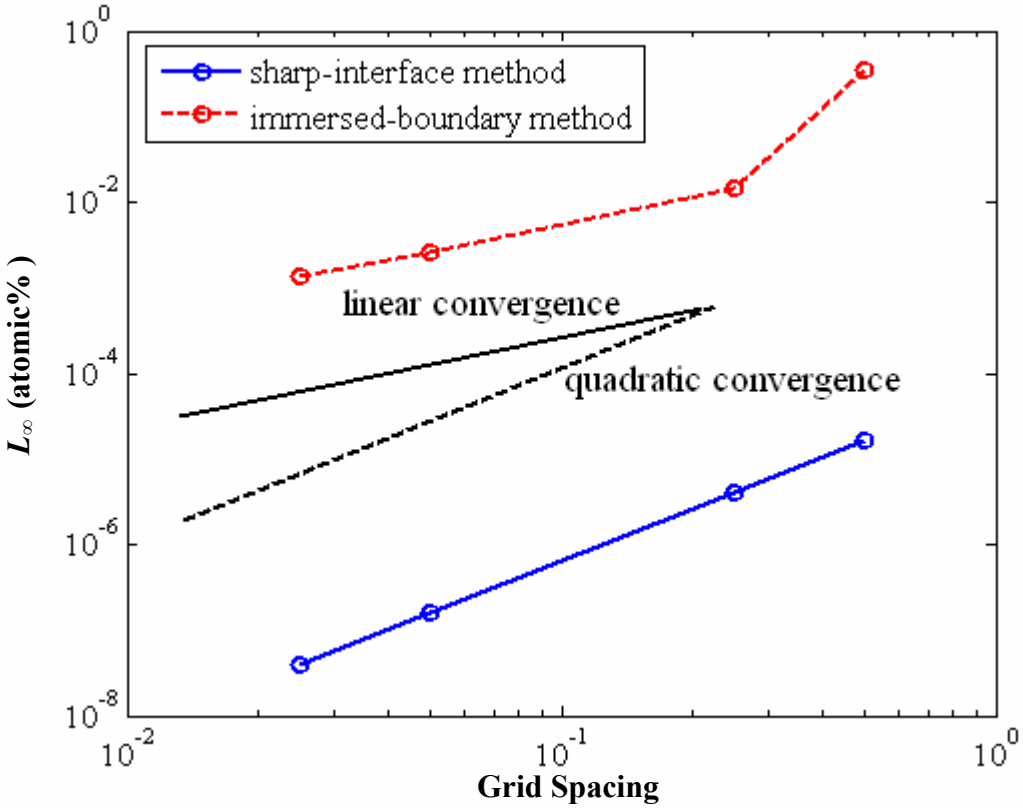

Figure 3.11 L_1 and L_2 composition error norms for the sharp-interface (solid line) and immersed-boundary (dashed line) methods at time=100 seconds. The sharp-interface method shows nearly quadratic convergence, and the immersed-boundary method shows between linear and quadratic convergence. The simulations were run using: C_P = 33 at.%, C_S = 2.24 at.% , C_M = 0 at%, D = 0.1 μm2/sec, $x_f(0) = 3\,\mu\text{m}$, and L = 30 μm.

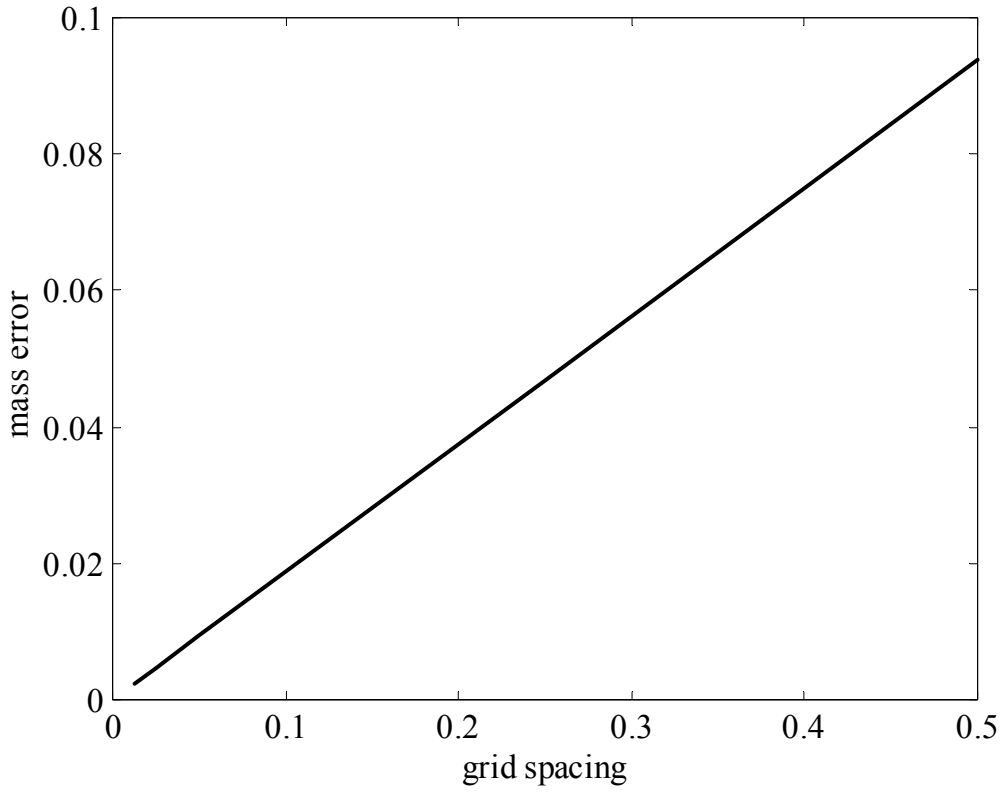

Figure 3.12 Sharp-interface mass error plotted as a function of grid resolution (dx=0.5,0.25, 0.05, 0.025, and 0.0125). The simulations were run using : C_P = 33 at.%, C_S = 2.24 at.% , C_M = 0 at%, D = 0.1 μm2/sec, $x_f(0) = 3\,\mu\text{m}$, and L = 30 μm.

The sharp-interface front-tracking method has been chosen for the remaining calculations in this thesis. It has outperformed the immersed-boundary method in both composition calculations and mass conservation. Both factors may be attributed to the delta-function source-terms that are inherent to the immersed-boundary method. The sharp-interface method is also more efficient – performing at a clock speed of almost three times faster than the immersed-boundary method. This enhanced efficiency is needed when moving into two-dimensional simulations.

3.2.2 Comparison with Literature Models

Aaron and Kotler [37] considered one-dimensional diffusion-controlled dissolution of a planar precipitate in a semi-infinite domain. Under the assumption that the interface location was a slowly varying function of time, they calculated the interface location to be:

$$x_f(t) = x_f(0) - k\sqrt{\frac{Dt}{\pi}} \tag{3.20}$$

where k is a supersaturation parameter given by:

$$k = 2\frac{C_S - C_M}{C_P - C_S} \tag{3.21}$$

where C_P, C_S, and C_M are the composition in the precipitate, the precipitate/matrix interface, and the matrix, respectively. According to Aaron and Kotler, in order for the interface location to be a slowly varying function with time, k must be less than 0.3.

Figure 3.13 shows Aaron & Kotler's [37] method compared with the exact solution and both front-tracking methods. The simulations were run using: $C_P = 33\,\text{at\%}$, $C_S = 2.24\,\text{at\%}$, $C_M = 0\,\text{at\%}$, $D = 0.1\,\mu\text{m}^2/\text{s}$, $x_f(0) = 3\ \mu\text{m}$, and $L = 30\ \mu\text{m}$. The supersaturation parameter, k, is equal to 0.14564. It is obvious from Figure 3.13 that Aaron and Kotler's method diverges very quickly from the exact solution, which is somewhat surprising considering that k is well within the limits of their model's applicability. The divergence from the exact solution is most likely due to the assumption that the interface-location is a slowly varying function with time.

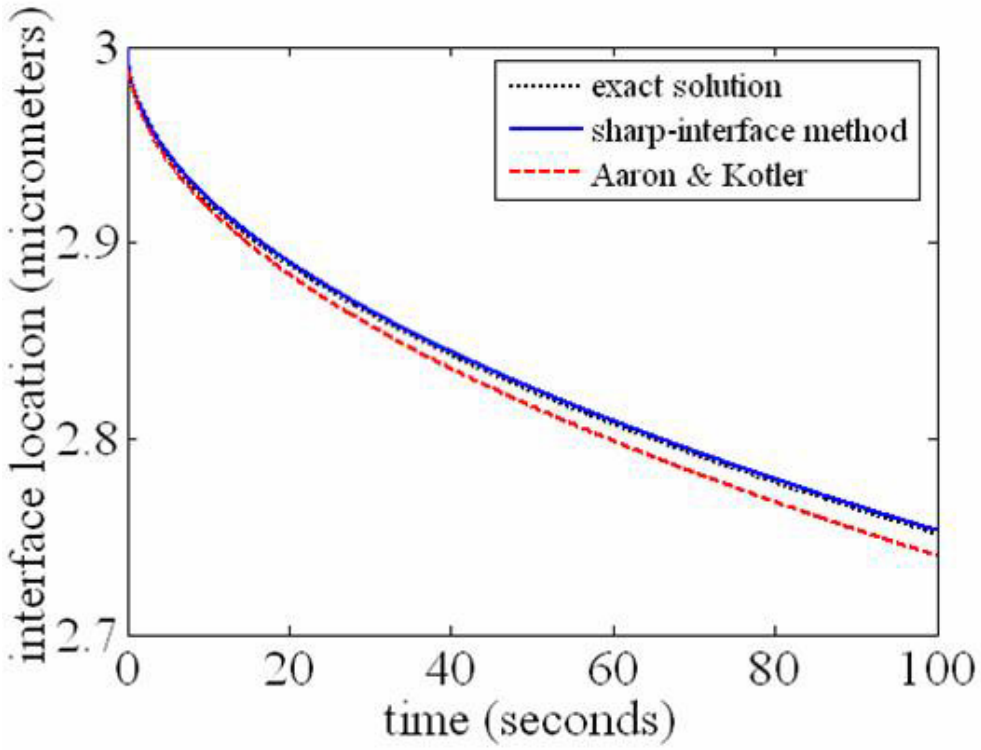

Figure 3.13 Interface location as a function of time, showing the exact solution (dotted line), sharp-interface method (solid line), immersed-boundary method (dashed line), and Aaron & Kotler's approximation (dash-dot line). Aaron and Kotler's expression has diverged from the other solutions at an early time due to the assumptions in their analysis. They assumed that the interface was a slowly varying function with time. The simulations were run using : $C_P = 33\,\text{at\%}$, $C_S = 2.24\,\text{at\%}$, $C_M = 0\,\text{at\%}$, $D = 0.1\,\mu\text{m}^2/\text{s}$, $x_f = 3\ \mu\text{m}$, and $L = 30\ \mu\text{m}$.

Whelan [36] considered the dissolution of a spherical precipitate and posed that it was approximately the reverse of growth at long times. His analysis was similar to that of Aaron and Kotler [37] for the planar particle. They approximated the dimensionless half-thickness at early times to be:

$$\frac{r}{r_0} = 1 - \frac{kDt}{2r_0^2} - \frac{k}{r_0}\sqrt{\frac{Dt}{\pi}} \tag{3.22}$$

Figure 3.14 shows the Whelan equation (dashed line) plotted with the radius determined by the spherical one-dimensional sharp-interface front-tracking method. The Whelan solution predicts a slower dissolution time than the sharp-interface method. Whelan's solution does not take into account the changing interfacial area for mass transfer. The area available for mass transport increases with radial distance from the center of the sphere. Therefore, as the sphere becomes small, the dissolution rate increases, which is observed in the sharp-interface method profile.

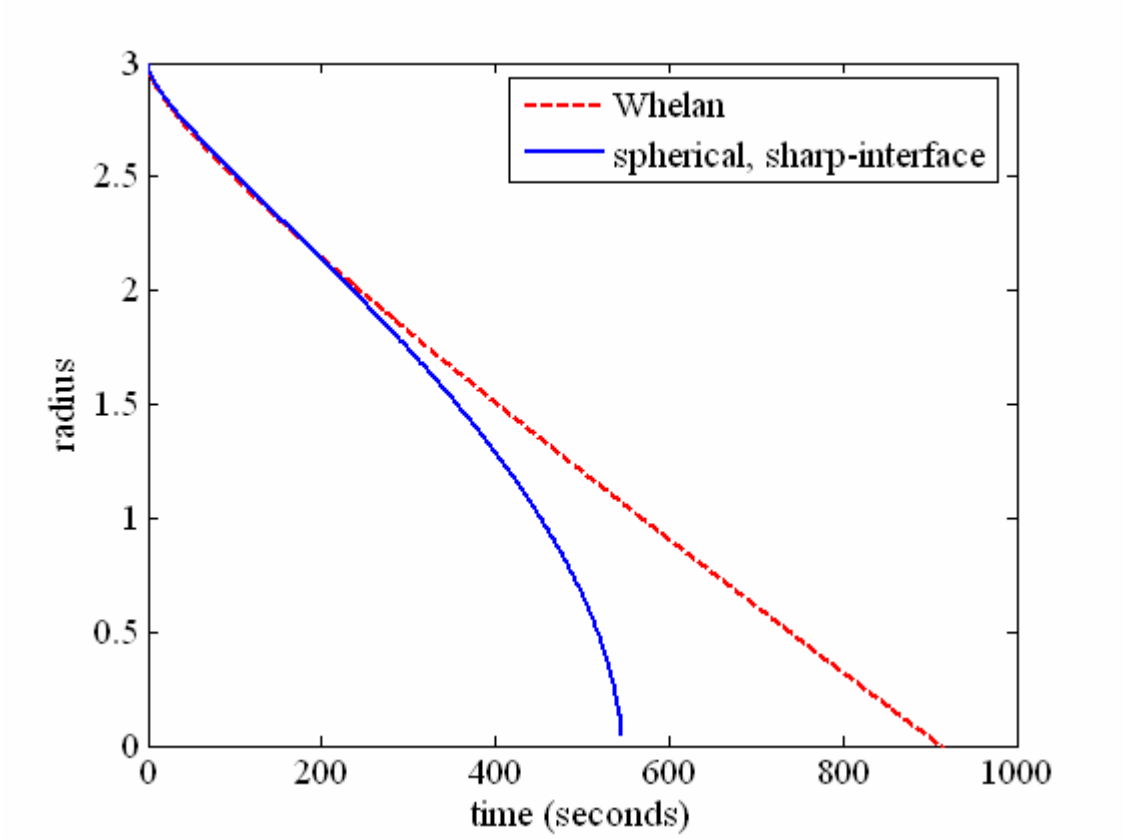

Figure 3.14 Whelan correlation plotted with sharp-interface spherical model. The Whelan correlation initially shows a slightly lower interface radius position, however as time continues, Whelan's model predicts a longer dissolution time than the spherical model. The simulations were run using: $C_P = 33\,\text{at\%}$, $C_S = 2.24\,\text{at\%}$, $C_M = 0\,\text{at\%}$, $D = 0.1\,\mu\text{m}^2/\text{s}$, $r_0 = 3\ \mu\text{m}$, and $r_L = 30\ \mu\text{m}$

3.3 Two Dimensional System

Two-dimensional simulations were performed, using the parameters shown in Tables 3.1 and 3.2. In all cases, the two-dimensional simulations were run using a circular precipitate in a matrix, shown in Figure 3.15. This geometry was chosen because it is a convenient shape, however any two-dimensional precipitate shape can be used. The concentration profile of B in the system can be found by solving Equations (3.8) and (3.9). The equations are coupled at the interface location, $s(t)$ through the Stefan condition, Equation (3.7). There are two separate fields for which the diffusion equation must be solved: within the precipitate and within the matrix. Within the precipitate, there is a no-flux condition at the center ($x=x_c$, $y=y_c$):

$$\frac{\partial C_2}{\partial x} = \frac{\partial C_2}{dy} = 0, \text{ at } (x_c, y_c) \tag{3.23}$$

and there are also no-flux conditions imposed on all outer boundaries of the matrix phase:

$$\frac{\partial C_1}{\partial x} = \frac{\partial C_1}{dy} = 0, \text{ at } \begin{cases} (0, 0 \le y \le y_L) \\ (x_L, 0 \le y \le y_L) \\ (0 \le x \le x_L, 0) \\ (0 \le x \le x_L, y_L) \end{cases} \tag{3.24}$$

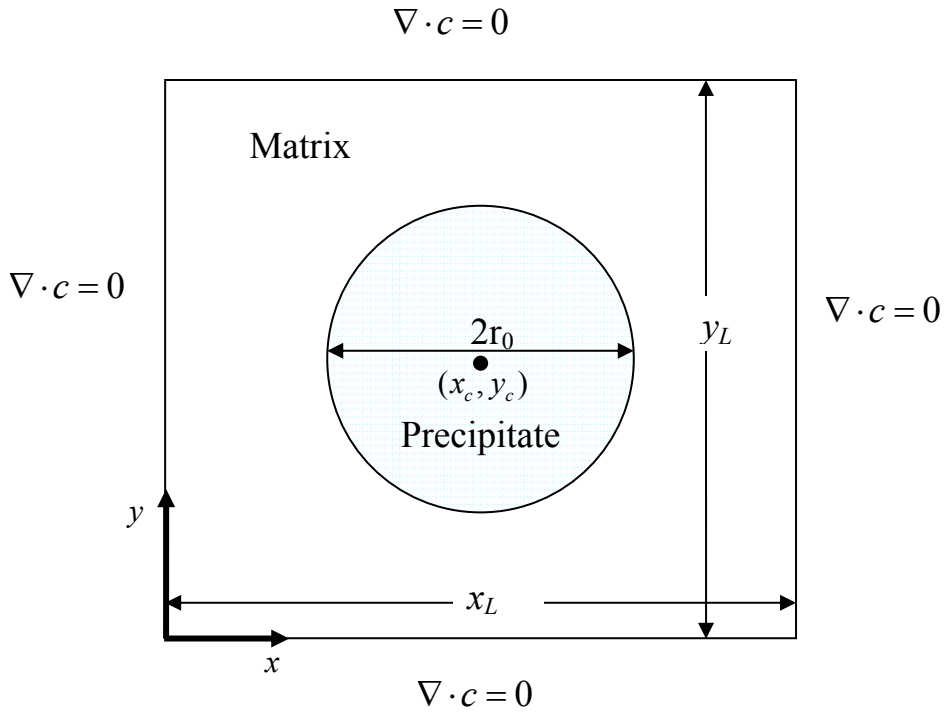

Figure 3.15 Solution domain for dissolution of a circular precipitate in an alloy. There are no-flux conditions on all outer boundaries of the solution domain.

3.3.1 Comparison with Experimental Data

There are three main issues to consider when comparing models with experimental data: (1) the diffusivity of the solute in the solvent, (2) shape of precipitates, and (3) size distribution of precipitates. In all cases where models were compared to experimental data, the diffusivity value reported by the author was used. There is uncertainty involved in these numbers which may affect the final result. The diffusivity values found in the literature were reported to have less than 5% error, which is not

enough of a difference to affect the dissolution time. Additionally, the shape of the precipitates is a factor that must be considered. If the particle is spherical in shape, the spherical model will be the obvious choice. Two-dimensional simulations are needed when more than one particle is being considered, or particle spacing is an issue. The one-dimensional models assume a uniform size, shape, and distribution of precipitates. Another factor is that the reported experimental information is for a distribution of various sizes of precipitates. The one-dimensional models can only account for one particle at a time, so again, two-dimensional simulations are needed. Note that in this chapter, only one particle will be considered in a given matrix.

The sharp-interface method was compared with experimental data found in the literature for Al_2Cu platelets dissolving in an Al-Cu alloy [59, 60], for θ' dissolving in an Al-Cu alloy [18], and for Si particles dissolving in an Al-Si alloy[13]. The simulations were run using the parameters listed in Tables 3.1 and 3.2. The diffusivities for each simulation are given in Table 3.1, along with the precipitate and interface compositions. The geometric parameters used for the simulations are given in Table 3.2 for each case. In all two-dimensional simulations in this section, the geometry shown above in Figure 3.15 was used. This geometry translates to an infinitely long cylinder dissolving in an infinitely long square bar.

Table 3.1 Boundary conditions and diffusivities for binary alloy simulations found in Reiso *et al*. [60],(ROR), Baty *et al*. [59], (BTH), and Hewwitt and Butler[18], (HB), Tundal and Ryum[13], (TR).

Precipitate	Half thickness or radius	Volume fraction	C_P (at. fraction)	C_S (at. fraction)	diffusivity (μm^2/sec)	Source
Al_2Cu/θ	3 μm	0.015182	0.33	0.0224	0.1	ROR
Al_2Cu/θ	0.3 μm	0.025	0.33	0.0224	0.0603	BTH
Al_2Cu/θ'	0.25 μm	0.019	0.33	0.00857	$6.43X10^{-4}$	HB
Si	1.89 μm	0.0037	0.8289	0.0079	0.131	TR
Si	1.89 μm	0.0037	0.8289	0.0104	0.288	TR
Si	1.89 μm	0.0037	0.8289	0.0136	0.6	TR

Table 3.2 Geometry for simulations using parameters found in Reiso *et al*. [60], Baty *et al*. [59] Hewitt and Butler[18],and Tundal and Ryum[13].

Experiment	Geometry	1D planar	1D cylindrical	1D spherical	2D, cylindrical precipitate
ROR	x_0, r_0 (μm)	3	3	3	3
	L, r_L (μm)	197	24	12	43 x 43
BTH	x_0, r_0 (μm)	0.3	0.3	0.3	0.3
	L, r_L (μm)	12	1.897	1.025	3.36 x 3.36
HB	x_0, r_0 (μm)	0.25	0.25	0.25	0.25
	L, r_L (μm)	13	1.8	0.94	2.8 x 2.8
TR-a , TR-b, TR-c	x_0, r_0 (μm)	1.89	1.89	1.89	1.89
	L, r_L (μm)	510.81	31.07	12.22	55 x 55

Reiso, Overlie, and Ryum [60] investigated the dissolution of Al_2Cu in an Al-4.2 wt%-Cu alloy. The alloy was produced by directional solidification and was then homogenized 4 days at 530°C and subsequently broken down by cold rolling with intermediate annealing at 430°C. The specimens were then annealed for 2 hours at 530°C in air. The temperature was then decreased by 1°C/hour down to 450°C, after which the specimens were quenched in water. To observe dissolution of the Al_2Cu precipitates, a series of up-quenching experiments to 546°C were run. The area fraction of precipitates was measured on an optical microscope using an interactive image analysis system instrument. Dissolution data was digitized using "digiMatic" software. The percent-area fraction of precipitate is shown as a function of time in Figure 3.16. The two-dimensional model was run using a circular precipitate in a matrix, and shows good agreement with the experimental data. The solution geometry chosen is akin to an infinite cylinder dissolving in an infinite box of square cross-section with end effects neglected. Al_2Cu precipitates are plate-like in shape, and as they dissolve, the sharp edges will soften, so this geometrical choice is reasonable. The one-dimensional planar model is also compared with the experimental data shown in Figure 3.16, and overshoots the dissolution time.

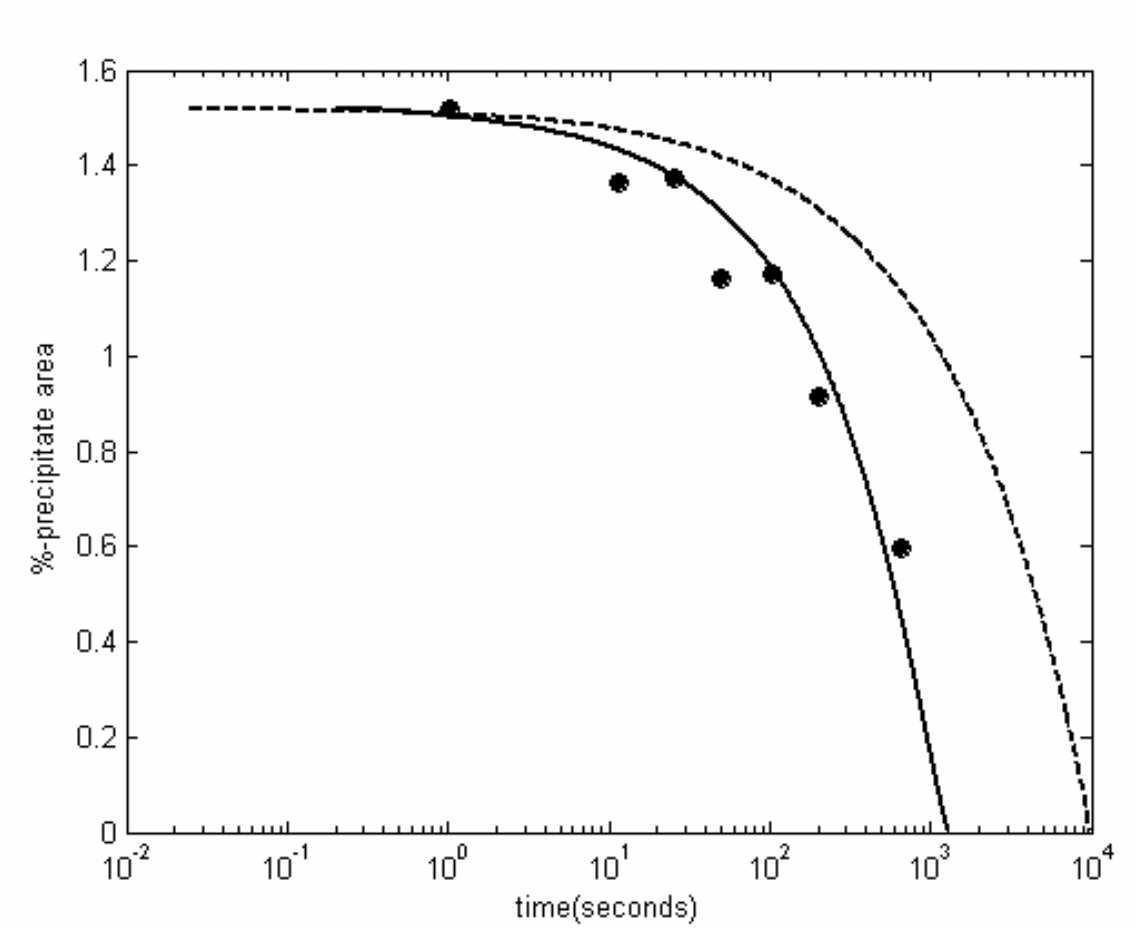

Figure 3.16 Two-dimensional model (solid line) and planar model (dashed line) compared with Reiso *et al*.'s experiment (●).

Baty, Tanzilli, and Heckel [59] studied the dissolution of Al_2Cu in an Al-4wt%-Cu alloy. They developed large Al_2Cu particles during a heat treatment of 35 hours at 300°C. Small particles were developed by solution heat treatment at 560°C for 46 hours followed by cold working 50% and aging for 200 hours at 200°C. The samples were then heat treated at 520°C and 540°C to study the evolution of the Al_2Cu particles. Point counting was used to determine the volume fraction of Al_2Cu after each heat treatment. Size distributions were calculated using DeHoff analysis. The reduction in particle size during heat treatment was determined by two different ways. The first was volume fraction of Al_2Cu particles in the matrix. The second was by determining the mean particle size from the particle size distributions. The data were plotted in dimensionless parameters: dimensionless radius, $\frac{r}{r_0}$, vs. dimensionless time, $\frac{D \cdot t \cdot C_S^{1.1}}{r_0^{\,2}}$. In order to compare the experimental data with our models, it was necessary to determine the time in seconds from the dimensionless time. The data were digitized using digiMatic software. The two-dimensional model shows good agreement with the experimental data, as observed in Figure 3.17.

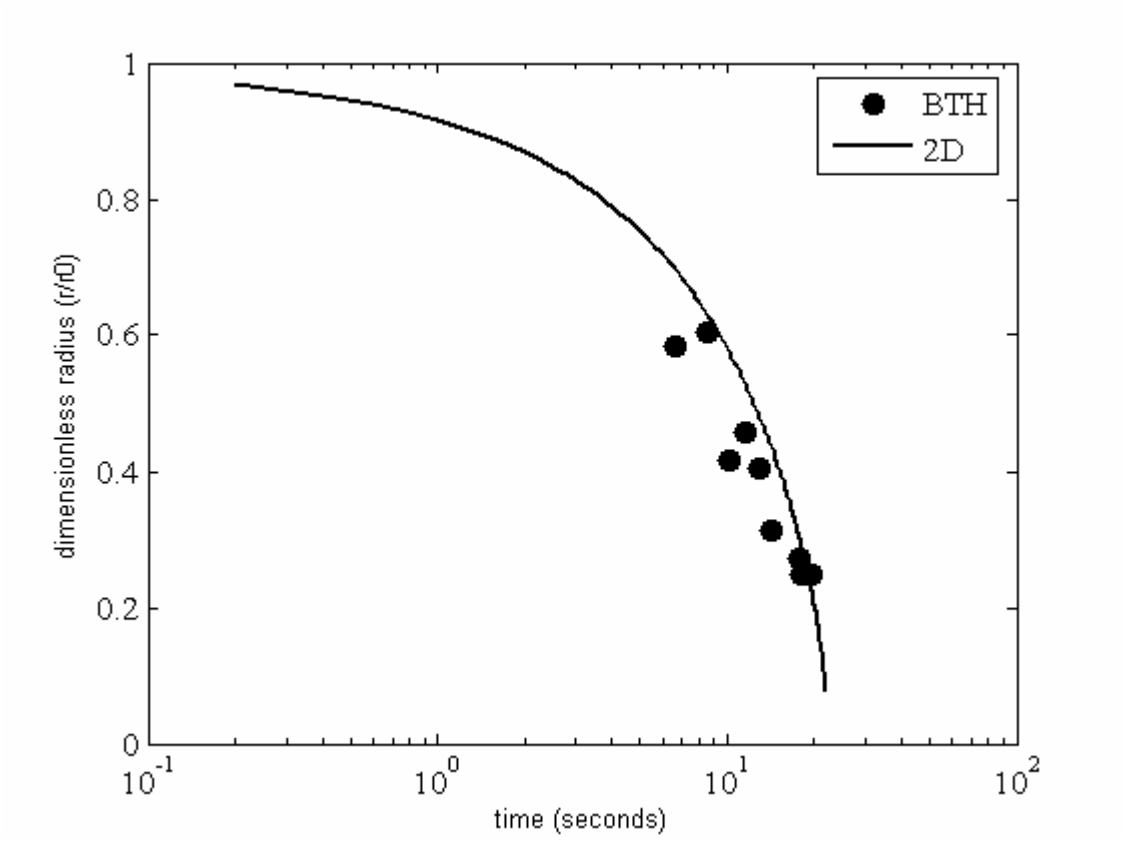

Figure 3.17 Data compared with experiment from Baty, Tanzilli and Heckel[59]. The two-dimensional model shows good agreement with the experimental data.

Hewitt and Butler[18] investigated the dissolution of θ′ in an Al-3wt%-Cu alloy. The alloy was solution heat treated at 550°C for 30 minutes, water quenched and aged at 285°C for 22 hours to produce a microstructure consisting of two size dispersions of θ′. The samples were then observed during a heat treatment at 370°C in a high voltage electron microscope. A timed sequence of micrographs was obtained using a data acquisition system and the area of θ′ at each time step was determined using stereometric analysis software. Hewitt and Butler observed disk-like particles θ′ dissolving. The two-dimensional model and the one-dimensional spherical model are compared with the data digitized from Figure 2 in Hewitt and Butler[18]. The spherical model shows good agreement with the data points, while the two-dimensional model overshoots the dissolution time.

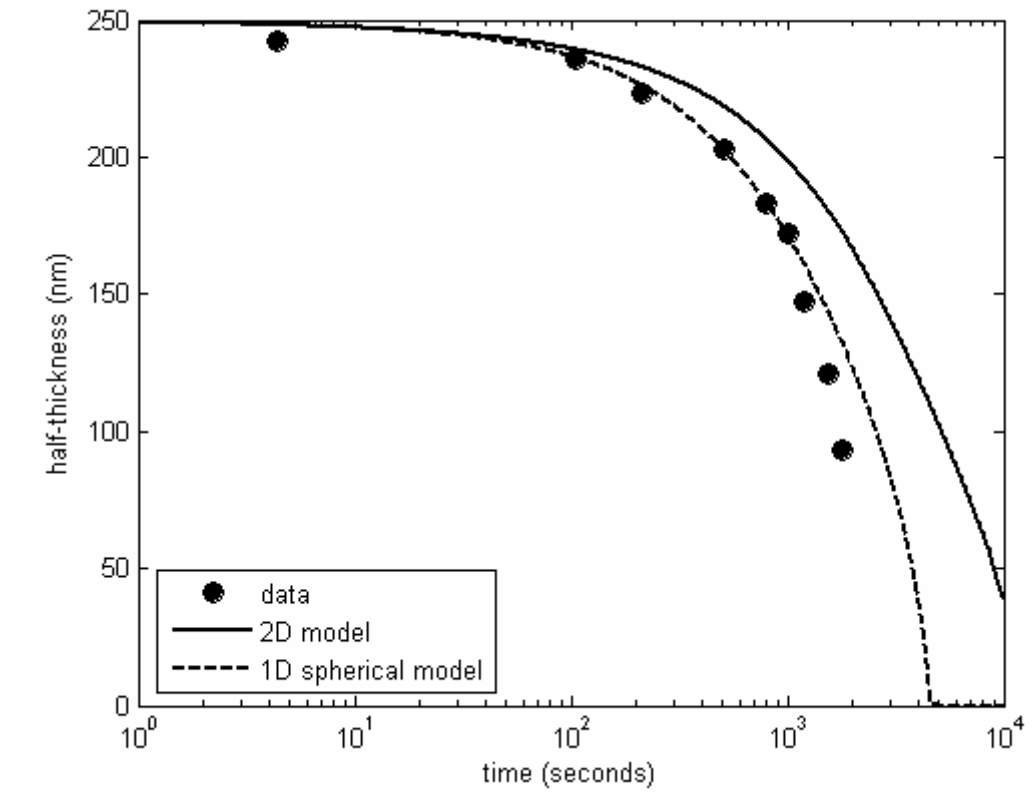

Figure 3.18 Simulations compared with data found in Hewitt and Butler[18]. The one-dimensional spherical sharp-interface model shows very good agreement with the experimental data at early times. The two-dimensional model overshoots the dissolution time, likely due to geometry.

Tundal and Ryum[13] studied the dissolution of silicon particles in an Al-0.8wt%-Si alloy[13]. The casting was homogenized for 48 hours at 580°C. The alloy was then heat treated at 490°C for 24 hours, 70% cold rolled, held for four hours at 490°C, cooled at 1°C/hour to 450°C and heat treated for another 48 hours. Samples were then heat treated in a salt bath to various temperatures above the solvus temperature in order to study the dissolution. After the heat treatment, the samples were quenched in cold water. The particle sizes after each heat treatment were determined using a semiautomatic image analyzer, and were found to be generally circular in shape in the planar sections. The area fraction of precipitates found using image analysis was then plotted with dimensionless time, $\frac{2Dkt}{r_0^2}$, where k is a measure of the supersaturation.

Tundal and Ryum[13] observed spherical particles dissolving with an average radius of 1.89 μm, which was chosen as the input for the spherical model. Their data are compared with our model in Figure 3.19. For all three temperatures, the experimental dissolution time is longer than the calculated dissolution time. Again, the simulations were carried out using the average radius determined experimentally by Tundal and Ryum. However, in reality there is a distribution in the size of precipitates dissolving. At large times, the larger particles will dominate the experimental data. Smaller particles dissolve faster and do not enter into the experimental determination of average radius. In Figure 3.20, three initial radii (1.89, 2.835, and 3.78 μm) are compared to the experimental data for 530°C. The curves for the larger radii each go through an experimental datum point, which confirms that particles larger than the average initial radius take longer to dissolve. The spherical model does not take into account more than

one precipitate. In order to predict the dissolution time of a distribution of particles, either a distribution of particles, or the largest particle radius should be used.

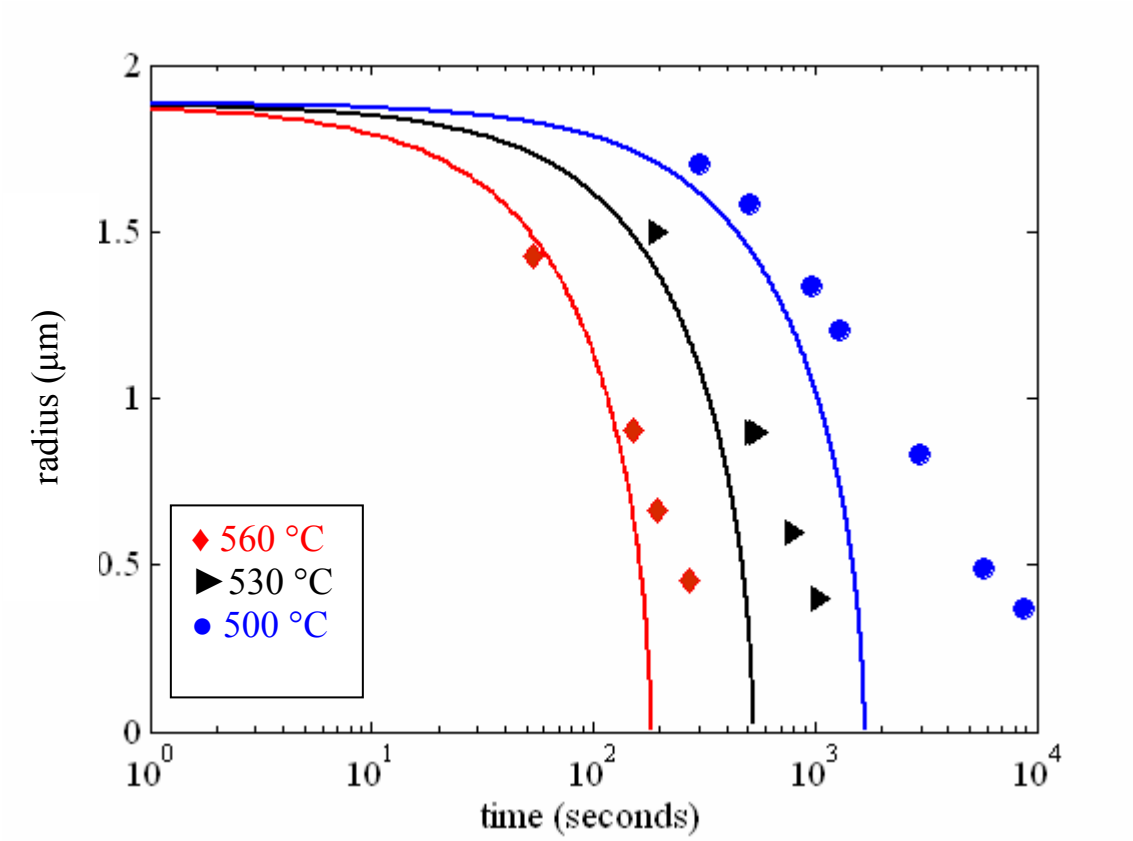

Figure 3.19 Model comparison with experimental data from Tundal and Ryum [13]. Spherical silicon particles were observed dissolving in an aluminum matrix at 560 °C (♦), 530 °C (▶) and 500 °C (●). The experimental data overshoot the spherical model for all three temperatures.

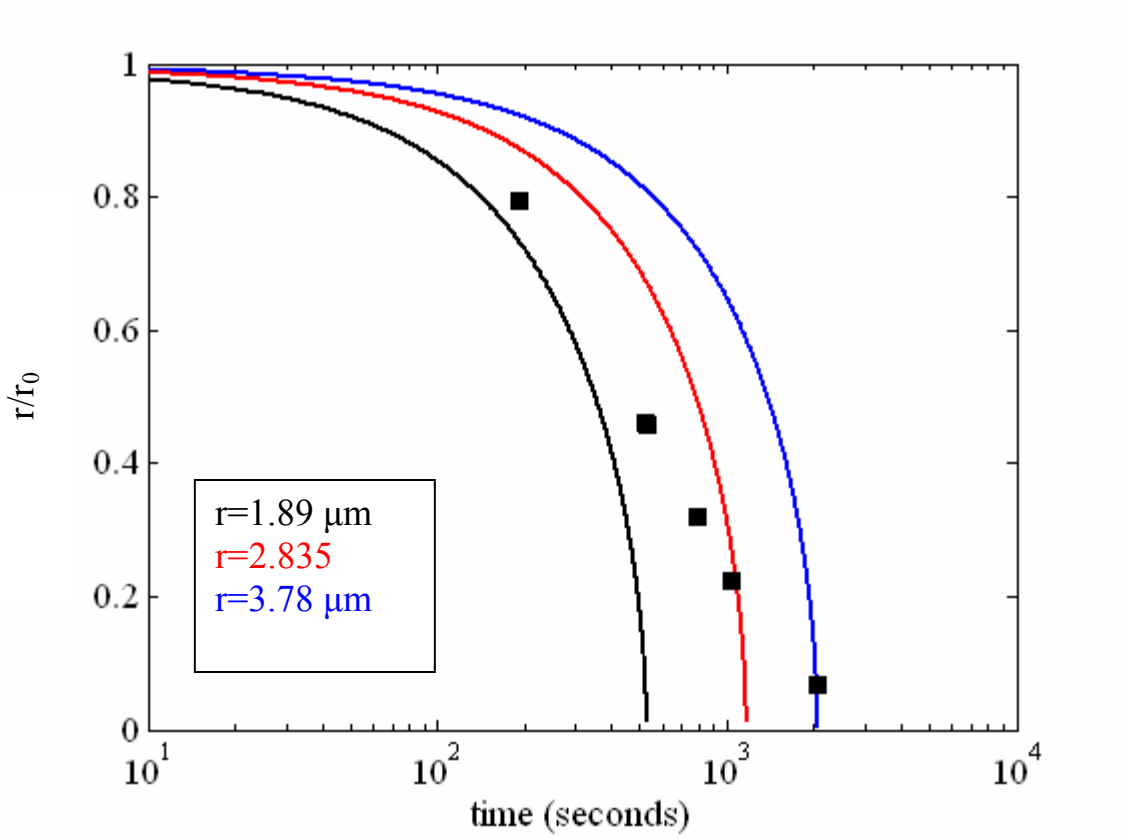

Figure 3.20 Spherical silicon particles dissolving at 530°C (■) compared with spherical dissolution model using an initial radius of 1.89 μm (black line), 2.835 μm (red line) and 3.78 μm (blue line). Experimental data taken from Tundal and Ryum [13].

3.4 Summary

Two front-tracking techniques, the immersed-boundary and the sharp-interface methods, were compared with an exact solution for a one-dimensional planar-dissolution problem. The interface location as a function of time, mass conservation as a function of time, and concentration profiles were compared for each method. Both front-tracking methods performed well with respect to interface location; however, the immersed-boundary method deviated more from the exact solution than the sharp-interface method. The sharp-interface method was also shown to conserve mass better than the immersed-

boundary method. Furthermore, when composition profiles of the two front-tracking methods were compared with the exact solution, the sharp-interface method out-performed the immersed-boundary method. The composition error norms for the immersed-boundary method were all higher than those for the sharp-interface method. Furthermore, the sharp-interface method showed the expected second-order accurate convergence when subjected to a standard grid-reduction study. The immersed-boundary method showed slightly less than quadratic convergence. An additional advantage of the sharp-interface method is that it is more efficient and faster than the immersed-boundary method because the source terms are no longer necessary.

The sharp-interface front-tracking model was then compared with dissolution models found in the literature, as well as experimental results for precipitate dissolution in binary alloys. A semi-analytic planar-dissolution model, developed by Aaron and Kotler [37], was compared with the one-dimensional planar sharp-interface method and the exact solution. Aaron and Kotler's method was shown to predict a faster dissolution time, due to assumptions inherent in their analysis. Whelan's [36] semi-analytical spherical-dissolution model was also compared with the one-dimensional spherical sharp-interface model. His spherical model predicted a longer dissolution time than the sharp-interface method. Whelan's analysis was for a spherical particle dissolving in an infinite domain, and Aaron and Kotler's analysis was for a planar particle, also dissolving in an infinite domain. The motion of the moving interface was not accounted for in either study, causing the discrepancy between their models and our sharp-interface model.

Four sets of experimental data were found in the open literature for dissolution of second-phase particles in aluminum alloys. Two sets of experimental data were found for dissolution of θ in the aluminum copper alloy system. The two dimensional model performed well when compared with both sets of data. Reiso *et al*.'s [60] experiments were performed with an Al-4.2Cu alloy with an initial average precipitate radius of 3 μm. Baty *et al*.[59] considered dissolution of θ in an Al-4Cu alloy, with an average initial precipitate radius of 0.3 μm. The model was able to capture the dissolution kinetics at both of these precipitate sizes. The spherical model performed very well when compared with Hewitt and Butler's [18] experiments on dissolution of θ′ in an Al-3Cu alloy. The two dimensional model was also compared with Hewitt and Butler's experimental data and predicted a much longer dissolution time. This result enforces that the shape of the dissolving precipitate must be taken into consideration to obtain accurate description of the dissolution kinetics. The model was also compared with Tundal and Ryum's [13] experiments on dissolution of spherical silicon particles in an Al-Si alloy. The average initial radius reported by Tundal and Ryum was used to run the simulations for three different temperatures, using the spherical model. In all three cases, the spherical model under-predicted the dissolution time. Tundal and Ryum observed a distribution of precipitates dissolving in the matrix. The smaller particles will dissolve first, so at large times the experimentally determined average radius will be dominated by the largest particles. Therefore, a distribution of particles should be incorporated into the model in order to obtain a more accurate description of the system.

CHAPTER FOUR

APPLICATIONS FOR TERNARY ALLOYS

4.1 Introduction

Most industrially relevant alloys contain more than two components; therefore it is important to consider dissolution in multi-component alloys. Because of the complexities associated with multi-component alloys, there are no experimental results available. This chapter will focus on data from the Al-Mg-Si system where data are available for the diffusivity values. First the governing equations will be discussed and applied to the dissolution problem using the one-dimensional spherical model. The effects of particle spacing and size distributions on the dissolution of Mg_2Si will then be investigated.

The hyperbolic relationship between interfacial concentrations in this case may be expressed by:

$$\left(C_{Mg,S}\right)^2 \left(C_{Si,S}\right)^1 = K(T) \tag{4.1}$$

where the subscript S refers to interfacial values, Mg and Si refer to magnesium and silicon, respectively, and $K(T)$ is the solubility product constant. The exponents on the interfacial composition are taken from the precipitate stoichiometry. For simplicity, consider dissolution of Mg_2Si in a one-dimensional spherical domain. The interfacial flux relationships, neglecting cross-diffusion terms are:

$$\left(C_{Mg,P} - C_{Mg,S}\right)\frac{ds}{dt} = D_{Mg,P}\left.\frac{\partial c}{\partial r}\right|_{x_f -} - D_{Mg,M}\left.\frac{\partial c}{\partial r}\right|_{x_f +} \tag{4.2}$$

and

$$\left(C_{Si,P} - C_{Si,S}\right)\frac{ds}{dt} = D_{Si,P}\left.\frac{\partial c}{\partial r}\right|_{x_f -} - D_{Si,M}\left.\frac{\partial c}{\partial r}\right|_{x_f +} \tag{4.3}$$

where $D_{Mg,M}$, $D_{Mg,P}$, $D_{Si,M}$, and $D_{Si,P}$ are the diffusivities of Mg in the matrix, Mg in the precipitate, Si in the matrix and Si in the precipitate, respectively. The composition flux may be written as:

$$\left.\frac{\partial c}{\partial r}\right|_{x_f -} = \frac{C_{Si,P} - C_{Si,S}}{\Delta r} \tag{4.4}$$

and

$$\left.\frac{\partial c}{\partial r}\right|_{x_f +} = \frac{C_{Si,S} - C_{Si,M}(x_f + \Delta r)}{\Delta r}. \tag{4.5}$$

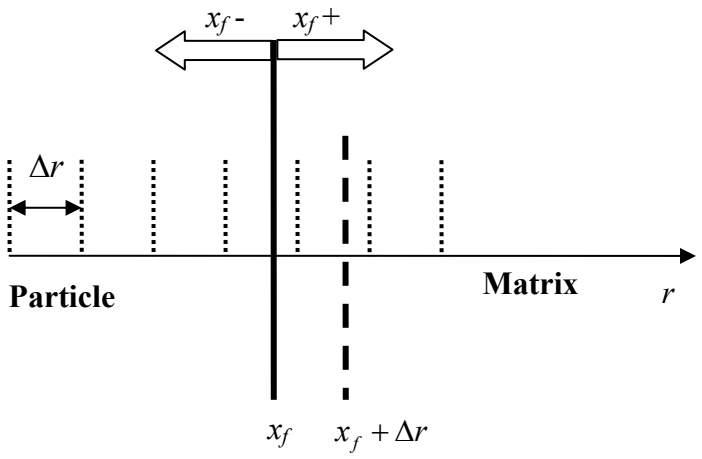

Figure 4.1 Schematic of moving interface point located at x_f on an equally spaced stationary grid. The large block arrows represent the directions for gradients at the interface.

The composition at $x_f + \Delta x$ is interpolated from neighboring grid nodes, see Figure 4.1. The boundary conditions at the interface have been specified in equations (4.1) through (4.3). The unknowns in these equations are the interface compositions, the compositions at the grid nodes at the current time step, and the interface velocity, $\frac{ds}{dt}$. The compositions at the grid nodes are found using the diffusion equation, which in the example we are considering here may be expressed as:

$$\frac{\partial C_{Mg}}{\partial t} = D_{Mg,M}\left(\frac{\partial^2 C_{Mg}}{\partial r^2} + \frac{2}{r}\frac{\partial C_{Mg}}{\partial r}\right) \quad \text{and} \quad \frac{\partial C_{Mg}}{\partial t} = D_{Mg,P}\left(\frac{\partial^2 C_{Mg}}{\partial x^2} + \frac{2}{r}\frac{\partial C_{Mg}}{\partial r}\right) \tag{4.6}$$

for magnesium in the matrix and the precipitate phases, respectively, and similarly for silicon:

$$\frac{\partial C_{Si}}{\partial t} = D_{Si,M}\left(\frac{\partial^2 C_{Si}}{\partial x^2} + \frac{2}{r}\frac{\partial C_{Si}}{\partial r}\right) \quad \text{and} \quad \frac{\partial C_{Si}}{\partial t} = D_{Si,P}\left(\frac{\partial^2 C_{Si}}{\partial x^2} + \frac{2}{r}\frac{\partial C_{Si}}{\partial r}\right). \tag{4.7}$$

There are zero-flux conditions at the outer boundaries of the system, at $r = 0$ and $r = L$. The interface compositions are determined iteratively by guessing the composition of Mg, calculating the composition of Si using the solubility product constant, and iterating until the interface velocity determined by the interfacial-flux balances given in equations (4.2) and (4.3) are identical to each other.

Figure 4.2 shows composition profiles for magnesium and silicon for a spherical precipitate. The simulation is carried out at a temperature of 853 K. The interface composition histories for Mg and Si are shown in Figure 4.3. The diffusivity in aluminum at 853 K of magnesium is 1.249 μm^2/sec, which is approximately 25% higher than the diffusivity of silicon at this temperature (0.948 μm^2/sec)[21]. The two species are coupled at the interface, and, as time increases, the interface composition of silicon is increasing while the interface composition of magnesium is decreasing. The presence of magnesium speeds up the diffusion of silicon, which causes the interface composition of silicon to rise while the opposite is true – the presence of silicon slows down the diffusion of magnesium and depresses the interface composition.

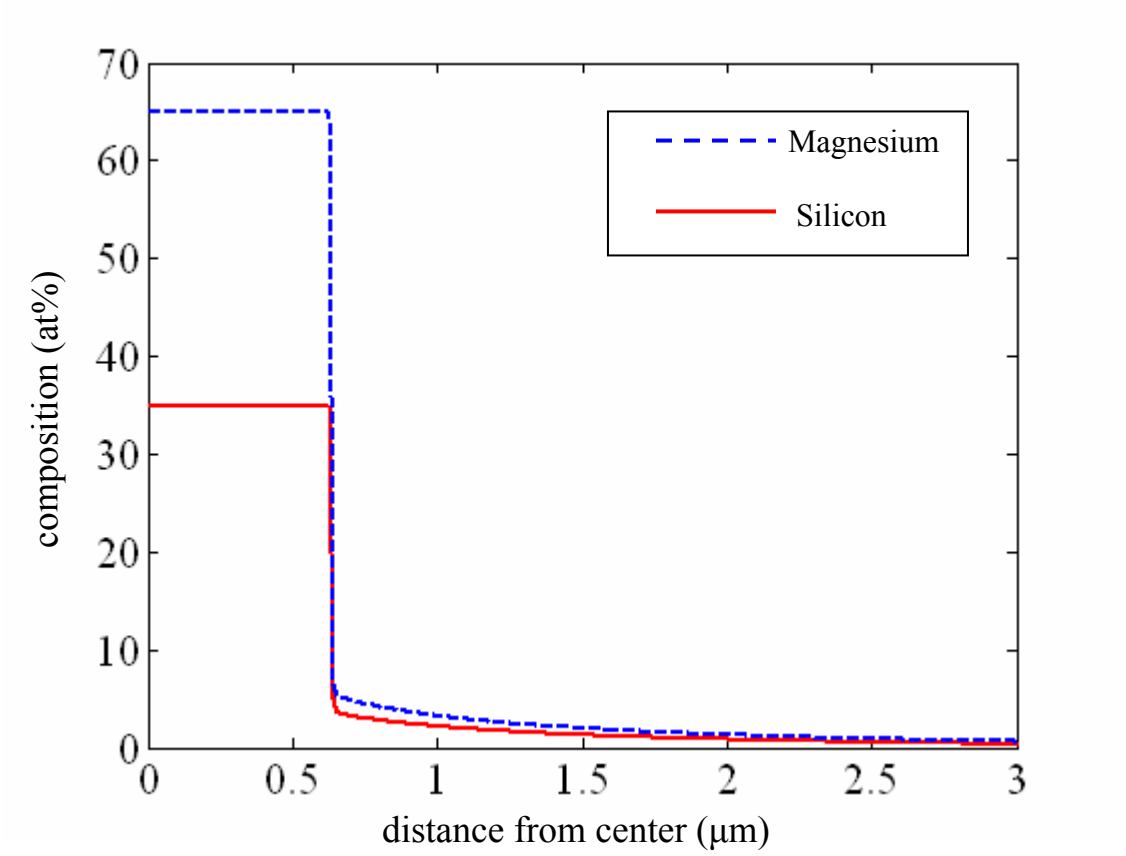

Figure 4.2 Composition profiles of magnesium (dashed line) and silicon (solid line) in atomic percent as a function of distance from the center of a spherical precipitate. The initial radius is 1 μm, dissolving in a sphere of radius 8 μm. $C_{Mg,P}$ = 65%, $C_{Si,P}$ = 35%, $D_{Si,M}$ = 1.249 μm^2/s, $D_{Mg,M}$ = 0.324 μm^2/s, K = 98 at%.

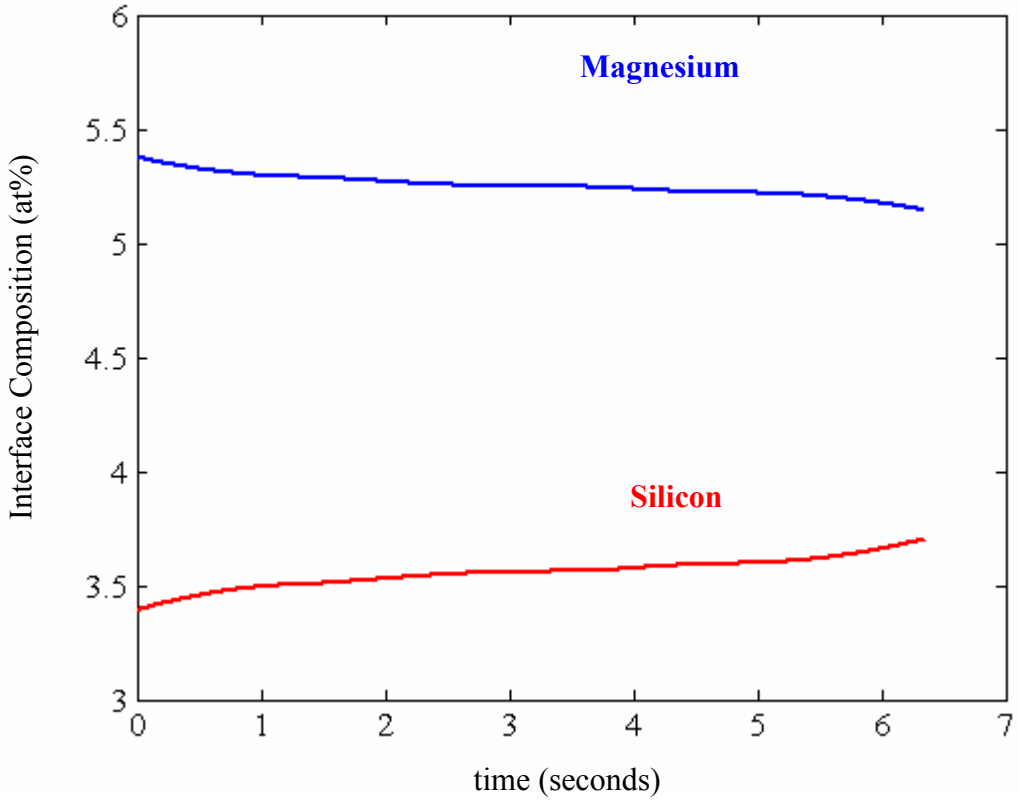

Figure 4.3 Interface composition as a function of time for magnesium (blue line) and silicon (red line). The initial radius is 1 μm, dissolving in a sphere of radius 8 μm. $C_{Mg,P}$ = 65%, $C_{Si,P}$ = 35%, $D_{Si,M}$ = 0.948 μm^2/s, $D_{Mg,M}$ = 1.249 μm^2/s, K = 98 at%.

4.2 Inter-particle Spacing

The previous discussions in Chapter 3 and Section 4.1 have all considered a uniformly spaced particle dissolving in a matrix. This is an idealization of the actual geometry of the system. In this section the effects of initial particle spatial-distribution on the dissolution of Mg_2Si in an aluminum matrix will be investigated. The initial size of the precipitate will remain constant for all three cases, as will the area fraction of precipitate in the matrix. Three cases will be considered, as shown in Figure 4.4. The shaded region is the actual computational domain. Case 1 represents uniformly spaced precipitates, centered in the solution domain. In Case 2 the precipitate is located one precipitate-diameter from the left-hand side of the vertical axis, but still centered vertically within the cell. This resembles the conditions that give rise to clustering of precipitates. Further clustering has occurred in the third case. The particle is located one precipitate-diameter from the left side of the vertical axis and one precipitate-diameter up from the bottom of the horizontal axis.

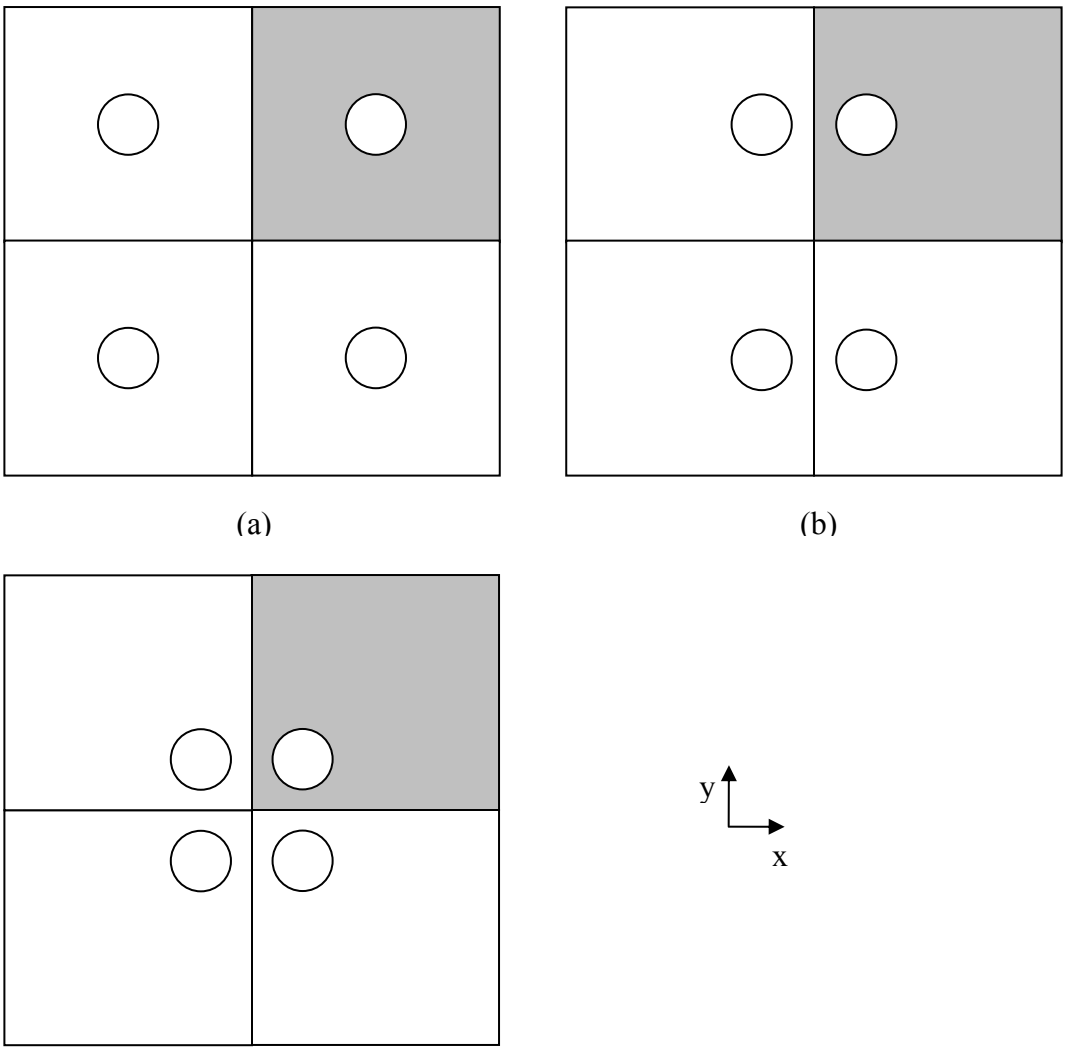

Figure 4.4 Schematic of the particle spacing used in the following simulations: (a) Case 1, particle is centered in the matrix; (b) Case 2, particle center is one diameter from the wall in the x-direction, and centered in the y-direction; and (c) Case 3, particle is located one diameter from the wall in the x- and y-directions. The shaded region shows the actual computational domain.

Figure 4.5 shows the radius as a function of time for the three different cases of inter-particle spacing. The radius is determined by taking the average radii between the initial precipitate center and interface point locations. The precipitates of Cases 2 and 3 do not dissolve symmetrically, so their average radii do not vary smoothly with time as for Case 1. As expected, the dissolution time of Case 1 is the fastest, followed by Case 2, while Case 3 is the slowest. These results show that knowledge of the inter-particle spacing is necessary for accurate prediction of dissolution time. Figure 4.6 shows the interface location profiles for all three cases at one second intervals from zero to ten seconds. The asymmetric interface motion experienced under Cases 2 and 3 is obvious in Figure 4.6. The concentration contours of magnesium and silicon dissolving for each of these cases are shown in Figures 4.7 through 4.12. The composition of magnesium inside the precipitate is 65 at% and the composition of silicon inside the precipitate is 35 at%. The initial precipitate radius is 3 μm for all three cases and the solution domain is 30 μm by 30 μm, which results in a constant area fraction of 0.0314. The simulation is carried out isothermally at 853 K. The diffusivity of magnesium in aluminum is 1.249 $\mu m^2/sec$ and the diffusivity of silicon in aluminum is 0.948 $\mu m^2/sec$.

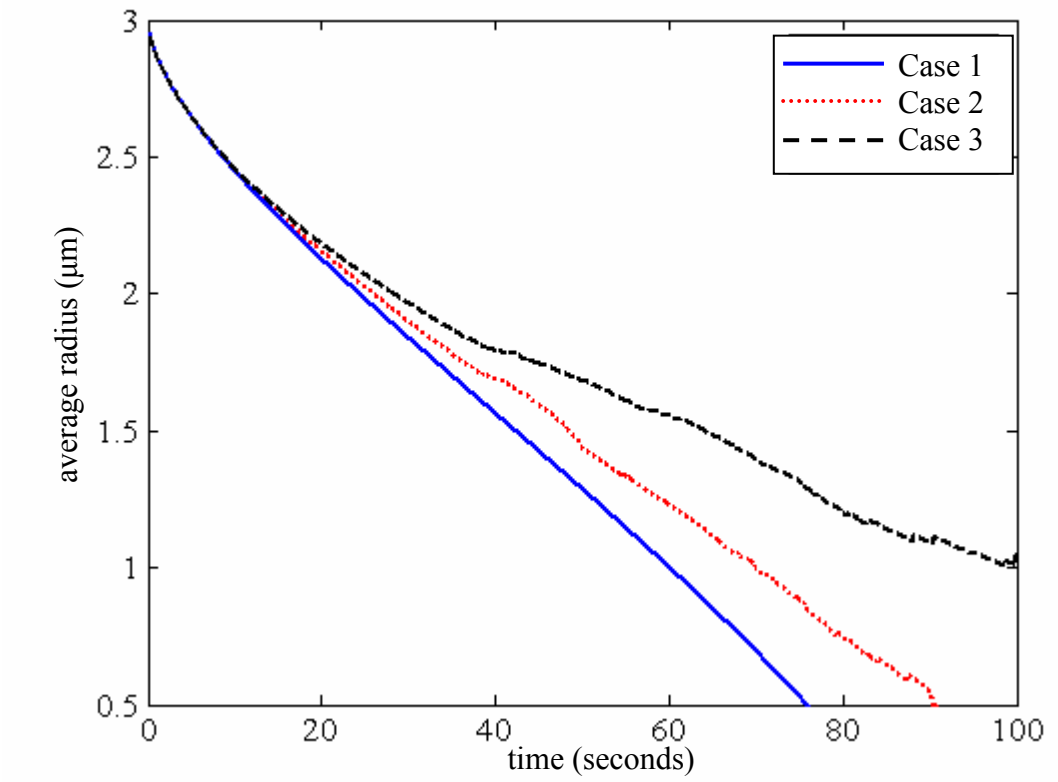

Figure 4.5 Average radius location as a function of time for the three different cases Case 1 (solid line), Case 2 (dotted line), Case 3 (dashed line). Case 1 corresponds to equal spacing of particles in a matrix, Case 2 corresponds to two mirrored particles in a matrix, and Case 3 corresponds to four particles mirrored in a matrix. Note that the average radius is calculated by taking an average of the distance between each interface point and the initial radius. Because the precipitates in Cases 2 and 3 do not dissolve symmetrically, their average radius profiles are not smooth.

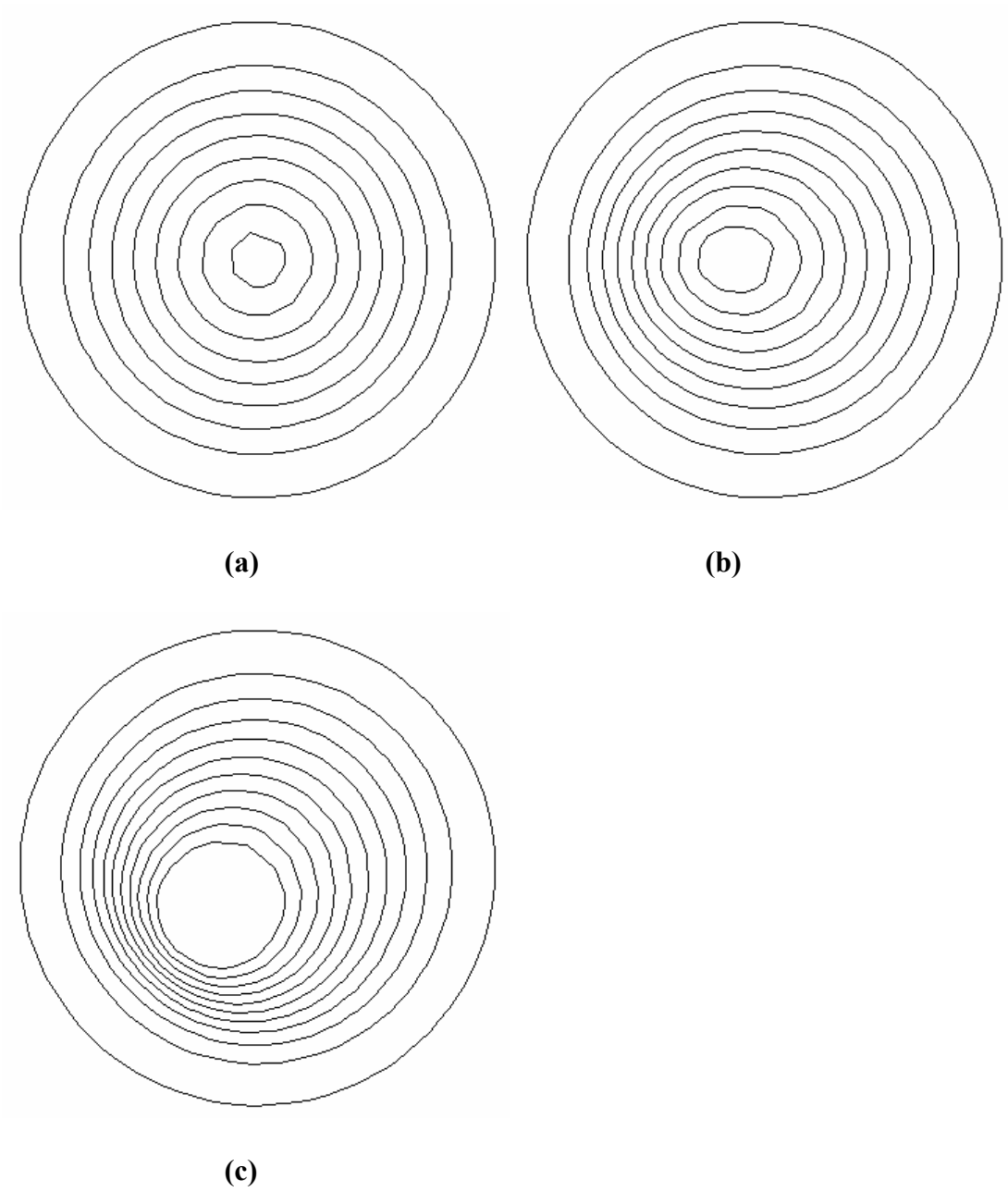

Figure 4.6 Interface location profiles at one second intervals from 0 to 10 seconds for particles dissolving under (a) Case 1, (b) Case 2, and (c) Case 3 conditions. The particle in (a) is dissolving symmetrically, while the particles in (b) and (c) are dissolving asymmetrically.

Figures 4.7 and 4.8 show the concentration contours at 20, 40, 60, and 80 seconds for magnesium and silicon, respectively, for uniformly spaced particles dissolving in an aluminum matrix. The particle is dissolving symmetrically in the matrix, which can be observed by the symmetric concentration contours surrounding the precipitate. The precipitate is indicated by the innermost contour. As time increases the solutal elements spread out across the graphs. The magnesium (Figure 4.7) has diffused away from the particle/matrix interface faster than the silicon (Figure 4.8) for all cases, because the diffusivity of magnesium in aluminum is 25% higher than the diffusivity of silicon in aluminum.

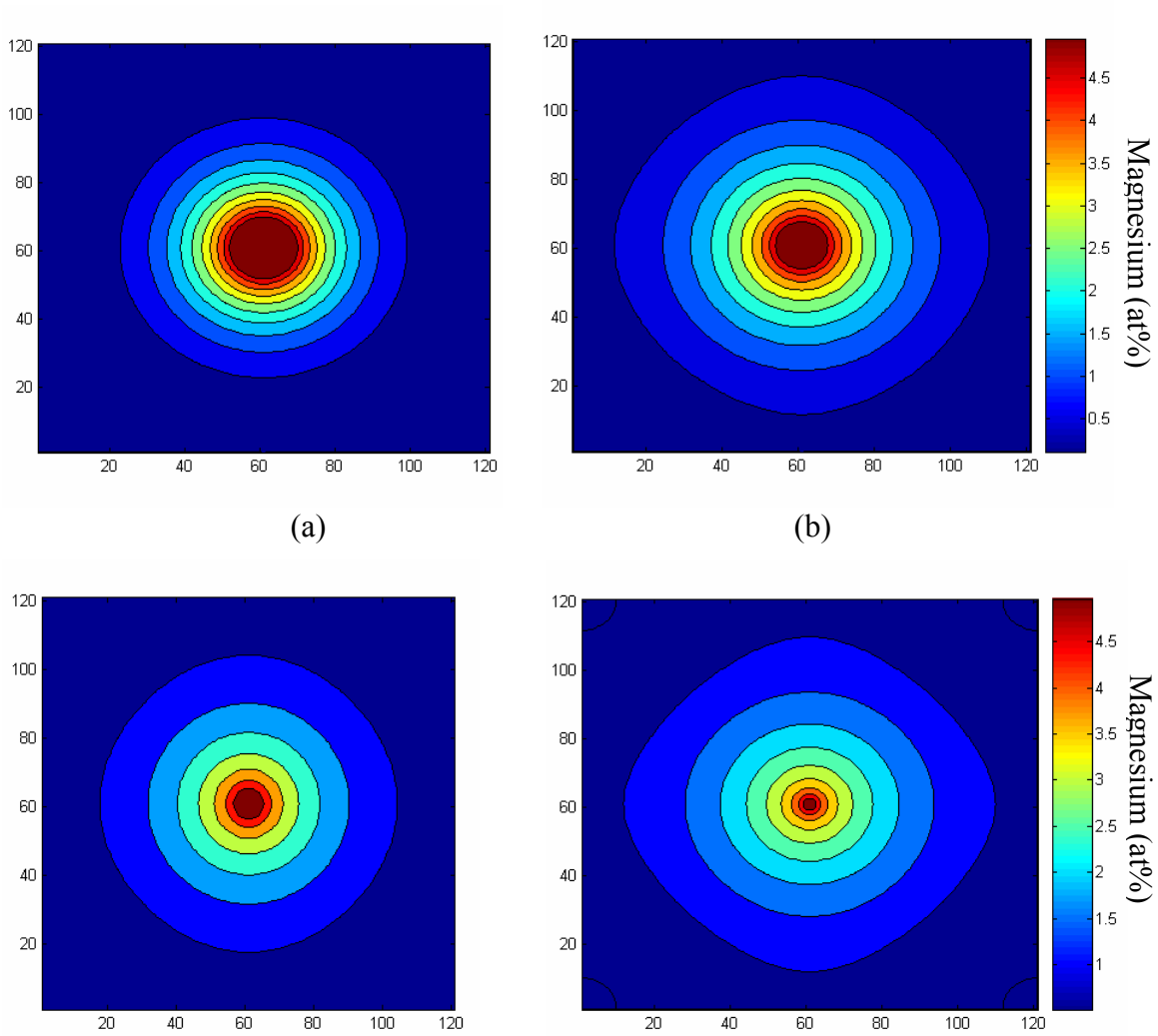

Figure 4.7 Composition contours for magnesium at (a) 20 seconds, (b) 40 seconds (c) 60 seconds and (d) 80 seconds. The precipitate is centered in the solution domain. The particle/matrix interface is depicted by the innermost concentration contour.

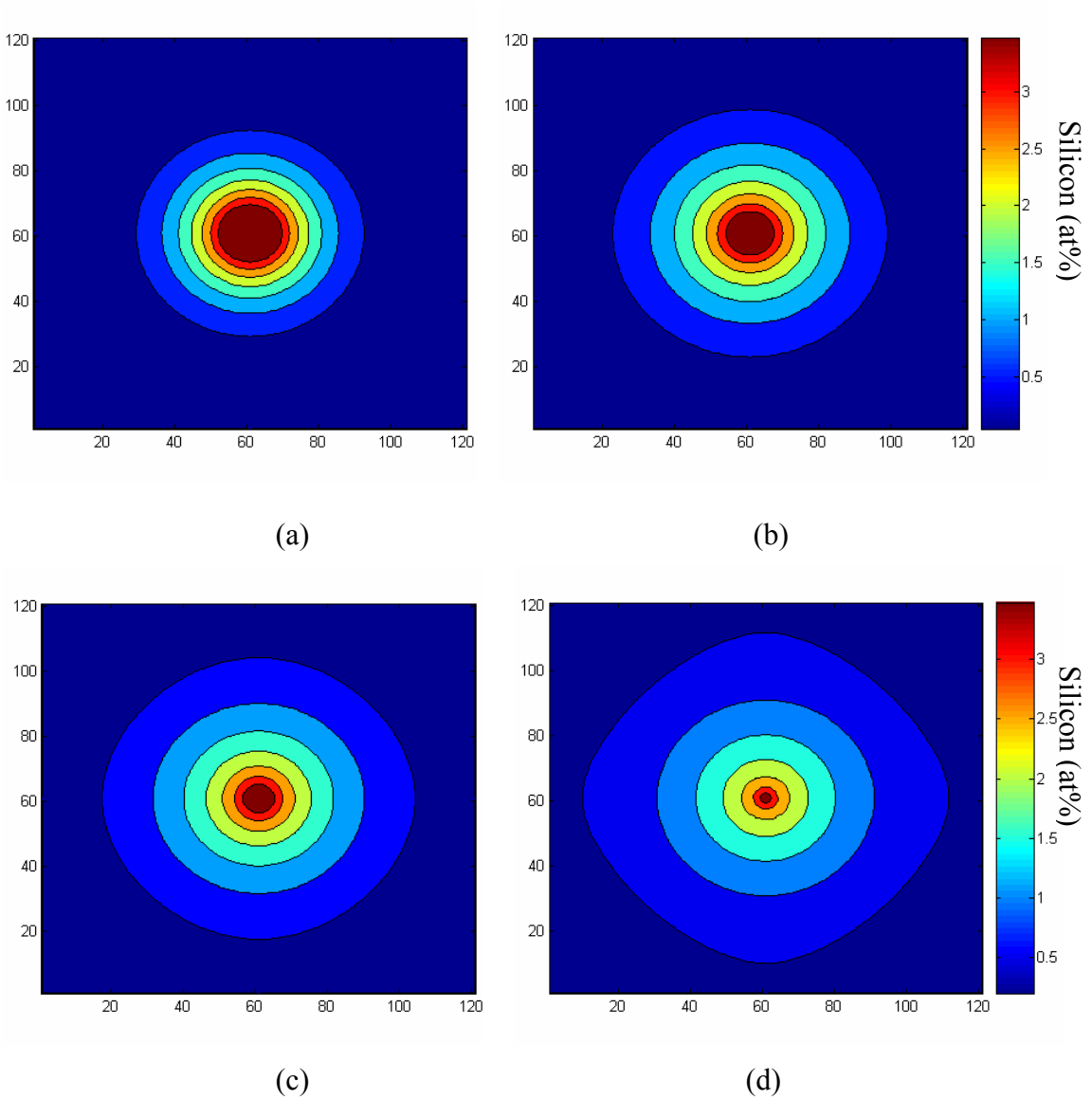

Figure 4.8 Composition contours of silicon at (a) 20 seconds, (b) 40 seconds, (c) 60 seconds and (d) 80 seconds. The precipitate is centered in the solution domain. The particle/matrix interface is depicted by the innermost concentration contour.

Figures 4.9 and 4.10 show the concentration contours at 20, 40, 60, and 80 seconds for magnesium and silicon, respectively, for the precipitate dissolving under Case 2 conditions. Again, the precipitate is shown by the innermost concentration contour. The particle is centered vertically (at 2.5 precipitate-diameters) and located one precipitate-diameter from the left-hand vertical axis. The influence of the symmetry condition at the boundaries is evident from the increase in solute concentration on the left side of the graphs. The solutal elements spread out towards the top and bottom of the computational domain into the matrix. The concentration gradients are steeper towards the larger inter-particle spacing, so the precipitate dissolves asymmetrically (recall that the interface velocity is a function of the concentration gradient at the interface). The magnesium (Figure 4.9) has diffused away from the particle/matrix interface faster than the silicon (Figure 4.10) for all cases, because the diffusivity of magnesium in aluminum is 25% higher than the diffusivity of silicon in aluminum.

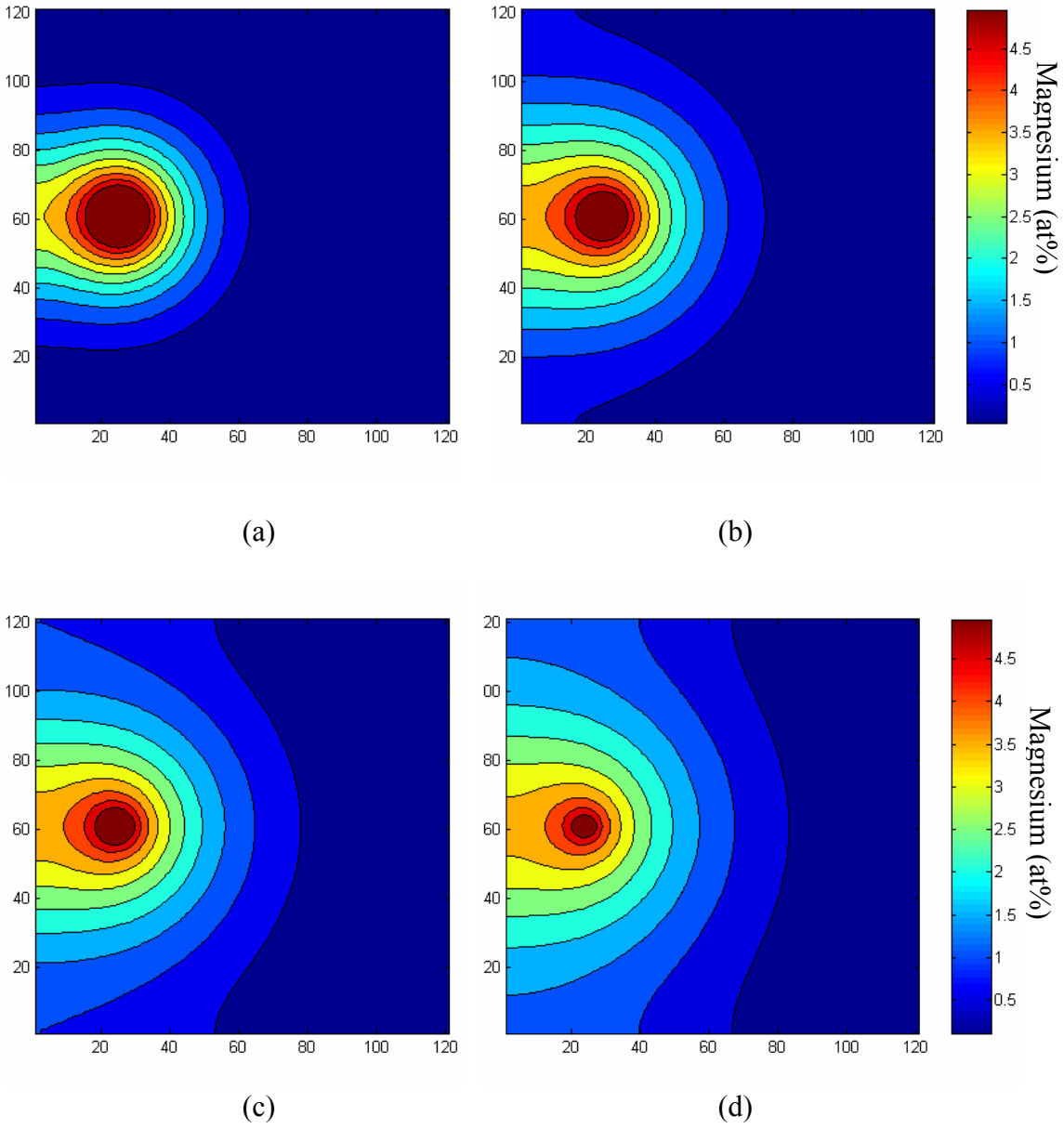

Figure 4.9 Magnesium concentration contours at (a) 20 seconds, (b) 40 seconds, (c) 60 seconds, and (d) 80 seconds. The influence of the symmetry conditions at the boundaries is evident as solute builds up on the left-hand side of the solution domain. The precipitate/matrix interface is depicted by the innermost concentration contour.

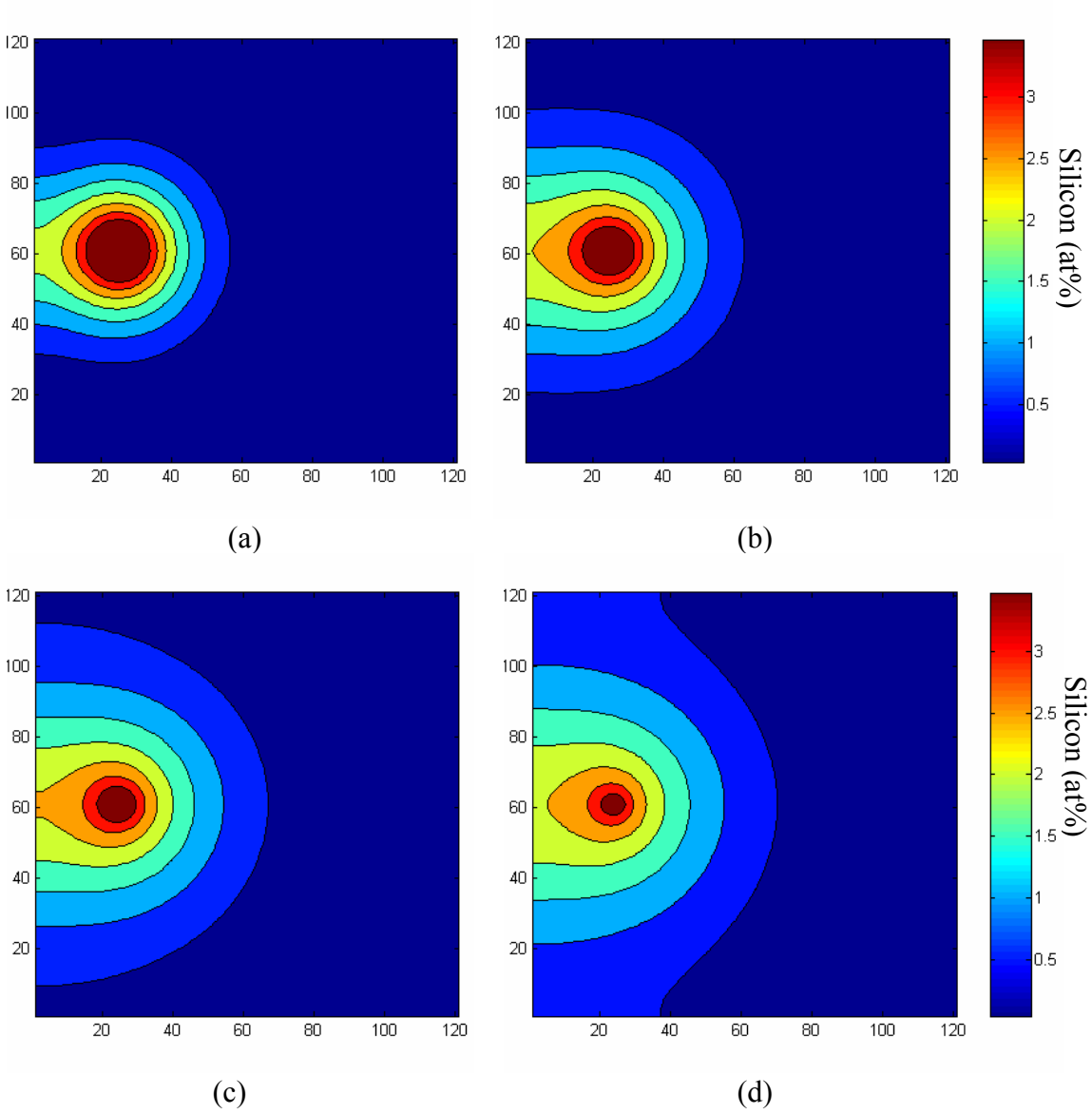

Figure 4.10 Silicon concentration contours at (a) 20 seconds, (b) 40 seconds, (c) 60 seconds, and (d) 80 seconds. As time increases, the silicon spreads out into the matrix. The influence of the symmetry conditions at the boundaries is evident as solute builds up on the left-hand side of the solution domain. The particle/matrix interface is depicted by the innermost concentration contour.

Figures 4.11 and 4.12 show the concentration contours at 20, 40, 60, and 80 seconds for magnesium and silicon, respectively, for a precipitate dissolving under Case 3 conditions. The precipitate is located one precipitate-diameter from the left vertical axis and one precipitate-diameter from the lower horizontal axis. The influence of the symmetry conditions is evident from the increase in solute concentration in the lower left corner of the graphs. The solutal elements spread out diagonally across the computational domain into the matrix. Again, recall that the interface velocity is a function of the concentration gradients at the interface. The concentration gradients facing the lower left corner of the solution domain are smaller than those facing the upper right corner, so the particle dissolves asymmetrically. The magnesium (Figure 4.11) has diffused away from the particle/matrix interface faster than the silicon (Figure 4.12) for all cases, because the diffusivity of magnesium in aluminum is 25% higher than the diffusivity of silicon in aluminum.

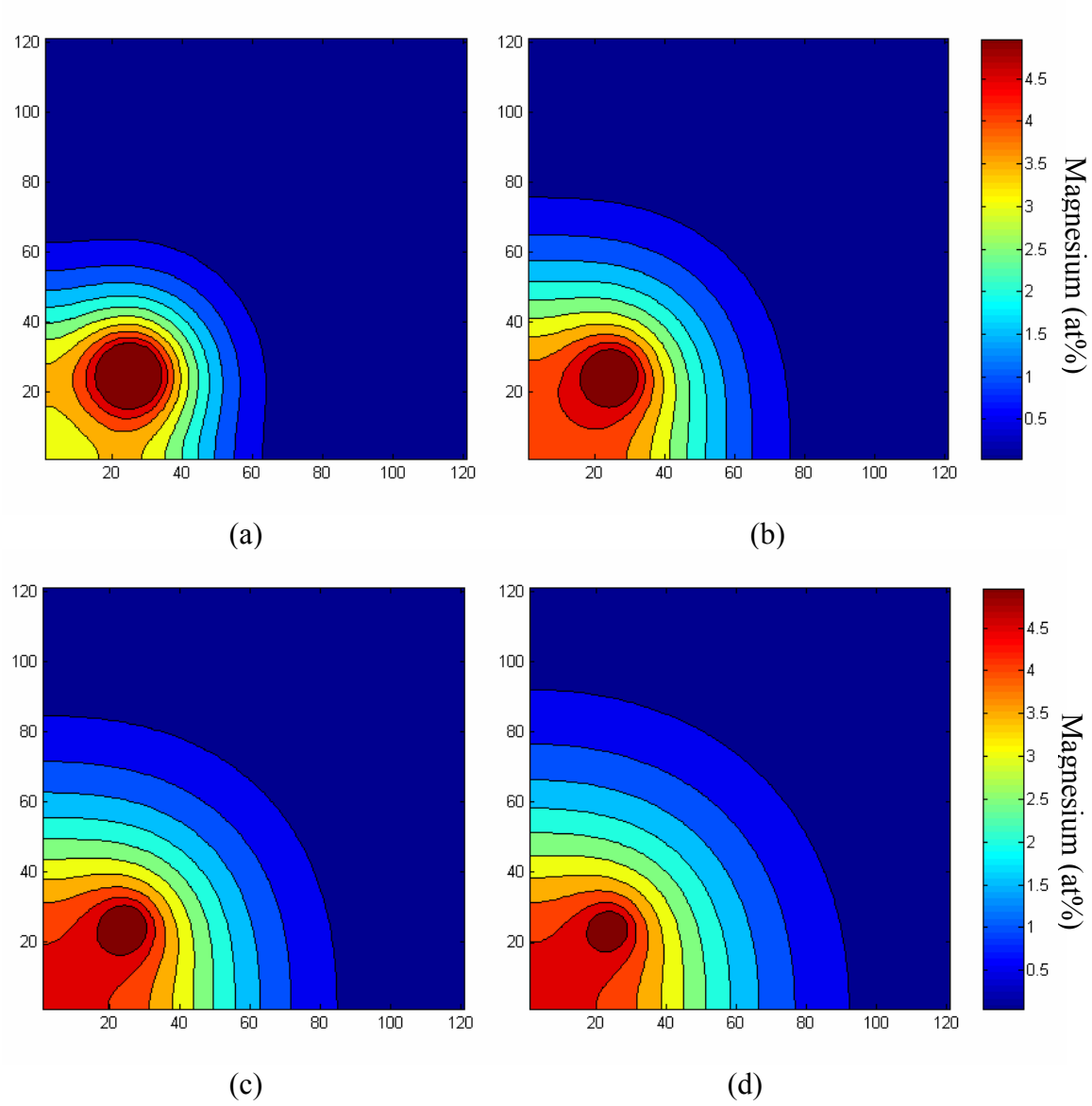

Figure 4.11 Magnesium concentration contours for Case 3 at (a) 20 seconds, (b) 40 seconds, (c) 60 seconds, and (d) 80 seconds. The influence of the symmetry conditions at the boundaries is evident as solute builds up in the lower left corner of the solution domain. The particle/matrix interface is depicted by the innermost concentration contour.

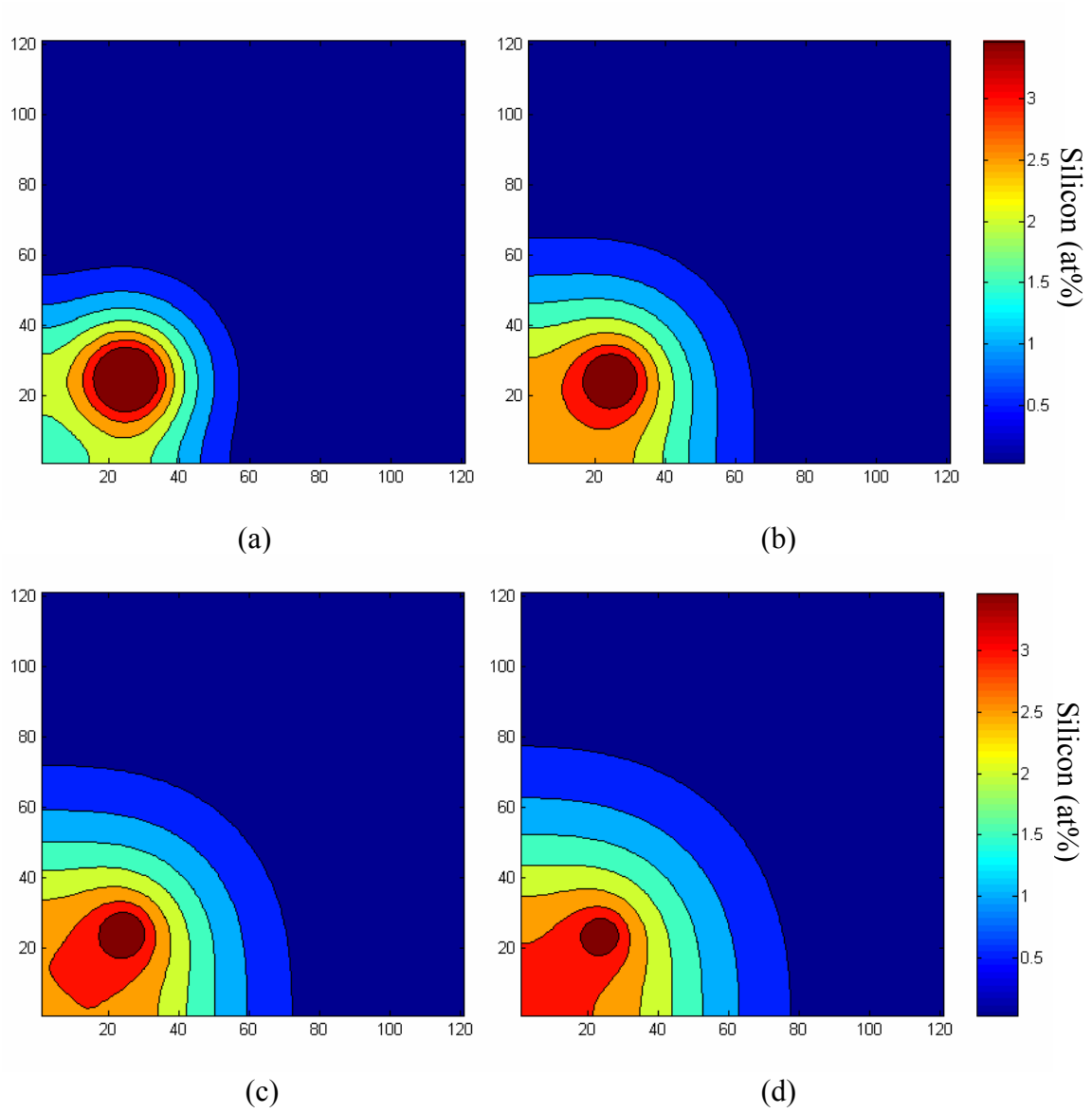

Figure 4.12 Silicon concentration contours for Case 3 at (a) 20 seconds, (b) 40 seconds, (c) 60 seconds, and (d) 80 seconds. The influence of the symmetry conditions at the boundaries is evident as solute builds up in the lower left corner of the solution domain. The particle/matrix interface is depicted by the innermost concentration contour.

4.3 Multiple Particle Interactions

Aluminum alloys typically contain a range of precipitate sizes that are not symmetrically located in the matrix. In this section, a distribution of three particles with three different sizes is considered. Three Mg_2Si particles of radius $3.0\,\mu m$, $2.5\,\mu m$, and $1.5\,\mu m$ were placed randomly in a matrix $30\,\mu m \times 30\,\mu m$ in size. The composition profiles are shown in Figures 4.13 and 4.14 for magnesium and silicon, respectively. The smallest particle is on the left side of the graphs and the largest particle is located in the upper right corner. The composition contours in Figures 4.13 and 4.14 are shown at 0, 10, 50 and 100 seconds. The precipitates are indicated by the darkest red color in the graphs, and the compositions of magnesium and silicon within the precipitates are 65 at% and 35 at%, respectively. At 10 seconds all three precipitates remain in the matrix. Solute builds up between each precipitate and the nearest solution-domain boundary due to the no-flux condition imposed there. The solute from the two precipitates on the right side of the graphs has begun to overlap. At 50 seconds the smallest particle (located on the left side) has disappeared, and the solute from that particle has spread out on the left side of the solution domain. The two remaining particles are no longer circular in shape. The largest particle remains at 100 seconds, and the influence of the medium-size particle is still clear in the composition contours. The solute from the smallest particle has diffused throughout the region on the left of the graphs.

It is clear from these figures that the presence of other precipitates in the matrix influences the dissolution of an individual precipitate. The precipitates dissolve in an asymmetric manner when their solutal profiles overlap. The dissolution of precipitates

close to each other is slower because solute builds up between them, stalling diffusion of solute into the matrix. As expected, the smaller particles dissolve faster than larger particles; however their presence at the initial time has influenced the dissolution of the largest particle.

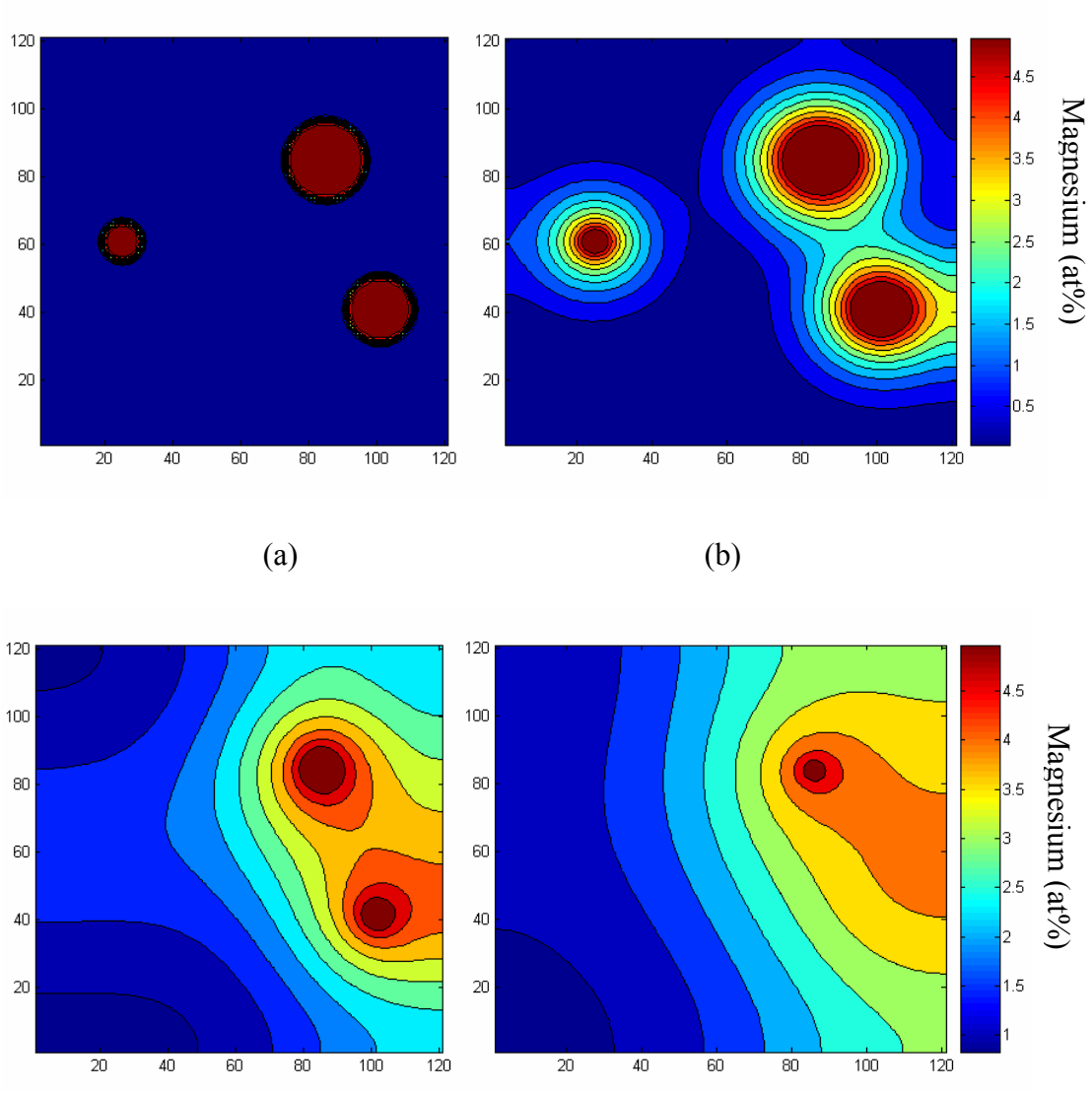

Figure 4.13 Magnesium concentration contours at (a) 0 seconds, (b) 10 seconds, (c) 50 seconds and (d) 100 seconds. At 10 seconds the concentration profiles from the two particles on the right hand side have begun to overlap. At 50 seconds the smallest particle has completely dissolved. At 100 seconds, the medium-sized particle has dissolved but the influence on the concentration contours is still observed.

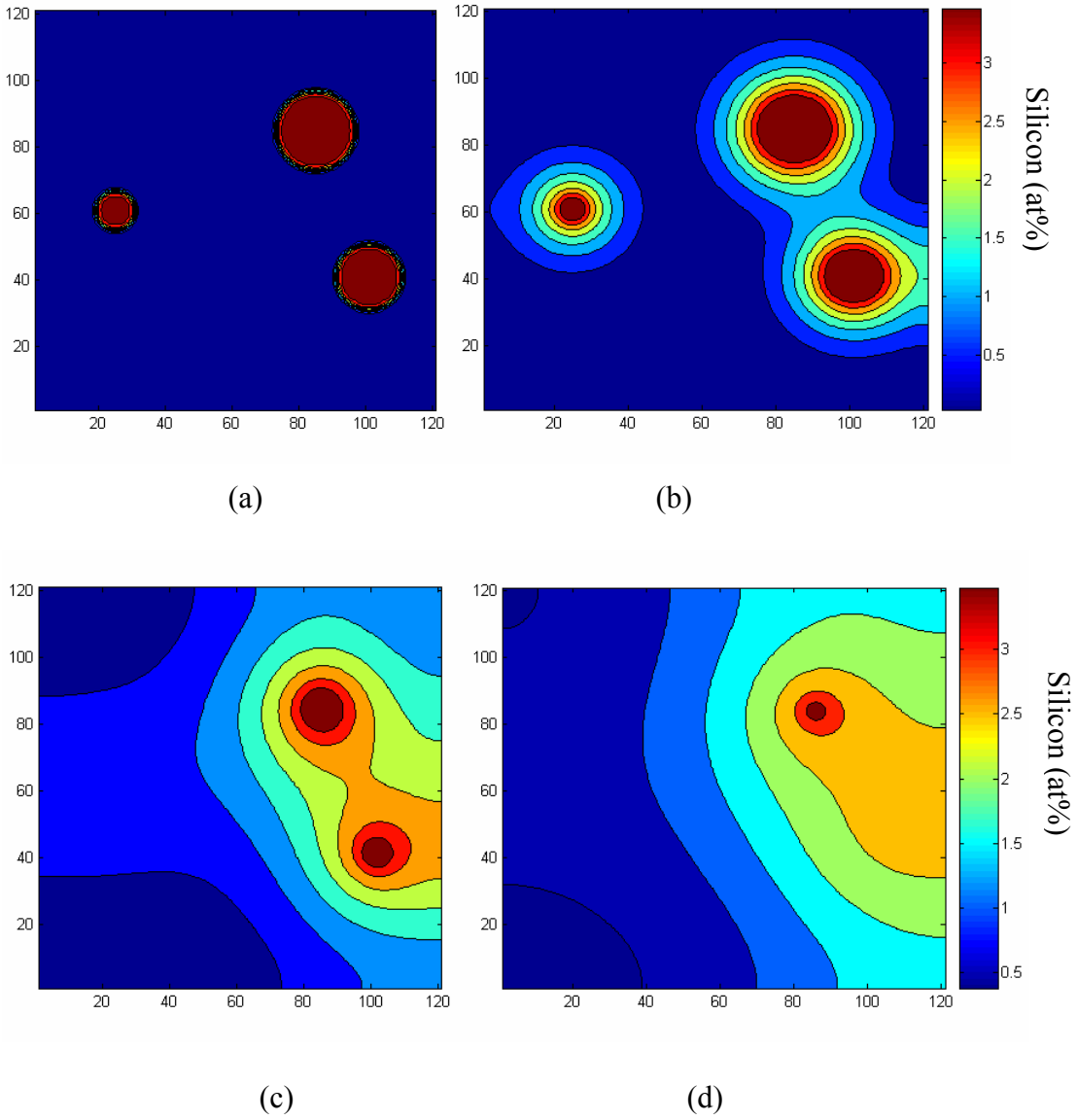

Figure 4.14 Silicon concentration contours at (a) 0 seconds, (b) 10 seconds, (c) 50 seconds, and (d) 100 seconds. At 10 seconds the concentration profiles from the two particles on the right hand side have begun to overlap. At 50 seconds the smallest particle has completely dissolved. At 100 seconds, the medium-sized particle has dissolved but the influence on the concentration contours is still observed.

CHAPTER FIVE

CONCLUSIONS AND RECOMMENDATIONS

5.1 Conclusions

A general particle-dissolution model has been developed for multi-component alloys using front-tracking. The model may be used in one and two dimensions, with a variety of precipitate sizes and shapes. The immersed-boundary front-tracking method of Trygvasson [56] , Juric [45, 51], and Shin [44, 52, 53] has been combined with the ghost-fluid method of Gibou *et al*. [57], removing the need for solutal mass source terms at the particle/matrix interface. The front-tracking methods were both compared with an exact solution for a planar particle dissolving in an infinite matrix. Both methods performed well with respect to interface location; however, the immersed-boundary method deviated more from the exact solution than the sharp-interface method (*cf*. Figure 3.5). The sharp-interface method was also shown to conserve mass better than the immersed-boundary method (*cf*. Figure 3.6). Furthermore, when composition profiles obtained using the two front-tracking methods were compared with an exact solution, the sharp-interface method out-performed immersed-boundary method. The composition error norms for the immersed-boundary method were all higher than those for the sharp-interface method (*cf*. Figures 3.8 – 3.10). An additional advantage of the sharp-interface method is that

it is more efficient and faster than the immersed-boundary method because the source terms are no longer necessary.

The sharp-interface front-tracking model was compared with results for precipitate dissolution in binary alloys. Two sets of experimental data were found for dissolution of θ in the aluminum-copper alloy system. The two-dimensional model performed well when compared with both sets of data. Reiso *et al.*'s [60] experiments were performed with an Al-4.2Cu alloy with an initial average precipitate radius of 3 μm (*cf.* Figure 3.16). Baty *et al.* [59] considered dissolution of θ in an Al-4Cu alloy, with an average initial precipitate radius of 0.3 μm (*cf.* Figure 3.17). The model was able to capture the dissolution kinetics at both of these precipitate sizes. The spherical model performed very well when compared with Hewitt and Butler's [18] experimental data on dissolution of θ′ in an Al-3Cu alloy (*cf.* Figure 3.18). The two-dimensional model was also compared with Hewitt and Butler's [18] experimental data and predicted a much longer dissolution time. This result suggests that the shape of the dissolving precipitate must be taken into consideration to obtain a meaningful description of the dissolution kinetics. The model was also compared with Tundal and Ryum's [13] data for dissolution of spherical silicon particles in an Al-Si alloy. The average initial radius reported by Tundal and Ryum was used to run the simulations for three different temperatures, using the spherical model. In all three cases, the spherical model under-predicted the dissolution time (*cf.* Figure 3.19). Tundal and Ryum observed a distribution of precipitates dissolving in the matrix. The smaller particles dissolve first, so at longer times the experimentally determined average radius will be dominated by the largest

particles (*cf*. Figure 3.20). However, the small particles still influence the dissolution of the larger particles after they have disappeared, due to soft-impingement of solute. If one is interested in capturing the overall kinetics of dissolution, a distribution of precipitates must be included in the model.

Dissolution of Mg_2Si in an Al-Mg-Si alloy was also investigated. The compositions and fluxes of the solutal elements, Mg and Si, are coupled at the moving interface. Because the diffusion coefficient of magnesium in aluminum is 25% higher than the diffusion coefficient of silicon in aluminum at 853 K, magnesium diffuses away from the precipitate/matrix interface faster than silicon. Thus, the rate-limiting step controlling the dissolution for multi-component alloys is not the diffusion into the matrix, but the coupling of the solutal elements at the precipitate/matrix boundary.

Particle size, shape, and distribution (both spatial and size distributions) affect the dissolution time. Clustering of particles slows the dissolution time and causes asymmetrical interface motion. This phenomenon was shown for the ternary alloy in Chapter Four, (*cf*. Figures 4.5 through 4.11). The precipitate dissolution time was longer for precipitates that were closer to the no-flux boundaries. Additionally, the influence of a distribution of sizes was examined for ternary alloys. Smaller particles dissolve faster than larger particles but still affect the diffusion of solute away from the larger particles, which in turn may slow down the dissolution of the larger particles (*cf*. Figures 4.12 and 4.13). The results for clustering and size-distributions of particles are not unique to ternary alloys. Precipitates in binary and higher-order alloys will experience the same effects on dissolution time.

5.2 Contributions

This work is the first in the available literature to detail a general dissolution model for multi-component alloys in two dimensions. The main contributions of this research on the dissolution of secondary phases in aluminum alloys are listed below.

1. A general dissolution model has been developed for multi-component alloys that is applicable in one and two dimensions. In the past, other researchers have developed two-dimensional simulations for binary alloys [39] and one-dimensional solutions have been developed for multi-component alloys [21, 27, 29, 30, 32-34, 39, 42]. This research represents the first effort to model the dissolution of precipitates in a multi-component aluminum-alloy in two dimensions.
2. A sharp-interface method has been developed, combining front-tracking with the ghost-fluid method. This new method was shown to be more accurate than the immersed-boundary front-tracking method when compared with an exact solution for dissolution. The sharp-interface front-tracking method has also been validated based on experimental data found in the literature.
3. The effect of particle spacing on dissolution in two-dimensions has been investigated. To the author's knowledge, inter-precipitate spacing has not previously been quantified.
4. The effect of multiple particle interactions in two dimensions has been investigated. Previously, Vermolen *et al*. [39] showed a plot of concentration contours of two different size particles dissolving in a binary aluminum alloy and

suggested that more work be done in this area. This is the first time multiple particle interactions have been investigated in a multi-component aluminum alloy.

5.3 Recommendations for Future Work

This work is the first in the available literature to consider the effects of inter-particle spacing and multiple-particle interactions in multi-component alloys. Based on the experience gained in this research, the following recommendations for future work are suggested.

The current calculations are for isothermal holds, useful information will be gained by including a representative heat-treatment schedule from the aluminum industry. The diffusion coefficients and solubility product constant would vary throughout time because they follow an Arrhenius relationship with temperature. The interface compositions also depend on temperature, according to the specific alloys phase diagram. Phase-diagram-calculation software, such as PANDAT and Thermocalc, should be combined with the current model in order to determine interface compositions.

More complex geometries should be investigated. Precipitates form in a variety of shapes such as rods, cubes, rectangles, and ellipsoids to name a few. The dissolution of precipitates of varying shapes should be investigated, perhaps necessitating three-dimensional simulations. Furthermore, a more realistic size-distribution of particles should also be investigated. This could be accomplished by using a micrograph as the initial condition, which would incorporate both a size and shape distribution of particles dissolving in the matrix.

Currently, only one type of second-phase particle is considered. Actual alloys have several different secondary phases present in the matrix. For example, an Al-Mg-Si alloy may have Mg_2Si and Si particles embedded in the matrix. The presence of the silicon particles will undoubtedly influence the dissolution of the Mg_2Si particles, and vice versa.

Combining the dissolution model with models for particle growth will permit a more accurate description of the microstructural evolution throughout heat-treatments. Presently, the homogenization step may be modeled–using the as-cast microstructure as the starting condition for precipitate size and distribution. Dissolution during the precipitation-hardening heat-treatment step may also be modeled; however the initial condition is more ambiguous. A more complete picture of precipitate behavior would be captured if both growth and dissolution of the various second-phase particles were modeled throughout all of the heat-treatments.

Finally, more experimental data are needed to validate the model. There is a dearth of information regarding precipitate dissolution in the open literature. Experiments should be designed to capture the dissolution behavior in multi-component alloys, in particular.

APPENDIX A

FINITE-DIFFERENCE EQUATIONS

The finite-difference equations that were used to calculate composition are given in this appendix for the two-dimensional models. First, the finite-difference equations will be expressed for the immersed-boundary method. Then the finite-difference equations for the sharp-interface method will be described.

The diffusion equation was solved on a regular, fixed grid using a conservative, second-order, centered-difference scheme for the spatial variables and an explicit, first-order, forward Euler time integration method. Consider the computational model for node *l*,*m* shown in Figure A.1. The immersed boundary front-tracking method included a source term in the finite-difference equations. In this case, the finite-difference equation for component *i* at node *l*,*m* is given by:

$$C_{l,m}^{t+1} = C_{l,m}^{t} + \Delta t \cdot Q_{l,m} + \frac{D_{ij}\Delta t}{\Delta x^2}\left\{C_{l-1,m}^{t} - 2C_{l,m}^{t} + C_{l+1,m}^{t}\right\} + \frac{D_{ij}\Delta t}{\Delta y^2}\left\{C_{l,m-1}^{t} - 2C_{l,m}^{t} + C_{l,m+1}^{t}\right\} \quad \text{(A.1)}$$

where Q represents the solutal mass source term of component i at node (l, m). For simplicity, the diffusivity, D_{ij} , has been taken as constant throughout the solution domain. Note that the diffusivity at each node may be different than the nodes surrounding it, so care must be taken to ensure that the correct diffusivity is used.

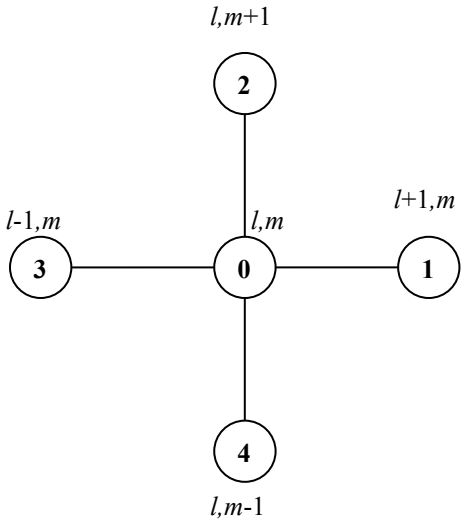

Figure A. 1 Computational model for explicit finite differencing surrounding node *l,m*.

The explicit method is subject to the stability condition that $\Delta t \le 4\frac{\min(\Delta x, \Delta y)^2}{\max(\mathbf{D})}$.

A second method was used to calculate the composition – the sharp-interface method. The source terms are no longer included in the sharp-interface method, and ghost points are used for grid points that are near the moving interface. Interpolation of "ghost" compositions is described in Chapter Two. Again, consider the schematic in Figure A.1. There are two possibilities for the positions between each node.

- If nodes 0 and 1 are on the same side of the interface, $C^t_{l+1,m} = C(l+1,m)$.
- If nodes 0 and 1 do not lie on the same side of the interface, $C^t_{l+1,m} = C_{\text{interpolated}}$.

- If nodes 0 and 3 are on the same side of the interface, $C^t_{l-1,m} = C(l-1,m)$.
- If nodes 0 and 3 do not lie on the same side of the interface, $C^t_{l-1,m} = C_{\text{interpolated}}$.
- If nodes 0 and 2 are on the same side of the interface, $C^t_{l,m+1} = C(l,m+1)$.
- If nodes 0 and 2 do not lie on the same side of the interface, $C^t_{l,m+1} = C_{\text{interpolated}}$.
- If nodes 0 and 4 are on the same side of the interface, $C^t_{l,m-1} = C(l,m-1)$.
- If nodes 0 and 4 do not lie on the same side of the interface, $C^t_{l,m-1} = C_{\text{interpolated}}$.

The finite-difference equation for the sharp-interface method is then given by:

$$C^{t+1}_{l,m} = C^t_{l,m} + \frac{D_{ij}\Delta t}{\Delta x^2}\left\{C^t_{l-1,m} - 2C^t_{l,m} + C^t_{l+1,m}\right\} + \frac{D_{ij}\Delta t}{\Delta y^2}\left\{C^t_{l,m-1} - 2C^t_{l,m} + C^t_{l,m+1}\right\}. \quad \text{(A.2)}$$

Note that the only difference between Equations (A.1) and (A.2) is the absence of the mass-source term in Equation (A.2).

REFERENCES

1. Hatch, J., *Aluminum Properties and Physical Metallurgy*. 1984, Metals Park, OH: American Society for Metals.

2. Porter, D.A. and K.E. Easterling, *Phase Transformations in Metals and Alloys*. Second ed. 1992, London: Chapman & Hall.

3. Mondolfo, L.F., *Metallography of Aluminum Alloys*. 1943, New York: Wiley.

4. Thanaboonsombut, B., *Microstructural Evolution and Recrystallization Modeling in AA6013 and Compositional Variants of 6013*, in *Materials Science and Engineering*. 1993, Georgia Institute of Technology: Atlanta.

5. Guiner, A., Nature, 1938. **142**: p. 569.

6. Preston, G.D., Nature, 1938. **142**: p. 572.

7. Smith, W.F., *Structure and Properties of Engineering Alloys*. 1993, New York: McGraw-Hill.

8. Reed-Hill, R.W. and R. Abbaschian, *Physical Metallurgy Principles*. Third ed. 1992, Boston: PWS Publishing Company.

9. Schaffer, J.P., A. Saxena, S.D. Antolovich, T.H. Sanders, and S.B. Warner, *The Science and Design of Engineering Materials*. Second ed. 1999, Boston: McGraw-Hill.

10. Bauccio, M., ed. *ASM Metals Reference Book*. 1993, ASM International: Metals Park.

11. Massalski, T.B., ed. *Binary Alloy Phase Diagrams*. 1986, ASM International: Metals Park.

12. Mondolfo, L.F., *Aluminum Alloys: Structure and Properties*. 1976, London: Butterworths.

13. Tundal, U.H. and N. Ryum, *Dissolution of Particles in Binary Alloys: Part II. Experimental Investigation on an Al-Si Alloy.* Metallurgical Transactions A, 1992. **23A**: p. 445-449.

14. Chen, H. and J.E. Morral, *Variation of the Effective Diffusivity in Two-Phase Regions.* Acta Materiala, 1999. **47**(4): p. 1175-1180.

15. Chen, Q., N. Ma, K. Wu, and Y. Wang, *Quantitative phase field modeling of diffusion-controlled precipitate dissolution in Ti-Al-V.* Scripta Materialla, 2004. **50**: p. 471-476.

16. Chen, S., M.S. Vossenberg, F.J. Vermolen, and J.v.d. Langkruis, *Dissolution of beta particles in an Al-Mg-Si alloy during DSC runs.* Materials Science & Engineering A, 1999. **A272**: p. 205-256.

17. Chen, S.P., N.C.W. Kuijpers, and S.v.d. Zwaag, *Effect of microsegregation and dislocations on the nucleation kinetics of precipitation in aluminum alloy AA3003.* Materials Science & Engineering A, 2003. **A341**: p. 296-306.

18. Hewitt, P. and E.P. Butler, *Mechanisms and Kinetics of theta prime dissolution in Al-3%Cu.* Acta Metall., 1986. **34**(7): p. 1163-1172.

19. Javierre-Perez, E., *Literature Study: Numerical Methods for Solving Stefan Problems*, in *Reports of the Department of Applied Mathematical Anlaysis*. 2003, Department of Applied Math: Delft. p. 1-85.

20. Krielaart, G., R.A. Hubert, and Y. Houbaert. *Some Applications of Moving Boundary Problems in Solid State Steel Metallurgy*. in *Moving Boundaries IV*. 1997. Boston.

21. Langkruis, J.v.d., N.C.W. Kuijpers, W.H. Kool, F.J. Vermolen, and S.v.d. Zwaag. *Modeling Mg2Si Dissolution in an AA6063 Alloy During Preheating to Extrusion Temperature*. in *Seventh International Aluminum Extrusion Technology Seminar*. 2000. Chicago, IL: Aluminum Extruters Council and the Aluminum Association.

22. Matan, N., H.M.A. Winand, P. Carter, M. Karunartne, P.D. Bogdanoff, and R.C. Reed, *A Coupled Thermodynamic/Kinetic Model for Diffusional Processes in Superalloys.* Acta Materiala, 1998. **46**(13): p. 4587-4600.

23. Romig, A.D., N.Y. Pehlivanturk, and O.T. Inal. *Modeling of Diffusion Processes: Numerical Solutions to the Diffusion Equation*. in *Diffusion Analysis & Applications*. 1988. Chicago, IL.

24. Segal, G., K. Vuik, and F.J. Vermolen, *A Conserving Discretization for the Free Boundary in a Two-Dimensional Stefan Problem.* Journal of Computational Physics, 1998. **141**: p. 1-12.

25. Sinder, M. and J. Pelleg, *On Homogenization of a Binary Alloy after Dissolution of Planar and Spherical Precipitates.* Metallurgical and Materials Transactions A, 2000. **31A**: p. 1525-1530.

26. Tanzilli, R.A. and R.W. Heckel, *Numerical Solutions to the Finite, Diffusion-Controlled Two-Phase, Moving-Interface Problem(with Planar, Cylindrical, and Spherical Interfaces).* Transactions of the Metallurgical Society of AIME, 1968. **242**: p. 2313-2321.

27. Vermolen, F., K. Vuik, and S.v.d. Zwaag. *A numerical analysis for the dissolution of second phase particles in ternary alloys*. in *Moving Boundaries IV: Computational Modelling of Free and Moving Boundary Problems*. 1997.

28. Vermolen, F.J., P.v. Mourik, and S.v.d. Zwaag, *Analytical approach to particle dissolution in a finite medium.* Materials Science and Technology, 1997. **13**: p. 308-312.

29. Vermolen, F.J. and C. Vuik, *A mathematical model for the dissolution of particles in multi-component alloys.* Journal of Computational and Applied Mathematics, 2000. **126**: p. 233-254.

30. Vermolen, F.J., C. Vuik, and S.v.d. Zwaag, *Some Mathematical Aspects of Particle Dissolution and Cross-Diffusion in Multi-Component Alloys*, in *Reports of the Department of Applied Mathematics*. 2001, TU-Delft: Delft.

31. Vermolen, F.J., C. Vuik, and S.v.d. Zwaag, *Particle dissolution and cross-diffusion in multi-component alloys.* Materials Science & Engineering A, 2003. **A347**: p. 265-279.

32. Vermolen, F.J., C. Vuik, and S.v.d. Zwaag, *A mathematical model for the dissolution of stoichiometric particles in multi-component alloys.* Materials Science & Engineering A, 2002. **A328**: p. 14-25.

33. Vermolen, F.J. and K. Vuik, *A Vector Valued Stefan Problem from Aluminum Industry*, in *Modelling, Analysis and Simulation*. 1998, Stichting Mathematisch Centrum: Amsterdam.

34. Vermolen, F.J. and K. Vuik, *A numerical method to compute the dissolution of second phases in ternary alloys.* Journal of Computational and Applied Mathematics, 1998. **93**: p. 123-143.

35. Vermolen, F.J. and S.v.d. Zwaag, *A numerical model for the dissolution of spherical particles in binary alloys under mixed mode control.* Materials Science & Engineering A, 1996. **A220**: p. 140-146.

36. Whelan, M.J., *On the Kinetics of Precipitate Dissolution.* Metal Science Journal, 1969. **3**: p. 95-97.

37. Aaron, H.B. and G.R. Kotler, *Second Phase Dissolution.* Metallurgical Transactions, 1971. **2**: p. 393-408.

38. Nolfi, F.V., P.G. Shewmon, and J.S. Foster, *The Dissolution and Growth Kinetics of Spherical Precipitates.* Transactions of the Metallurgical Society of AIME, 1969. **245**: p. 1427-1433.

39. Vermolen, F., C. Vuik, and S. van der Zwaag, *Mathematical Models for Particle Dissolution in Metallic Alloys*, in *Reports of the Department of Applied Mathematics*. 2002, TU-Delft.

40. Murray, D. and F. Landis, Trans. ASME, Ser. D., 1959. **81**: p. 106-112.

41. Tundal, U.H. and N. Ryum, *Dissolution of Particles in Binary Alloys: Part I. Computer Simulations.* Metallurgical Transactions A, 1992. **23A**: p. 433-444.

42. Vitek, J.M., S.A. Vitek, and S.A. David, *Modelling of Diffusion Controlled Phase Transformation in Ternary Systems and Application to the ferrite-austenite Transformation in the Fe-Cr-Ni-system.* Metallurgical Transactions A, 1995. **26A**: p. 2007-2025.

43. Reiso, O., N. Ryum, and J. Strid, *Melting and Dissolution of Secondary Phase Particles in Al-MgSi-Alloys.* Metallurgical Transactions A, 1993. **24A**: p. 2629-2641.

44. Shin, S., *A Level Contour Reconstruction Method for three-dimensional Multiphase Flows and its Application*, in *Mechanical Engineering*. 2001, Georgia Institute of Technology: Atlanta.

45. Juric, D., *Computations of Phase Change*, in *Mechanical Engineering*. 1996, University of Michigan.

46. Crank, J., *Free and Moving Boundary Problems*. 1984, Oxford: Clarendon Press.

47. Osher, S. and J.A. Sethian, *Fronts propogating with curvature-dependent speed: Algorithms based on Hamilton-Jacobi formulations.* Journal of Computational Physics, 1988. **79**: p. 12.

48. Sethian, J.A., *Level Set Methods and Fast Marching Methods*. 1999, New York: Cambridge University Press.

49. Fabbri, M. and V.R. Voller, *The Phase-Field Method in the Sharp-Interface Limit: a comparison between model potentials.* Journal of Computational Physics, 1997. **130**: p. 256-265.

50. Suzuki, T., M. Ode, S.G. Kim, and W.T. Kim, *Phase Field Model of Dendritic Growth.* Journal of Crystal Growth, 2002. **237**: p. 125-131.

51. Juric, D. and G. Tryggvason, *A Front Tracking Method for Dendritic Solidification.* Journal of Computational Physics, 1996. **123**: p. 127-148.

52. Shin, S., S.I. Abdel-Khalik, V. Daru, and D. Juric, *Accurate representation of surface tension using the level contour reconstruction method.* Journal of Computational Physics, 2004. **article in press**.

53. Shin, S. and D. Juric, *Modeling Three-Dimensional Multiphase Flow Using a Level Contour Reconstruction Method for Front Tracking without Connectivity.* Journal of Computational Physics, 2000. **180**: p. 427-470.

54. Peskin, C.S., *Numerical Analysis of Blood Flow in the Heart.* Journal of Computational Physics, 1977. **25**: p. 220.

55. Peskin, C.S. and B.F. Printz, *Improved Volume Conservation in the Computation of Flows with Immersed Boundaries.* Journal of Computational Physics, 1993. **105**: p. 33-46.

56. Tryggvason, G. and H. Aref, *Numerical Experiments on Hele Shaw Flow with a Sharp Interface.* Journal of Fluid Mechanics, 1983. **136**: p. 1-30.

57. Gibou, F., R. Fedkiw, L.T. Cheng, and M. Kang, *A Second Order Accurate Symmetric Discretization of the Poisson Equation on Irregular Domains.* Journal of Computational Physics, 2002. **176**(1): p. 205-227.

58. Carslaw, H.S. and J.C. Jaeger, *Conduction of Heat in Solids, 2nd ed.* 1959, New York: Oxford University Press.

59. Baty, D.L., R.A. Tanzilli, and R.W. Heckel, *Solution Kinetics of CuAl2 in an Al-4Cu Alloy.* Metallurgical Transactions, 1970. **1**: p. 1651-1656.

60. Reiso, O., H.G. Overlie, and N. Ryum, *Dissolution and Melting of Secondary Al2Cu Phase Particles in an AlCu Alloy.* Metallurgical Transactions A, 1990. **21A**: p. 1689-1694.